1-1-2013

Molecular Crystallization Directed By Nanoparticles And Nanopatterns

Li Li
Wayne State University,

MOLECULAR CRYSTALLIZATION DIRECTED BY NANOPARTICLES AND NANOPATTERNS

by

LI LI

DISSERTATION

Submitted to the Graduate School

of Wayne State University,

Detroit, Michigan

in partial fulfillment of the requirements

for the degree of

DOCTOR OF PHILOSOPHY

2013

MAJOR: MATERIALS SCIENCE AND ENGINEERING

Approved by:

_____

Advisor Date

_____

_____

_____

_____

DEDICATION

This dissertation is dedicated to my parents and friends for their deepest love, encouragement and support throughout the process.

ACKNOWLEDGEMENTS

I would like to express my deepest appreciation to my advisor, Prof. Guangzhao Mao, for her guidance, supervision and support in many aspects during my Ph.D. study. She introduced me the unique and fascinating research area of confined crystallization and provided financial support for my research.

I would like to thank my committee members, Prof. Charles W. Manke, Prof. Stephanie L.Brock and Prof. Ming-Cheng Cheng for valuable suggestion for my research and dissertation.

I would like to thank my research group members, Mr. Yi Zou, Mr. Sunxi Wang, Mr. Pedram Jahanian, for their help and advice during my research. I would also like to thank Dr. Zhi Mei for helping me with the SEM and TEM training and imaging and Prof. Zhixian Zhou for the conductivity measurements.

I would like to express my eternal appreciation towards my family and friends for all unconditional supports and patience.

TABLE OF CONTENTS

LIST OF TABLES

LIST OF FIGURES

CHAPTER 1

INTRODUCTION

In nanoscience and nanotechnology, organic-inorganic hybrid materials have drawn significant interest due to their unique physical and chemical properties and applications in optical and bio-sensing materials as well as electronic applications, such as electronic devices, sensors, and electrocatalysis. One valuable advantage of organic-inorganic hybrids in nano scale is their high surface-to-volume ratio which results in higher chemical reactivity and prominent quantum effects. Another important aspect of nano hybrids is that the properties such as thermal, magnetic, optical, catalytic, and electrochemical properties depend on their size, shape and composition. Much work has been done to generate organic-inorganic hybrid materials with various structures including but not limited to core-shell, particle-rod, wire, film, *etc*. However, incorporating organic and inorganic components with controllable properties and well-defined geometry still remains a challenge.

This dissertation focuses on the molecular crystallization directed by nanoparticles and nanopatterns. The main goal of this work is to establish a universal strategy to form organic-inorganic hybrid material with unique and well-defined particle-rod nanostructures. The strategy is to use inorganic nanoparticles as seeds to initiate and confine the nucleation of organic nanorods based on seed-mediated nucleation (*SMN*). One successful method is the formation of *n*-carboxylic acid nanorods on monolayer-protected metal nanoparticles on highly oriented pyrolytic graphite (HOPG) substrate via spin

coating. Another successful method is the formation of tetrathiafulvalene bromide ((TTF)$Br_{0.76}$) nanorods and partially oxidized potassium tetracyanoplatinate ($K_{1.75}Pt(CN)_4 \cdot 1.5H_2O$) nanorods on gold nanoparticles on HOPG by electrocrystallization. The confined nucleation and crystallization of the organic nanorods imposed by inorganic nanoparticles and their crystalline structures are investigated. This work contributes to the understanding of *SMN*, molecular ordering under nanoconfinement and engineering hybrid nanomaterials. The inorganic-organic hybrid nanomaterials with particle-rod structure can be applied to fabricate interconnected self-assembled hybrid networks and have potential applications in optical, bio-sensing and electronic areas.

In this dissertation, Chapter 2 presents the background and literature review on the subject in three aspects. The first aspect is the summary and prediction of the potential applications of hybrid materials. The second aspect is the basics of nucleation and crystallization theories including classical nucleation theory, seed-mediated nucleation theory and confined crystallization. The third aspect is the fundamentals of electrochemistry including electrochemical cell, thermodynamics and kinetics aspects, electrode reactions, electrodeposition and electrocrystallization.

Chapter 3 describes the principles and procedures of the experimental techniques used in this work. The main characterization techniques include Atomic Force Microscopy (AFM), Field-emission Scanning Electron Microscopy (FESEM), Transmission Electron Microscopy (TEM), *in situ* Energy Dispersive X-ray Spectroscopy (EDS), X-ray Diffraction (XRD). Electroanalytic methods, for

example, the cyclic voltammetry and the conductivity measurement are provided in detail.

Chapter 4 demonstrates the formation of carboxylic acid nanorods on monolayer-protected metal nanoparticles on HOPG via spin coating. 11-mercaptoundecanoic acid capped cadmium selenide (MUA-CdSe) nanoparticles and oleyamide capped gold (OA-Au) nanoparticles are used as nucleating seeds. The effects of the core and capping layer composition, the nanoparticle size, the chain length of the carboxylic acids on the carboxylic acid nanorod formation are investigated and the crystalline structure of the carboxylic acid nanorods is determined from the AFM results. The formation of the particle-rod hybrid structure and the confinement effect is also discussed in this chapter.

Chapter 5 illustrates the formation of $(TTF)Br_{0.76}$ nanorods on gold nanoparticles (GNPs) by electrocrystallization. In the first part of this chapter, the electrodeposition of GNPs on HOPG electrodes, the redox properties, surface area of active gold and electrochemical activity are analyzed by cyclic voltammetry (CV) and the GNP morphology is investigated by AFM and XRD. In the second part, the electrocrystallization of $(TTF)Br_{0.76}$, the crystallization conditions and the morphology of $(TTF)Br_{0.76}$ nanorods are investigated by AFM and FESEM. The formation mechanism and the crystalline structure of the $(TTF)Br_{0.76}$ nanorods are also explained in this chapter.

Chapter 6 shows another example of the formation of inorganic-organic hybrid nanomaterials with particle-rod structure by electrocrystallization. The crystallization conditions and the morphology of $K_{1.75}Pt(CN)_4 \cdot 1.5H_2O$ nanorods

on HOPG/GNP-decorated HOPG electrodes are investigated by AFM and FESEM. The conductivity of the $K_{1.75}Pt(CN)_4 \cdot 1.5H_2O$ nanorods is measured on prefabricated Au electrode patterns. The formation and the crystalline structure of the $K_{1.75}Pt(CN)_4 \cdot 1.5H_2O$ nanorods is interpreted in this chapter.

Chapter 7 summarizes the general conclusions from this work and suggestions for the future research. The overall conclusion is the successful fabrication of organic-inorganic hybrid nano-materials with particle-rod structures using either spin coating or electrocrystallization. The seed-mediated nucleation provides a universal strategy to integrate nano-components, which incorporate new functionalities and broaden the applications of the hybrid nano-materials.

CHAPTER 2

LITERATURE REVIEW

2.1 Potential Applications of Hybrid Architectures and Assemblies

2.1.1 Applications of metal nanoparticle/nanowire arrays

Metal nanoparticles exhibit unique physical and chemical properties due to their high surface-to-volume ratio and are applicable to surface plasmon, surface-enhanced Raman scattering, single-electron devices, ion-sensitive field-effect transistors, and photo-generations.[1] Gold nanoparticles have excellent optical, magnetic, electronic and catalytic properties and biocompatibility; thus, they have received significant interest in various applications, especially electrochemical applications in bioassay, biosensor, chemical sensor, and electrocatalysis.[2]

Gold nanoparticle arrays functionalized with thiols can be used as chemiresistor sensors to detect analytes in aqueous solution. Copper et al. used a range of hydrophobic and hydrophilic thiol modified gold nanoparticle arrays to discriminate simple alcohols dissolved in artificial seawater.[3] The advantage of this sensor is the possibility of tuning the sensor selectivity by functionalizing the gold nanoparticles with different thiols.

Tokonami et al. prepared open bridge-structured gold nanoparticle arrays with precisely controlled gaps in nanometers on platinum microelectrodes.[4-5] The combination of the nanogap electrode and conductive DNA can measure small electrical property changes in DNA with a high *S/N* ratio and amplify the distinction of the mismatch in the DNA sequence. Thus, the gold nanoparticle array film electrode is highly selective to detect DNA polymorphism.

Metal nanowires have been used for the fabrication of chemical sensors and biosensors recently. Most nanowires composed of metal oxides, such as ZnO, TiO, and *etc.*, and conductive polymers, such as PT and Ppy, have been applied to chemical sensors for gases. Penner's group successfully fabricated hydrogen sensors and switches from Palladium (Pd) nanowire arrays.[6-8] The Pd nanowire arrays were synthesized electrochemically on HOPG electrode using step-edge decoration method. The H_2 sensor consisting of Pd nanowires is based on the resistivity changes of the nanowires, that is, the resistance of the Pd nanowire arrays decreases in the presence of H2 due to break junction mechanism.

2.1.2 Applications of organic crystals

In recent years, remarkable progress has been made in the field of organic electronic devices such as organic light-emitting diodes (OLEDs), thin-film transistors (OTFTs), photovoltaic cells (OPVCs), sensors, memory cells, and light-emitting transistors.[9-10]

Ken-Hoong et al. used thin-film transfer-printing technique to make a multi-layered conjugated-polymer film for organic optoelectronic devices.[11] The fabricated devices show equal performance to either blend devices or bi-layer devices prepared by other techniques, indicating the well-controlled organic-organic interfaces. This technique can be repeated to fabricate multilayered conjugated-polymer film for new electronic devices.

Carbon nanotubes (CNTs) have novel electrical properties that make them useful for electronic devices and biosensors. Essig et al. recently reported the

phonon-assisted light emission from metallic single-wall carbon nanotubes (SWNTs), multiwall carbon nanotubes (MWNTs) and few-layer graphene (FLG).[12] For all carbon nanotubes and graphene devices, there are two universal electroluminescence peaks near 1.3 and 1.8 eV. Essig et al. attribute the electroluminescence to phonon-assisted radioactive decay from π* band states at the M point to the Fermi level at the κ point.

Enzyme-coated carbon nanotubes have been recently exploited in biosensors and biolabels with enhanced sensitivity. Besteman et al. created the glucose oxidase (GOx) - coated semiconducting SWNTs which are sensitive to pH changes and increase conductance upon adding glucose.[13] This is the first enzyme-activity biosensor based on SWNTs.

Munge et al. electrochemically detected proteins and nucleic acids using electrostatic layer-by-layer (LbL) self-assembled enzyme multi-layers, protein-polyion, on SWNT.[14] Bi et al. further utilized Munge et al.'s method to fabricate LbL self-assembled horseradish peroxidase (HRP)-polyion multilayers on MWNTs.[15] The biosensor exhibits a low detection limit, high sensitivity, good precision and operational stability.

Wang et al. also applied the LbL technique to fabricate the glucose biosensors using multi-layer of GOx-SWNT.[16] The sensor sensitivity could be controlled by the number of GOx-SWNT bilayers during fabrication. One additional GOx-SWNT bilayer increases the electrochemical response 2 - 4 times and the enzymatic response to glucose 6 - 17 times.

2.1.3 Potential applications of hybrid assemblies.

The organic/inorganic hybrid nanostructures with engineered particle/rod structures are of extensive scientific and technological interest due to their multifunctional capabilities with combined or enhanced optical and electrical properties and have potential electrochemical applications in electronic devices, sensors, and electrocatalysis.[17-22]

Buonsanti et al. synthesized magnetic-semiconductor particle-rod hybrids by growing spherical Fe_xO_y epitaxially at either on apex or any location along the longitudinal sidewalls of TiO_2 rods in a hot surfactant environment.[23-24] The $Fe(CO)_5$ - TiO_2 hybrids by reacting tapered *b*-TiO_2 nanorod seeds with different sizes and aspect ratios with varying amount of $Fe(CO)_5$. The hybrids exhibit enhanced magnetic and photocatalytic properties compared with their individual components and physical mixture.

Shi et al. synthesized gold (Au)/CNTs hybrid catalysts by modifying CNTs and attaching gold nanoparticles in one-step.[25] The gold nanoparticles disperse uniformly on the CNT surfaces. The uniform dispersion of gold nanoparticles enhances the electrochemical catalytic activity of Au/CNT hybrids for oxygen reduction reaction (ORR). The Au/CNT hybrids have potential application in sensors, optical electronics, electrocatalysis and proton exchange membrane fuel cells (PEMFC).

Inorganic nanoparticle-DNA hybrids are also applicable in biological and biochemical fields.[20, 22] Soundrapandian et al. reviewed the advantages of organic-inorganic hybrids in bone drug delivery such as the enhanced ability to

release drugs, adopting to the natural environment and supporting the local area until complete bone regeneration.[26]

In summary, hybrid structures composed of inorganic and organic parts are capable of controlling the desired optical and electrical properties by adjusting the chemical composition and geometry of individual components. A remaining challenge is to incorporate the inorganic and organic parts to form hybrid structure. One possible method is to grow organic crystals from inorganic particles based on seed-mediated nucleation via solvent evaporation or electrochemistry.

2.2 Basics of Nucleation and Crystallization

2.2.1 Concepts in crystallization

Crystallization as a solid-liquid phase transition process involves two main stages, nucleation and crystal growth. Nucleation is the initial stage of crystallization, where the solute molecules start to gather into clusters and form nuclei. In most cases, nucleation is heterogeneous and occurs in the presence of foreign bodies, *i.e.* nucleation sites, such as phase boundaries, microclusters, macromolecules and impurities like dusts. Homogeneous nucleation occurs spontaneously and randomly without preferred nucleation sites and requires more nucleation energy. The subsequent stage of crystallization is crystal growth, where the crystals grow into desired size from supersaturated solutions. The main crystal growth methods include but not limited to cooling, evaporation, soxhlet extraction, diffusion, sublimation and convection.

Polymorphism, an important concept in crystallization, is the ability of a compound to exist as two or more crystalline phases. It usually consists of packing polymorphism which is due to the crystal packing difference, conformational polymorphism, which is due to different conformers and pseudo-polymorphism which is due to hydration or solvation. Different polymorphs can exhibit distinct physical and chemical properties. Therefore, controlling polymorphism during crystallization process is critical to produce a wide variety of materials in food, pharmaceutical and pigment industries. Commonly used controlling methods include supersaturation, the nucleation temperature, choice of solvent, usage of additives, external fields and surface templating.

Crystal size distribution (CSD) is an essential criterion used in industry to examine the crystal qualities during crystallization process. A narrow distribution of crystal size is favorable in industrial application as a result of good filtering, drying and free-flow ability. A related phenomenon is the thermodynamically-driven spontaneous process, Ostwald ripening, where larger particles are more energetically favored than smaller particles during crystal growth. Therefore, larger crystals become larger and small crystals become smaller or disappear over time which resulted in larger crystal size distribution.

Crystallization is a fundamental separation and purification process in a variety of industries such as fine chemical, food, pharmaceutical and pigment industries. In pharmaceutical researches, it is important to understand structure-property/function relationship in protein studies and separate the intermediates and the final products in the manufacture of active pharmaceutical ingredients. In

pigment industries, the pigment performance such as the color, fastness, the ability to resist chemical and physical factors, are influenced by the crystallinity, polymorphism, crystal size and shape.

However, there are still unsolved problems remaining in crystallization. One unanswered question is the smallest nucleus size needed to initiate crystallization process inquired by Ostwald more than one hundred years ago.[27] Another dominant challenge in crystallization is to visualize or capture the initial stage of crystallization or the nucleation process which requires high resolution and fast imaging techniques, for example, the atomic force microscopy (AFM). The understanding of the nucleation process is essential in solving the problems such as preparing single crystal and controlling the polymorphism.

2.2.2 Classical nucleation theory (*CNT*)

In the classical nucleation theory (*CNT*)[28], the free energy change to form a cluster of *n* molecules (ΔG) is related to the chemical potential difference ($\Delta\mu$) and the total surface energy of the *n*-sized cluster (Φ_n) as in Equation 1.

$$\Delta G = -n\Delta\mu + \Phi_n. \quad \text{(Equation 1)}$$

The nucleating species has to overcome an energy barrier to initiate nucleation. The nucleation energy barrier is attributed to two-conservancy effects: one is the lowering of the free energy due to the formation of the stable crystalline phase; the other is the increase of the interfacial free energy due to the interfacial area increasing as the clusters growing. The maximum value of free energy change (ΔG^*) is the nucleation barrier with the cluster radius defined as the critical nucleus size (r_c). The clusters need to be larger than r_c to

overcome the nucleation energy barrier and grow into stable crystals. The sub-clusters or the clusters with radius less than r_c are unstable and tend to dissolve in the system. The larger clusters, called supernuclei or nuclei will grow spontaneously to reach macroscopic sizes.

In thermodynamic view, the driving force for nucleation is the chemical potential difference $\Delta\mu$ between the mother phase, *i.e.* the solution or melt phase, and the crystal phase (Equation 2).

$$\Delta\mu = \mu_{mother} - \mu_{crystal}. \quad \text{(Equation 2)}$$

The system is considered as undersaturated if $\Delta\mu < 0$, in equilibrium if $\Delta\mu = 0$, and supersaturated if $\Delta\mu > 0$. When equilibrium, the chemical potential of the crystal phase ($\mu_{crystal}$) can by replaced by the chemical potential of the mother phase in equilibrium (μ_{eq}).

In case of crystallization from solutions, the chemical potential of the nucleating specie *i* is related to its activity (a_i), which can be simplified as its concentration (C_i) in Equation 3.

$$\mu_i = \mu_i^0 + kT \ln a_i \approx \mu_i^0 + kT \ln C_i. \quad \text{(Equation 3)}$$

where μ_i^0 is the standard state (a_i=1) of the chemical potential of species *i*. Therefore, $\Delta\mu$ is derived as the following equation.

$$\Delta\mu = \mu_i^0 + kT \ln \frac{a_i}{a_i^{eq}} \approx \mu_i^0 + kT \ln \frac{C_i}{C_i^{eq}}. \quad \text{(Equation 4)}$$

Define supersaturation (σ) as the percentage of the activity or concentration difference:

$$\sigma = (a_i - a_i^{eq}) / a_i \approx (C_i - C_i^{eq}) / C_i. \text{(Equation 5)}$$

The chemical potential difference is then expressed simply with supersaturation in Equation 6.

$$\Delta\mu = kT\ln(1+\sigma). \quad \text{(Equation 6)}$$

$$\Delta\mu \approx kT\ln\sigma, \text{ if } \sigma < 1. \quad \text{(Equation 7)}$$

In case of crystallization from melts, $\Delta\mu = s_m\Delta T$, where s_m is the entropy of melting per molecule and ΔT is supercooling ($\Delta T = T_m - T$).

In case of electrodeposition and electrocrystallization, $\Delta\mu$ is a function of the ion valence (z_i) of deposit specie *i*, the electron charge (*e*), and the overpotential (η):

$$\Delta\mu = z_i e\eta, \ \eta = (E - E_{eq}). \quad \text{(Equation 8)}$$

where η is the difference between actual electrode potential (E) and the equilibrium potential of the deposit specie (E_{eq}). More detailed information on electro-deposition and electro-crystallization is discussed in Chapter 2.3.

In nucleation kinetics, the most important parameter is the nucleation rate (J) as the number of nuclei created per unit volume-time. In equilibrium state, $J = 0$. In steady state, J is independent of time. For homogeneous nucleation, the nucleation rate is expressed as a function of the nucleation energy barrier in Equation 9.

$$J = K\exp\left(-\frac{\Delta G^*_{\text{homo}}}{kT}\right). \quad \text{(Equation 9)}$$

For heterogeneous nucleation, J is proportional to the density and the surface area of nucleating species. In non-steady state, the equation for J is very complex and also related with time.

2.2.3 Seed-mediated nucleation (*SMN*)

In heterogeneous seed-mediated nucleation (*SMN)*, a foreign particle seed lowers the nucleation energy barrier and promotes nucleation at lower supersaturation.[29-30] Figure 1 is schematic illustration of the nucleation occurs on a foreign particle seed.

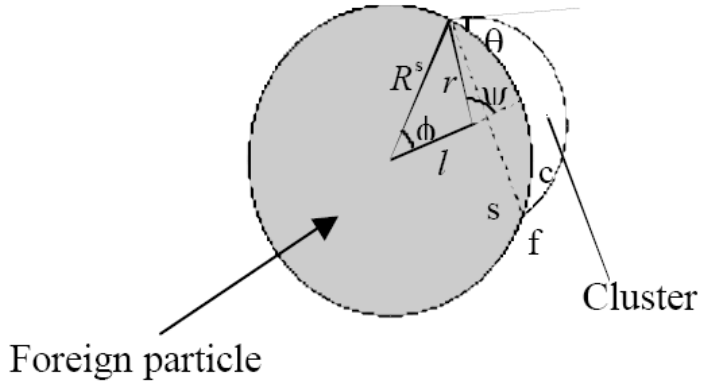

Figure 1. Scheme of seed-mediated nucleation. (Reprinted with permission from *Advances in Crystal Growth Research* 2001. Copyright © 2001, Elsevier.)

To define the lowering of the nucleation energy barrier due to the foreign seed, a heterogeneity factor *f* is introduced as the ratio of the heterogeneous nucleation barrier (ΔG^*_{heter}) and homogeneous nucleation barrier (ΔG^*_{homo}).

$$f = \frac{\Delta G^*_{\text{heter}}}{\Delta G^*_{\text{homo}}}. \quad \text{(Equation 10)}$$

where $0 < f \leq 1$ by definition. Assume the nucleation occurs at a foreign seed with a radius of R_s, the nucleation barrier is a function of $\Delta\mu$, the volume (V), the volume per structure unit (Ω), the surface area (S) and the interfacial energy between phases i and j , γ_{ij}, as shown in Equation 11.

$$\Delta G = \frac{-\Delta\mu V_c}{\Omega} + \gamma_{cf} S_{cf} + (\gamma_{sf} - \gamma_{sc}) S_{sc}. \quad \text{(Equation 11)}$$

where the subscript *f*, *c* and *s* in the interfacial energy term stand for the mother phase, the cluster of the crystalline phase and the foreign seed, respectively.

The *f* value is mainly influenced by two parameters, the contact angle between the nucleus and the seed surface (θ) and the normalized radius of curvature of the foreign seed (R'). To simplify,

$$f = f(m, R') \quad \text{(Equation 12)}$$

where

$$m = \frac{\gamma_{sf} - \gamma_{sc}}{\gamma_{cf}} \approx \cos\theta, \ (-1 \le m \le 1) \quad \text{(Equation 13)}$$

and

$$R' = R^s / r_c, r_c = \frac{2\Omega\gamma_{cf}}{kT\ln(1+\sigma)}. \quad \text{(Equation 14)}$$

Figure 2 shows $f(m, R')$ as a function of R' for a given m. The $f(m, R')$ plots can be divided into three regimes: 1) Zero-effect regime, when $R' < 0.1$, f is close to 1, which indicates that the foreign seed is too small to initiate nucleation; 2) Non-linear regime, when $0.1 \le R' \le 10$, f is a function of both R' and m. f value decreases with increasing m and R' (decreasing r_c or increasing σ); 3) Linear regime, when $R' > 10$, f is only a function of m, the foreign seed is much larger than the critical nucleus and acts as a flat surface to the nucleating phase. There is no curvature effect imposed by the seed to the nucleating specie.

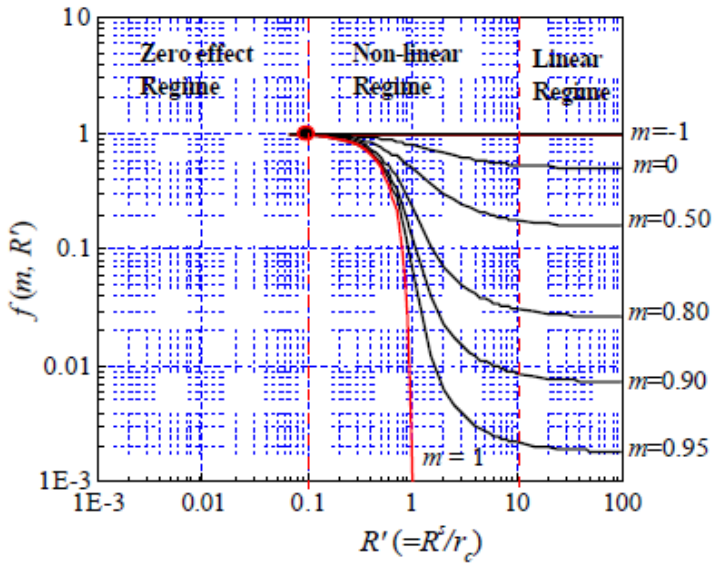

Figure 2. Dependence of the heterogeneity factor $f(m, R')$ on m and R'. (Reprinted with permission from *Advances in Crystal Growth Research* 2001. Copyright © 2001, Elsevier.)

Consider the contact angle effect. When $\theta \rightarrow 180°$, $m \rightarrow 1$, and $f \rightarrow 0$, the solution wet the seed surface and promotes nucleation on the foreign seed. In this case, by the definition of m in Equation 13, $\gamma_{sc} \rightarrow 0$ and $\gamma_{sf} \approx \gamma_{cf}$, which require perfect structural match with the strongest average interaction or the lowest interfacial energy between the foreign seed surface and the nucleating phase. On the other hand, if $\theta \rightarrow 0°$, $m \rightarrow -1$, and $f \rightarrow 1$, the structure match is poor and the solution cannot wet the surface, therefore, the foreign seed is ineffective in nucleation and the nucleation is more likely to be homogeneous.

2.2.4 Confinement in crystallization

2.2.4.1 Crystallization confined by nano-pores

Crystals growing in well-defined pores close to the critical nucleus size display unique characteristics of nucleation due to the confinement effect of the pores imposed on the nuclei.

Chayen et al. have manipulated protein heterogeneous nucleation and crystallization by using porous material as a confinement medium.[31-32] The porous materials they have investigated are porous silicon with pore size of 5 -10 nm and gel-glass with pore size of 2 -10 nm. Their results showed several protein crystals growing on and/or in the proximity of porous silicon fragments. The results also clearly indicated that the phycobiliprotein still attached to the silicon fragment even after moving the fragment. The porous silicon coated wafer pieces are more effective in constraining protein molecules and promoting crystallization than other porous materials based on two desired properties: 1) the pore size comparable with the protein molecule size and 2) the wide distribution of pore shape and size.

The Ward's group has done a series of studies using similar approach to control crystallization of organic materials in nano-scale chambers.[33-38] One porous material they have investigated is the controlled pore glass (CPG) powders with pore diameter varied from 7 to 55 nm. The CPG have random pores which permits the infiltration of the melts of compounds with high melting points and also the characterization of the thermotropic properties of embedded crystals at elevated temperatures. One finding is that the melting points of the

crystals decrease with decreasing channel diameter, which is consistent with their increased surface-area-to-volume ratio. Another group of porous materials is the porous block-polymer-derived plastic monoliths with pore diameter varied from 10 to 40 nm. The porous plastic monoliths are poly(cyclohexylethylene) (*p*-PCHE) which have highly order hexagonal array of hydrophobic cylindrical pores (dia. ≈ 30 nm). The porous plastic monolith permits studies such as selective formation of metastable amorphous and crystalline phases, size-dependent polymorphism at different pore sizes, formation of new polymorphs; examination and manipulation of nanocrystal orientation with respect to the pore direction.

2.2.4.2 Crystallization confined by nanopatterns

Micropatterns of self-assmbled monolayers have been used to control crystallization by relying on guest molecules to recognize different surface functional groups and by microconfinement. HOPG-induced alkane patterns provide confinement size less than 50 nm, which is generally below the limit of lithography. The molecular patterns formed by alkyl amphiphiles with a variety of functional groups with periodic active sites separated by inactive barriers have the potential to generate diverse host-guest structures through a wide range of intermolecular interactions.

Mao's group used 1,2-dimyristoyl-sn-glycero-3-phosphoethanolamine (DMPE) bilayer pattern to direct and confine the molecular crystallization of Aspirin on HOPG.[39] DMPE forms an alternative hydrophobic-hydrophilic bilayer pattern with a periodicity of ~ 5.2 nm, which is identical to the bilayer unit cell on HOPG by spin coating. Aspirin molecules adsorb only on the hydrophobic interior

of the DMPE bilayer stripe when spin coating from the Aspirin and DMPE alcoholic mixture. The structure analysis of the co-deposited film revealed that DMPE bilayer pattern Aspirin forms metastable or amorphous dimer rods along the direction perpendicular to bilayer stripes via aggregation. Therefore, the DMPE bilayer pattern provides the size limit to inhibit the crystallization of Aspirin molecules in the length of the bilayer.

Mao's group also fabricated copper sulfide nanorod arrays on eicosanoic acid bilayer pattern on HOPG.[40-41] Eicosanoic acid self assembles into monolayer stripe pattern with periodicity of 5.6 nm on HOPG via spin coating. The co-deposited film of the copper sulfate and eicosanoic acid displays a distorted stripe pattern with similar periodicity of 5.6 nm via spin coating. The complexation of the two components is between the copper ion and the carboxyl group of eicosanoic acid through metal coordination or ion exchange. The co-deposited film is then reacted with hydrogen sulfite (H_2S) to convert the embedded copper ions into copper sulfide nanocrystals. The resulting copper sulfide crystals restore the unidirectional orientation of the stripe patterns with unchanged periodicity of 5.6 nm and form nano-crystal arrays with a typical length of 35 nm and height of only 0.8 nm.

2.2.4.3 Crystallization confined by nanoparticles

The nanoconfinement effect probes the impact of size and shape of the critical nucleus on crystal growth according to seed-mediated nucleation. Mao's group first reported the formation of eicosanoic acid ($C_{20}A$) nanorods on 11-mercaptoundecanoic acid capped cadmium selenide (MUA-CdSe) nanoparticles

as illustrated in Figure 3.[42] The MUA-CdSe nanoparticles with height of 3.5 to 30 nm disturb the $C_{20}A$ self assembly and form one-dimensional nanorods via spin coating of the mixture of MUA-CdSe nanoparticles and $C_{20}A$ on HOPG. The $C_{20}A$ nanorods have uniform height (= 1.0 nm) and width (= 5.4 nm), which is identical to the unit cell lengths along the *a* and *c* axes of the C-form carboxylic acid crystal structure.[43] The particle/rod hybrid nanostructure provides strong evidence of the confined crystallization imposed by the nanoparticle based on seed-mediated nucleation.

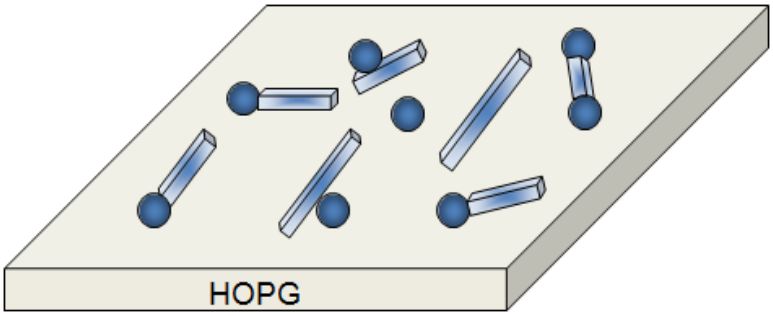

Figure 3. Redraw the schematic illustration of $C_{20}A$ nanorods growing on MUA-CdSe nanoparticles on HOPG by spin coating.

Cacciuto and Frankel have performed molecular simulation of spherical seed particles (with radius of R_s) on the crystallization of uncharged monodispersed spherical colloids (with diameter of D).[44-45] The simulation results showed that when the seed size is very small, *e.g.* $R_s \leq 4D$, crystal nuclei typically form in the bulk, rather than on the seed; When seed size is large, *e.g.* $R_s \geq 7D$, it tends to produce one single crystal that grows to macroscopic size as indicated in Figure 4 bottom scheme; When $R_s = 5D$, very small nuclei appear on the seed surface and tend to grow radially outward until they detach and move away into the bulk as shown in Figure 4 top scheme. The remaining seeds keep

on producing crystal nuclei which resulted in more crystallites over the seeds and smaller final crystals. It is assumed that the molecular rod is induced by the high curvature of the small seed.

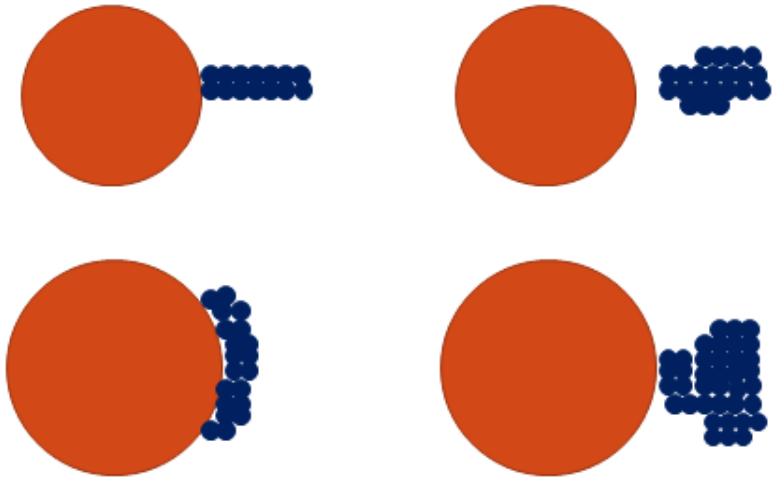

Figure 4. Redraw the schematic illustration of molecular simulations of colloidal crystallization on particle seed with $R_s = 5D$ (top) and $R_s = 7D$ (bottom).

2.3 Fundamental Aspect of Electrochemistry and Electrocrystallization

2.3.1 Electrochemical cell type and setup

Electrochemistry studies chemical redox reactions at the solid/liquid interface, which involve electron transfer at the interface of the electrode, an electron conductor, and the electrolyte, an ionic conductor.[46]

Depending on the spontaneity of the redox reaction, the electrochemical cell is characterized as two kinds, the Galvanic cell and the Electrolytic cell. If the redox reactions occur spontaneously at the electrodes when they are connected externally by a conductor, which is usually a salt bridge or a membrane, the cell is called the Galvanic cell. Examples of Galvanic cell are such as batteries, fuel cells and *etc*. In Electrolytic Cell, the redox reaction occurs with an external electric energy consisting of two half cell: the oxidation process occurred at the

anode, and the reduction process at the cathode. Examples of electrolytic cell which commonly used to decompose chemical compounds are such as electrolytic syntheses, electrorefining, and electroplating.

Modern electrochemical cell uses three-electrode system instead of the conventional two-electrode system with cathode and anode. The first electrode is the working electrode (WE) where the reaction of interest occurs. The common material for working electrode is metal such as Platinum (Pt) and gold (Au), Mercury and carbon including HOPG, carbon nanotube (CNT) and glassy carbon (GC) which is specially used in non-aqueous solution. The second electrode is the counter (CE), sometimes called auxiliary electrode, which is to balance the charge added or removed by the working electrode. Typical counter electrode is Pt plate or Pt wire. The third electrode is reference electrode, which has constant chemical composition to produce constant potential and is acting as reference in measuring and controlling the working electrodes potential without passing any current.

There's a variety of reference electrodes available depending on the solvent used in the electrochemical cell. Commonly used reference electrodes for aqueous solutions are saturated calomel electrode (SCE, E = +0.244 V) and silver chloride electrode (Ag/AgCl, E = +0.197 V saturated). The saturated KCl provides constant Cl^- concentration as well as constant potential. For electrochemical reactions occurring in non-aqueous solutions, $Ag/AgNO_3$ in acetonitrile is sometimes used to reduce the liquid-liquid junction potential caused by aqueous electrodes, for example, SCE and Ag/AgCl. Another group of

reference electrodes is called pseudo-reference electrode simply using Pt or Ag wire as RE. The potential of pseudo-reference electrode is not constant but can be calculated from the electrolyte composition and concentration.

Potentiostat is used to apply and control potential or current as the external electrical energy for three-electrode system. The cell voltage is the potential difference between the working and reference electrode.

The electrolyte solution usually contains the electroactive species as well as the supporting electrolyte. The electroactive species is one that can donate or accept electrons at the working electrode. Supporting electrolyte is added to reduce the solution resistivity.

2.3.2 Electrode reactions

2.3.2.1 Faradic process and non-faradic process

Faraday's Law is a fundamental quantitative relationship for electrochemical reactions: the amount of chemical reaction caused by the flow of current is proportional to the amount of electricity passed. Therefore, the electrode reactions are easily defined as two kinds, the Faradaic process and the nonfaradaic process.[46] Faradaic process is the chemical process that follows the Faraday's Law and is useful in studying the charge transfer at the interface, which is the electrode redox reaction. On the other hand, nonfaradaic process is the process that disobeys the Faraday's Law. Nonfaradaic process is used to investigate adsorption and desorption at the interface without charge transfer. The structure of the electrode-solution interface can alter with changing potential or solution composition.

2.3.2.2 Electric double layer

For nonfaradaic process, the behavior of the electrode-electrolyte interface without charge transfer is analogous to that of a capacitor. The capacitance (C) is the ratio of the charge stored on the capacitor (q) and the potential across it (E). At a given potential, the charge on the metal electrode (q^M) and the charge in the solution (q^S), follows the equation:

$$q^M = - q^S \quad \text{(Equation 15)}$$

which is often written in terms of charge density as

$$\sigma^M = - \sigma^S \quad \text{(Equation 16)}$$

where $\sigma = q/A$ ($\mu C/cm^2$).

The well established theory for the electrode/electrolyte interface is the electric double layer including the Helmholtz layer and the diffuse layer.[46] The inner Helmholtz (or Stern) layer contains solvent molecules and sometimes other species (ions or molecules) that are specifically adsorbed. The centers of those specifically adsorbed ions form the inner Helmholtz plane (IHP), with distance of x_1, and total charge density of σ^i. The centers of the nearest solvated ions form the outer Helmholtz plane (OHP), at distance x_2. The diffuse layer extends from the OHP into the bulk of the solution with nonspecifically adsorbed ions distributed in a 3D region with charge density of σ^d. Therefore, the Equation 16 is rewritten as

$$\sigma^S = \sigma^i + \sigma^d = - \sigma^M. \quad \text{(Equation 17)}$$

In general, the double-layer capacitance (C_d) is in the range of 10 - 40 $\mu F/cm^2$. The thickness of the diffuse layer depends on the total ionic

concentration in the solution. The structure of the double layer can affect the rated electrode processes.

2.3.2.3 Thermodynamics and kinetics in electrochemistry

Faradaic Process is used to study the redox reactions at the electrode/electrolyte interface. Thermodynamically, for a given redox reaction,

$$aA + bB \leftrightarrow cC + dD$$

the free energy term is written as

$$\Delta G_{rxn} = -RT \ln Q \text{ . (Equation 18)}$$

where $Q = \frac{[C]^c[D]^d}{[A]^a[B]^b}$.

In an electrochemical cell, the free energy term for the above redox reaction is also expressed as

$$\Delta G_{rxn} = -nFE_{cell} \text{ . (Equation 19)}$$

When $E_{cell} > 0$, $\Delta G < 0$, the reaction occurs spontaneously.

The cell potential can be then derived from Equation 18 and 19 as the Nernst equation

$$E = E^0 - \frac{RT}{nF} \ln \frac{[C]^c[D]^d}{[A]^a[B]^b} \text{ . (Equation 20)}$$

or

$$E = E^0 - \frac{0.0592}{n} \log Q \ (298\text{K}) \text{ . (Equation 21)}$$

The electrode reaction rate is usually expressed by the number of charge transferred at the electrode/electrolyte interface per electrode area per time. Equation 22 is the formula for electrode reaction rate

$$\upsilon_{rxn}\left(mol \times s^{-1} \times cm^{-2}\right) = \frac{i}{nFA} = \frac{j}{nF}.$$ (Equation 22)

where J is the current density (A/cm^2).

In general, the cell current is governed by the rates of processes, such as mass transfer, electron transfer at the electrode surface, chemical reactions, and other surface reactions (adsorption, desorption, crystallization, electrodeposition). Electrode reaction kinetics is also affected by the electrode surface cleanliness, surface microstructure, and surface chemistry.

Mass transfer is the movement of material from one location in solution to another. The mass transfer to an electrode is governed by the Nernst-Planck Equation, which is written as in Equation 23 along the x-axis for one-dimensional mass transfer:

$$J_i(x) = -D_i \frac{\partial C_i(x)}{\partial x} - \frac{z_i F}{RT} D_i C_i \frac{\partial \phi(x)}{\partial x} + C_i \upsilon(x).$$ (Equation 23)

where $J_i(x)$ is the flux of species i (mol s^{-1}cm^{-2}) at distance x from the electrode surface, D_i is the diffusion coefficient (cm^2/s), $\partial C_i(x)/\partial x$ is the concentration gradient at distance x, $\partial \phi(x)/\partial x$ is the potential gradient, z_i and C_i are the charge and concentration (mol/cm^3) of species i, respectively, and $v(x)$ is the velocity (cm/s) of materials moves along the x axis. The three terms on the right hand side of Equation 23 correspond to the flux diffusion, migration and convection, respectively. Diffusion is contributed to the movement of species with concentration gradient (or the gradient of chemical potential). Migration is contributed to the movement of ions with potential gradient in electric field and is negligible by adding supporting electrolyte. Convection is due to stirring or

hydrodynamic transport and can be avoided by preventing stirring and vibrations in the cell.

2.3.3 Electrodeposition and electrocrystallization

Electrodeposition and electrocrystallization are widely used electrochemical techniques to synthesize metal, metal oxide, and conductive organic materials. The advantages of electrochemical synthesis over vapor deposition techniques are such as high purity, high selectivity, low processing temperature and precise control of crystal growth via overpotential and charge density.[47] In this dissertation, electrodeposition is specified as the electrochemical deposition of metal and metal related materials and electrocrystallization is used for the electrochemical crystallization of conductive organic crystals.

2.3.3.1 Electrochemical nucleation theory

Electrochemical nucleation takes place at the boundary between two phases: the electrode, usually a metal, and the electrolyte solution, in which the charge carrier ions interchange electrons with the electrode.[48] Thus the electrochemical nucleation is heterogeneous in nature. The generated radical species may precipitate with neutral molecules and/or counterions on the electrode under suitable conditions of concentration, solvent, temperature, and current density, regardless of the crystal solubility in the solvent. Supersaturation at the crystal surface can be precisely controlled by varying the electrochemical potential, having the same effect as changing the solute concentration in conventional crystallization processes.

In chapter 2.1, the chemical potential difference for electrodeposition and electrocrystallization is expressed in Equation 8. The driving force for electrochemical nucleation is the overpotential which is the additional potential beyond the thermodynamic requirement needed to initiate a reaction. The concept of overpotential is analogous to the supersaturation for solution crystallization and can be achieved by two different ways as expressed in the following equations[49]:

$$\eta = | E - E_{eq} | .$$ (Equation 24)

$$\eta = \frac{kT}{ze} \ln \frac{a}{a_{eq}} .$$ (Equation 25)

In the first way, the overpotential is achieved by keeping the solution activity constant and changing the working electrode potential to more negative value for reduction process or more positive value for oxidation process. In the second way, the supersaturation is to make the solution activity higher than its equilibrium value and keep the working electrode potential constant. The advantage of the second way is to preserve the energy state of the electrode surface.

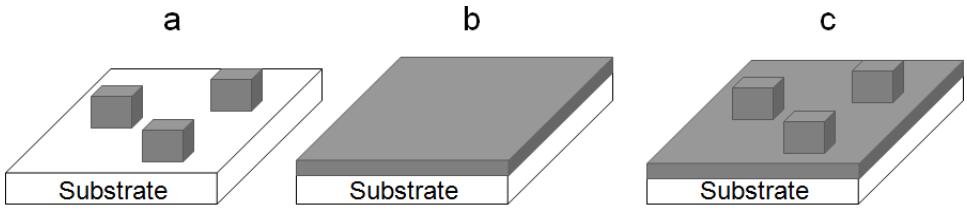

Figure 5. Scheme of nucleation and growth mechanisms on foreign surface: (a) Volmer-Weber growth; (b) Frank-van der Merwe growth; and (c) Stranski-Krastanov growth.

Figure 5 illustrates three nucleation and growth mechanisms for electrodeposition and electrocrystallization on a foreign substrate.[50-51] The first type of nucleation and growth is Volmer-Weber or Island growth which is characterized as 3D crystal growth with broad size distribution upon time. The formation of the 3D crystals is due to the weak interaction between the nucleating species and the foreign surface. For example, the metals deposit into particles or rods at low energy surfaces (e.g. H-terminated silicon and graphite) due to the weak van der Waals contact with the surface. The second type is the Frank-van der Merwe growth which is characterized by layer-by-layer growth mode. The layer-by layer deposition can be achieved by underpotential deposition technique when the interaction between the depositing species and the surface is stronger than the deposit molecules. The Stranski-Krastanov growth is layer-by-layer deposition followed by 3D growth which also occurs on surface with strong interaction with depositing species. For instance, at high energy surfaces (e.g. noble metals), metal deposits form a 2D film at the initial stage and the film acts as a foreign surface for 3D crystal growth at high overpotential.

In colloidal synthesis, if the nucleation of new particles occurs “progressively” during growth as shown in Figure 6 (top), the growth durations for individual particles will be distributed in time and a broad size distribution will be obtained. Ideally, nucleation occurs “instantaneously”, which means the nucleation time is short relative to the crystal growth time and can be considered as uniform growth as in Figure 6 (bottom).[52]

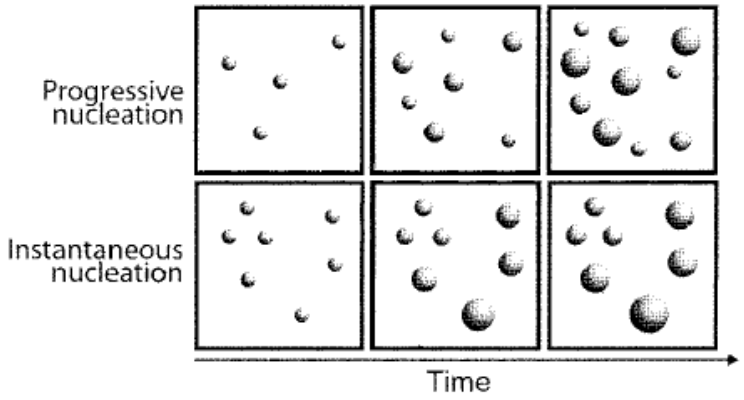

Figure 6. Scheme of progressive and instantaneous nucleation. (Reprinted with permission from *J. Phys. Chem. B*, 2002, 106 (13), pp 3339–3353. Copyright (2002) American Chemical Society.)

Consider the 3D crystal growth on a surface, the crystal size distribution is broadened due to 1) random nucleation on terrace and aligned nucleation at step edges, which is called “pseudo-random” nucleation, and 2) “Interparticle diffusion coupling” (IDC), that is, the crystal growth depends on the number and proximity of neighboring particles due to depletion zone. One way to narrow the size distribution is to use slow growth method which reduce the radius of the depletion layer and eliminate the interparticle diffusion coupling. The simulation results by Penner’s group predicted that lowering the applied overpotential reduces the depletion layer around the particles and changes the diffusion control to kinetic control as illustrated in Figure 7.[52] Their experimental results further proved that their “two-pulse” method, short nucleation pulse at high overpotential and then long crystal growth pulse at low overpotential, successfully produced Au, Ag and Pt nanoparticles with narrow size distribution by electrodeposition.[53-54]

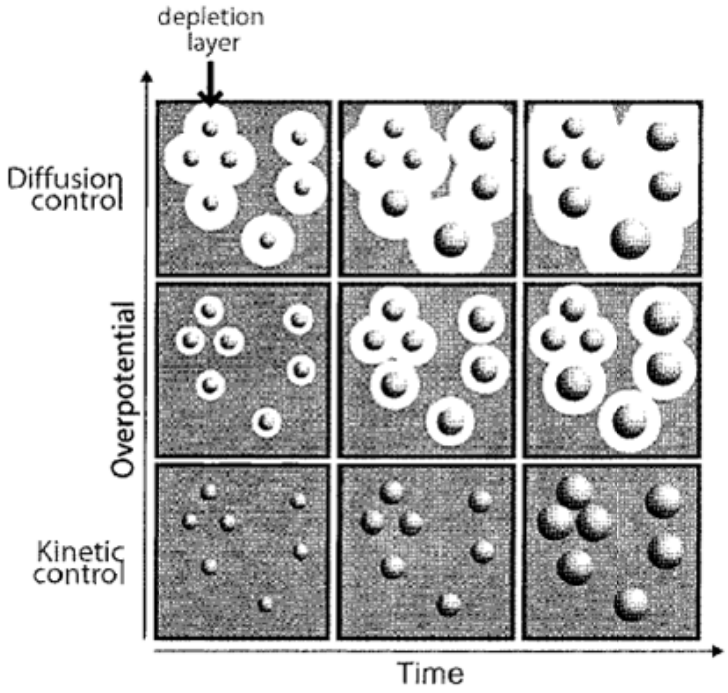

Figure 7. Scheme of the effect of overpotential on the size distribution of metal particles as a function of deposition time. (Reprinted with permission from *J. Phys. Chem. B*, 2002, 106 (13), pp 3339–3353. Copyright (2002) American Chemical Society.)

2.3.3.2 Electrodeposition of inorganic metals

Electrodeposition is widely used to synthesize metals, metal oxides and metal alloys with various shapes such as particles, rods and wires on different electrodes which are conductive substrates such as Au, Pt, GC, ITO (Indium tin oxide film) and *etc*. The metal particle/rod/wire decorated electrode often shows improved electric properties compared with the bare electrode which has potential applications in catalysis, electronic devices and sensors.

A majority of the recent developments focuses on the electrodeposition of Au, Ag or Pt nanoparticles on Si/SiO_2 substrate, HOPG, ITO (Indium tin oxide film), GC electrode, and gold (111) single-crystalline sheet.[53, 55-59] The metal

nanoparticle electrodeposition is simply achieved by using corresponding salt solutions such as $HAuCl_4$, $AgNO_3$, and H_2PtCl_6 aqueous solutions with appropriate supporting electrolytes and applying potentials in the reduction region of the redox species.

Boxley *et al*. investigated the electrochemical deposition and reoxidation of Au on HOPG electrode using SEM and AFM.[60] The Au nanoparticles preferred to deposit on the surface defects and the upper plane of step edges. The deposited Au nanoparticles present three morphologies upon deposition time. In the first stage, high density of Au nanoparticles with diameter < 10 nm are formed on HOPG when the deposition time is less than 1s. In the second stage, a small percentage of the au nanoparticles continue to grow into Au crystallites with diameter of ~ 300nm as the deposition time extended to ~50 s. Finally, the Au crystallites coalesce and form large crystallites (> 1 μm) with low density. The EDS results confirm that the Au nanoparticles are Au^0 with trace amount of Cl^-. The Au nanoparticles are more stable against oxidation than the bulk Au under strong oxidizing conditions.

El-Deab *et al*. studied the morphology change of Au nanoparticles electrodeposited on various substrates including glassy carbon, HOPG, and Au(111) single-crystalline substrates.[58] The nature of the substrate and the electrolyte composition all influence the morphology of the electrodeposited Au nanoparticles. The electrocatalytic activity of the Au nanoparticles on different electrodes behaves entirely different for oxygen reduction reaction due to the different crystallographic orientation of the Au nanoparticles. The Au-decorated

electrodes rich in Au (111) facet show lower electrocatalytic activity than those with more Au (100) facet.

Bayati *et al*. prepared Pt nanoparticles on oxidized HOPG using double- and triple-pulse chronoamperometry methods to separate nucleation and crystal growth and control particle size and density.[61] The diameters of the synthesized Pt nanoparticles ranges from 1.4 to 52 nm in height by AFM measurements via changing applied potential sequence and duration time. Small Pt nanoparticles are easily oxidized according to XPS results, for example, the 5.5 nm Pt nanoparticles display an oxidized outer layer around the Pt core, and the 1.7 nm Pt nanoparticles are pure Pt oxide.

Dr. Penner's group also deposited Pt nanocrystals on HOPG electrodes using two-pulse method. The deposition process consists of instantaneous nucleation and diffusion-control growth mechanism. The Pt nanocrystals have average size of 1-10 nm with particle density of 10^9-10^{10} cm^{-2}. The selected area electron diffraction (SAED) results indicate that the Pt nanocrytals have FCC structure with (111) and (100) facets on the surface. The shape of the Pt nanocrystals vary from spherical nanoparticles to irregular shapes, such as triangles, squares, truncated triangles for large nanocrystals with size of 50 nm.

2.3.3.3 Electrocrystallization of organic crystals

Recent development of electrocrystallization of organic crystals includes but not limited to controlling the stoichiometry of the electrocrystallized compound, synthesizing coordination polymer and ternary salts, studying redox states and molecular conformation, and making crystalline thin films.[47] Well-studied

conducting organic materials include but not limited to charge transfer salts, metal-organic framework (MOF) and conducting polymers.

Organic charge transfer salts are interesting candidates for well-defined micro/nano-scale conductive structures to meet the needs of complex and miniature electronic devices. In 1971, Chiang et al. reported the first organic crystalline solid via electrolysis experiments.[62] Aromatic hydrocarbon such as perylene, pyrene, or azulene were electrochemical oxidized in tetrahydrofuran (THF) solutions with *n*-Bu_4NClO_4 as supporting electrolyte and formed black single crystals with structure of $(Ar)_2ClO_4$. These mixed valence salts were conductive.

Organic metal tetrathiafulvalene-7,7',8,8'-tetracyanoquinodimethane (TTF-TCNQ), first discovered in 1973, yielded from the chemical redox reaction between the electron donor, TTF and the electron acceptor, TCNQ.[63-64] The crystal structure of the needle-shaped crystals reveals that the unit cells are stacking along the crystallographic *b* axis. The electrical conductivity ranges from 200 to 700 ohm^{-1} cm^{-1} at room temperature.

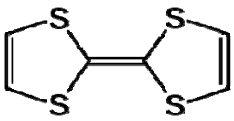

TTF

TCNQ

Later, new TTF-based charge-transfer salts were electrochemically synthesized with a variety of anions such as NO_3^-, Cl^-, Br^-, I^-, HCO_3^-, BF_4^-.[47, 65] The mixture of TTF and TTF radical cation can form self-assembled mix-valence charge transfer complexes (TTF)X*n* and exhibit high electrical conductivities (~

10^{-2} S/cm in semiconductor range) at room temperature. $(TTF)Br_x$ is one of the TTF based CT salts that is widely studied and still attracts scientific interest.

Hillier et al. incorporated *in situ* AFM to investigate the morphology of $(TTF)Br_{0.76}$ electrochemical nucleation on HOPG substrate.[66] By applying 0.40 - 0.70 V (vs. SCE) anodic potential step (1 - 5s), conductive needle crystals are obtained with well-defined widths (0.2 to 4 μm), lengths (10 to 15 μm), and heights (0.1 to 0.75 μm). Each face of the crystals has unique morphology and topography. The most prominent face is (010), which is parallel to the HOPG and along the needle axis. Additionally, triangular features are observed in the (011) face during the early stages of crystal growth and eventually evolve into oriented rectangular rafts with the long axis parallel to [100].

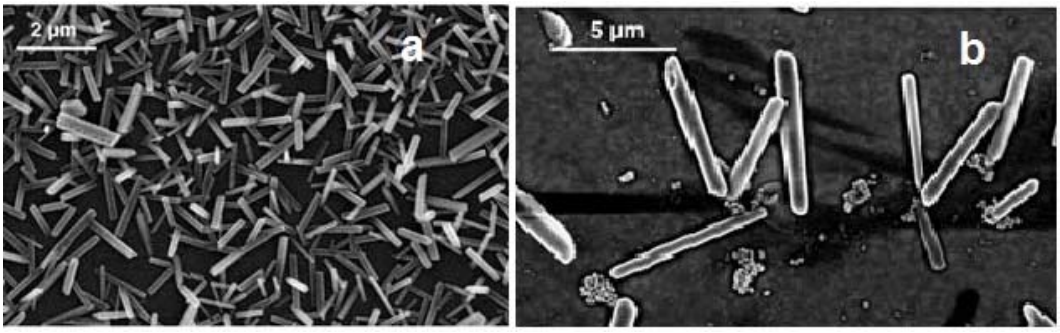

Figure 8. SEM images of $(TTF)Br_{0.76}$ crystals grown electrochemically on (a) prefabricated gold electrodes and (b) a silica substrate with gold nanoparticles acting as nucleation points. (Reprinted with permission from *Small*, 2005, 1, No. 8-9, 806 –808. Copyright © 2005 WILEY-VCH Verlag GmbH & Co. KGaA, Weinheim)

Mas-Torrent and Hadley conducted the electrochemical growth of $(TTF)Br_x$ mirocrystals on gold electrodes and on gold nanoparticles deposited on

a silicon wafer substrate.[67] $(TTF)Br_{0.76}$ microcrystals grow on Au electrodes with length of 1 - 2 μm and width of ~200 nm by applying 0.2 s of 20 pulses of 0.4 - 0.6 V vs. Pt (see Figure 8a). $(TTF)Br_x$ crystal rods also grow from Au nanoparticles by applying 0.2 s of 4V (vs. Pt) pulses on SiO_2 substrate (see Figure 8b). The insulating SiO_2 substrate allows an ion current to pass through, and the Au nanoparticles serve as nucleation seeds to initiate electrochemical growth of $(TTF)Br_{0.76}$ rods.

Favier *et al*. synthesized $(TTF)Br_{0.76}$ crystal micro-rods from Pt nanoparticles which are deposited on HOPG by applying 1 and 15 pulses of 0.2 s at + 650 mV (vs. Pt) as displayed in Figure 9a.[59] The widths of the crystal rods (30 - 600 nm) are linearly related to the diameter of the Pt nanoparticles (70 nm to 1.3 μm) on which they grow with an average ratio of 0.423 (see Figure 9b). Small individual $(TTF)Br_{0.76}$ crystallites were also observed on the graphite surface.

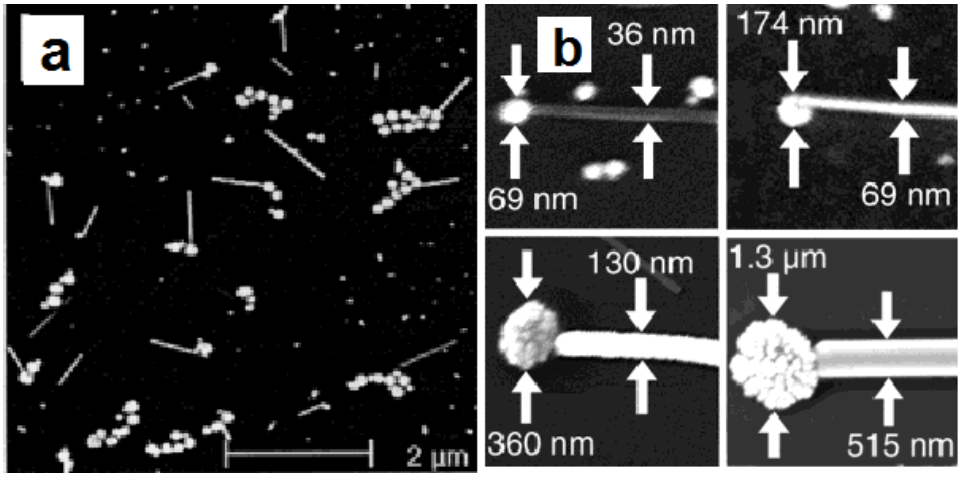

Figure 9. (a) SEM image of the electrocrystallization of $(TTF)Br_{0.76}$ rods on Pt nanoparticles on HOPG surface and (b) high magnification SEM images comparing the Pt nanoparticle diameter and the $(TTF)Br_{0.76}$ rod width. (Reprinted

with permission from *Adv. Mater.* 2001, 13, No. 20,1567-1570. Copyrights © 2001 WILEY-VCH Verlag GmbH, Weinheim, Fed. Rep. of Germany)

Bis(ethylenedithio)tetrahiafulvalene (ET), one of the TTF derivatives, is another widely studied molecular conductor. The π-π interaction in ET conductors is extended two-dimensionally: one is the π-π stacking direction, and the other is the lateral direction of the molecular plane, due to the periphery S atoms. Numerous conductive and superconductive ET salts are developed such as $(ET)_2I_3$,[68] $(ET)_2ReO_4$[69] and $[ET]_3[C_6(COO)_6H_4^{2-}]_2[C_5H_5NH^+]2{\bullet}CH_3OH{\bullet}2H_2O$ thin films[70].

Another group of conductive organic crystals is Krogmann's salt, a mixed-valence complex of platinum and tetra-cyanide bonded through linear Pt metal chains. For instance, the partially oxidized potassium tetracyanoplatinate $K_2[Pt(CN)_4]X_{0.3}{\cdot}(H_2O)_n$ (X = Cl, Br) can be synthesized by applying a small voltage containing $K_2[Pt(CN)_4]{\cdot}3H_2O$ with supporting electrolytes. The bronze-colored needle crystals will grow at the anode with metallic luster and metallic conductivity.[71] Its metallic conductivity is due to the overlap of the Pt $5dz^2$ orbitals and the linearly stacked Pt metal chains.

Other conductive candidates such as phthalocyanines and thiophenes will be taken into consideration if TTF, ET and Krogmann salts fail to nucleate on the nanoparticles.

2.3.3.4 Conductivity measurement of individual nanowire/tube

The organic charge transfer salts, Krogmann's salts, and conducting polymers which readily form into one-dimensional nanowires or nanotubes are

promising materials for electronic devices such as chemical and bio-sensors, field-effect transistors and capacitors.[72] Understanding the electron transfer properties and characterizing the electrical conductivity of individual nanowire/tube is crucial for improving the potential applications of conducting nanowires/tubes. Many strategies have been reported to estimate or measure the conductivity of individual nanowire/tubes.

The simple and conventional way is to estimate the conductivity from bulk resistance of nanowires. For polymer nanofibers synthesized from porous membrance templates, the nanofibers are left inside the pores and the bulk resistance of each pore is measured across the membrane by a two-probe method.[73-75] The conductivity of individual nanofiber is estimated based on the number and diameter of the fibers and neglecting the membrane resistance. However, this estimation method for individual nanofiber conductivity is inaccurate due to the uncertainties of the number of the nanofibers, and the poor contact between the membrane and the probes.

Recent development in conductivity measurements focuses on directly measuring the electric conductivity or *I*-*V* curves of individual nanowire/tube by incorporating an tip from AFM and scanning probe microscopy (STM), e-beam lithography and focused-ion beam (FIB) assisted deposition techniques. The direct measurements are designed to eliminate errors during calculation and estimation as well as reduce the contact resistance between the electrode probes and the nanowires/tubes.

AFM/STM tip assisted conductivity measurement is achieved by pressing the nanowire/tube with a conductive tip on a metal surface and measuring the *I-V* curve between the metal and tip.[76-78] This tip assisted method enables the electrical conductivity measurement in direction which is perpendicular or parallel to the axis of the nanowire/tube. The contact resistance cannot be eliminated but can be significantly reduced by increasing the contact force between tip and the fiber/tube. Penner's group modified this tip assisted method to measure the conductivity of molybdenum (Mo) nanowires by using gold-coated glass probe (dia. 200 nm) as one contact and silver paste as the other contact electrode.[79] The resistance of the nanowire is proportional to the length of the wire between the probe tip and the silver paste. The resistance of the nanowire with diameter of 450 nm is much larger than that of 380 nm in diameter.

One common approach is to prefabricate micro- or nano-electrodes via e-beam lithography, disperse nanowires/fibers onto the patterned surface and search single nanowire/fiber which is connected with multiple electrodes.[80-82] The drawbacks for this method are the large contact resistance between the electrode and the wire/fiber and the possibility of multiple wires/fibers lying on the same electrodes. Demoustier-Champagne and his coworker also studied the electrical properties of the hybrid metal-polymer nanowires using photolithography and e-beam lithography.[83-84]

Focused-ion beam (FIB) assisted deposition technique has been developed to minimize the contact resistance for measuring single nanowire/tube based on e-beam lithography method.[85-88] This technique is capable of directly

attaching metal microleads on single nanowire/tube to promise an ohmic contact. However, the metal deposition process may modify or damage the nanowires/tubes due to the gallium ions and only a few pA beam currents are allowed. Duvail *et al*. used this FIB deposition technique to investigate the effect of nanowire diameter on the electrical properties of single poly(3,4-ethylenedioxythiophene) (PEDOT) nanowires.[87] The conductivity of the nanowires increases significantly as the nanowire diameter reduces.

Another method to solve the contact problem is to electrochemically grown single nanowire/tubes between two prefabricated electrodes to avoid additional lithography process.[89-90] However, this method only applies to two-probe measurement and is not suitable for four-point probe measurement. Mas-Torrent *et al*. synthesized $(TTF)Br_{0.76}$ nanorod electrochemically using prefabricated gold electrodes with 5 μm gap as shown in the top insert SEM image in Figure 10.[67] The resistance of the $(TTF)Br_{0.76}$ nanorod is calculated to be 20 MΩ from the I-V curve in Figure 10. No clear gate-effect is observed of the source-drain current vs. gate voltage at source-drain voltage of 0.5V from the bottom insert plot in Figure 10.

In conclusion, organic/inorganic hybrid nanostructures have potential applications in electronic devices, sensors and catalysis. Novel properties and geometries of the hybrid nanostructures are expected under the nanoconfinement effect. Based on seed mediated nucleation (*SMN*) theory, particle/rod hybrids can be obtained through inorganic nanoparticle mediated organic crystal growth. Conductive organic crystal nucleation prefers

electrochemical method because of its precise control of supersaturation compared with conventional solvent evaporation. The electrical conductivity of the conducting nanorods is an important parameter for their properties and applications. Although some work has been done to synthesis hybrid structure and study nanoconfinement, more research is needed to fabricate the particle/rod hybrid materials and characterize their properties in order to better understand *SMN* and molecular ordering under nanoconfinement.

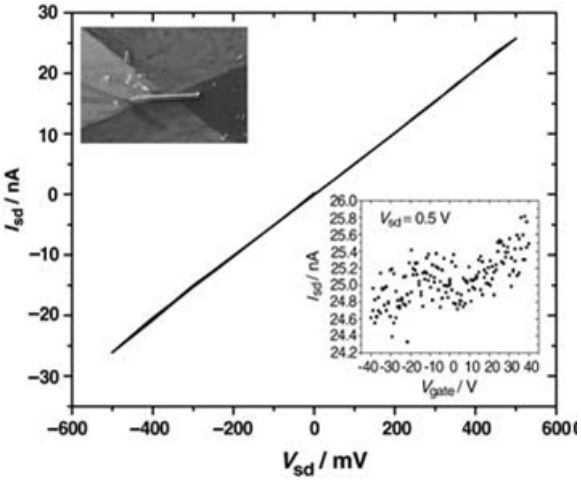

Figure 10. I-V curve for a (TTF)Br_x nanorod grown between two prefabricated triangular gold electrode with 5 m gap. Top insert image is SEM image of the nanorod and the gold electrode. Bottom insert plot is the source-drain current vs. gate voltage at 0.5 V. (Reprinted with permission from *Small*, 2005, 1, No. 8-9, 806 –808. Copyright © 2005 WILEY-VCH Verlag GmbH & Co. KGaA, Weinheim)

CHAPTER 3

EXPERIMENTAL METHODS

3.1 Materials

Carboxylic acids, including dodecanoic acid ($C_{12}A$, Aldrich, 98%), tetradecanoic acid ($C_{14}A$, Sigma, 99–100%), hexadecanoic acid ($C_{16}A$, Aldrich, 99%), octadecanoic acid ($C_{18}A$, Fluka, ≥ 99.5%), eicosanoic acid ($C_{20}A$, Sigma, ≥ 99%), docosanoic acid ($C_{22}A$, Aldrich, 99%), tetracosanoic acid ($C_{24}A$, Fluka, ≥ 99.0%), hexacosanoic acid ($C_{26}A$, Sigma, ≥ 95%), and triacontanoic acid ($C_{30}A$, Sigma, ≥ 95%) are used without any further purification. Trioctylphosphine oxide (TOPO, Sigma-Aldrich, 90%), selenium powder (Sigma-Aldrich, 99.5%), 11-mercaptoundecanoic acid (MUA, Sigma-Aldrich, 95%), tetranitromethane (Sigma-Aldrich), tetramethylammonium hydroxide pentahydrate (TMAH, Acros organics, 99%), cadmium oxide (CdO, Strem Chemicals, 99.9%) and trioctylphosphine (TOP, Strem Chemicals, 97%), 1-tetradecylphosphonic acid (Alfa-Aesar, 98%), Oleylamine (Aldrich), gold (III) chloride trihydrate ($HAuCl_4 \cdot 3H_2O$, >99.9%, Aldrich), potassium chloride (KCl, ACS grade, Fisher Scientific), tetrathiafulvalene (TTF, 97%, Aldrich), tetrabutylammonium bromide (TBAB, ≥ 99%, Fluka), potassium tetracyanoplatinate ($K_2Pt(CN)_4$, ACS grade, Sigma-Aldrich), and potassium ferricyanide ($K_3Fe(CN)_6$, ACS grade, Fisher Scientific) have been used as received. Solvents used include methanol (Mallinckrodt Chemicals, 100%), ethanol (Pharmco, 100%), 1-propanol (Fisher Scientific, 100%), 2-propanol (Mallinckrodt Chemicals, 100%), chloroform (Fisher Scientific, 100%), acetonitrile (CH_3CN, 99.9%, Fisher Scientific), toluene (Fisher

Scientific) and ethyl acetate (Fisher Scientific). HOPG (Mikromasch, ZYB grade) is hand-cleaved just before use with an adhesive tape until a smooth surface is obtained.

3.2 Nanoparticle Synthesis

CdSe and CdS nanoparticles are synthesized using the method described in Peng *et al* paper.[91] The thiolate capping procedure follows a modified procedure by Aldana *et al.*[92] The thiol-capped gold nanoparticles are synthesized using a sodium borohydride aqueous solution for the reduction of tetrachloroauric acid followed by reaction with the thiol.[93] The following nanoparticles are studied: CdSe capped by 3-mercaptopropionic acid (MPA-CdSe), CdSe capped by 11-mercaptoundecanoic acid (MUA-CdSe), CdSe capped by 1-dodecanethiol (DDT-CdSe), CdS capped by MUA (MUA-CdS), and Au capped by MUA (MUA-Au).

OA-GNPs with diameter less than 20 nm are synthesized according to the literature.[94] In one typical reaction, 49 mg (0.15 mmol) of $HAuCl_4$ is quickly added to a boiling solution of 10 ml (22 mmol) of oleylamine in 50 ml of toluene. After 15–30 min, the color of the solution changes gradually from bright yellow to grey yellow and finally deep red. After 2 h heating with reflux, the reaction mixture is allowed to cool to room temperature and 100 mL of methanol is added to precipitate the product. The OA-GNPs are obtained by centrifugation, wash three times with methanol, and vacuum dry of the precipitant. The product dissolves readily in non-polar solvents such as chloroform.

GNPs are also synthesized electrochemically using PAP 263A potentiostat (Princeton Applied Research) coupled to a Signatone Microscope

Probe Station. A three-electrode cell (as shown in Figure 11) is used with HOPG or GNP-decorated HOPG as the working electrode (WE), Pt wire (Diameter = 0.25mm) as the counter electrode (CE), and Ag wire (Diameter =0.25mm) as the quasi-reference electrode (QRE). All the potentials reported in this paper are converted into the values in reference to the SCE. The electrolytic solution consists of 0.01−10 mM $HAuCl_4$ with 0.1 M KCl as the supporting electrolyte. All solutions have been deoxygenated by purging with N_2 for 10 min prior to use. Single-pulse method uses the applied overpotential varying from -0.9 V to -0.1 V and the electrodeposition time ranging from 0.01 to 10 s. The double-pulse deposition is applied by modifying the electrodeposition procedure of Penner's two pulse method.[52-53] The first pulse is a short nucleation pulse for 10 ms at 0.1V (high overpotential of -0.5 V). The second pulse is a long dissolving pulse at 1 V for 5s. The Electrodeposition is performed on freshly cleaved HOPG at room temperature. After electrodeposition the HOPG substrate is rinsed with deionized water and dried under N_2.

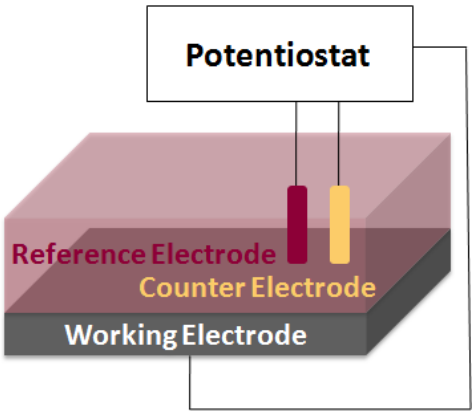

Figure 11. Scheme of three-electrode electrochemical cell.

3.3 Thin Film Fabrication

3.3.1 Spin coating

0.1 mL of freshly made solution of the carboxylic acid with a concentration range of 0.05−0.4 mM is used in each spin coating experiment. In each case, the carboxylic acid concentration was adjusted depending on its solubility and solvent evaporation rate by trial and error in order to achieve near monolayer coverage. The spin rate is 3000 rpm and the spin time is 60 s. To study the effect of the nanoparticle, mixed solutions containing both the carboxylic acid and the nanoparticle are used. The nanoparticle concentration in the mixed solution is maintained at 0.1 mM while the carboxylic acid concentration is maintained at 0.05–0.4 mM. The nanostructure of the films is unchanged when kept in the laboratory environment for at least 1 month.

3.3.2 Electrocrystallization

Electrocrystallization of $(TTF)Br_{0.76}$ has been conducted in 1−10 mM TTF and 0.1 M TBAB in CH_3CN following the literature.[66] A 4 s potential pulse of 0.5 V is applied on either bare HOPG or GNP-decorated HOPG at room temperature. The HOPG substrate is rinsed with ethanol and dried under N_2 after electrocrystallization. The morphology of the $(TTF)Br_{0.76}$ crystal is unchanged for at least 1 month when stored at room temperature.

The Krogmann's salt, $K_{1.75}Pt(CN)_4 \cdot 1.5H_2O$ (KCP), is electrocrystallized from 0.03 - 0.3 M $K_2Pt(CN)_4 \cdot 3H_2O$ in aqueous solution at 1.5 V for 0.1 s – 10 min on either freshly cleaved HOPG or GNP-decorated HOPG at room temperature following literature conditions.[95] The HOPG substrate is then rinsed with ethanol

and dried under N_2. The morphology of the KCP crystal is unchanged for at least 1 month when stored at room temperature.

3.4 Atomic Force Microscope (AFM)

Atomic force microscope (AFM) is a powerful tool for characterizing or engineering material surfaces and interfaces and provides a lateral resolution of 2 to 10 nm and a vertical resolution of 0.1 nm. AFM has several advantages over the electron microscopes: 1) AFM provides 3D topographic surface profile and does not require operation under a vacuum; 2) The specimen usually needs no special treatment such as gold/carbon coating; 3) AFM can be operated in ambient air or liquid environment using a fluid cell. The disadvantages of AFM is the constraint image size with a maximum of 10 – 20 μm and 150 × 150 μm in vertical and lateral dimension, respectively, and the image artifacts due to the wrong tip, parameter setting, or the sample itself.

AFM probes the surface of a sample with a sharp tip located at the free end of a cantilever. A micro-fabricated pyramidal silicon or silicon nitride tip with a radius of curvature on the order of nanometer is attached to a flexible cantilever of a specific spring constant. Forces between the tip and the sample surface cause the cantilever to bend, or deflect according to Hooke's law. Forces that are measured in AFM include van der Waals forces, capillary forces, chemical bonding, electrostatic forces, magnetic forces, etc. A photodiode detects the deflection of the cantilever through a laser beam focused on and reflected from the rear of the cantilever. The electrical differential signal of the photodiode is sent to a computer and generates a feedback signal for a piezo scanner to

maintain a constant force on the tip and also allows the computer to generate a map of the surface topography.

AFM can be operated in three modes: contact mode, non-contact mode and tapping mode. Contact mode AFM operates by sliding the probe tip across the sample surface while monitoring the change in cantilever deflection with a split photodiode detector. Non-contact mode measures the topography by sensing van der Waals attraction between surface and probe tip. Non-contact mode has lower resolution and is less stable than either contact or tapping mode. Tapping mode AFM, which is also the most commonly used mode, operates by lightly tapping the surface with an oscillation probe tip across the sample surface. The cantilever is oscillated at or slightly below its resonance frequency with amplitude ranging from 20 nm to 100 nm. The tip vibrates at 50 - 400 kHz in air and 10 kHz in liquid at constant amplitude.

Electrochemical atomic force microscopy (EC-AFM) is an attractive technique used to monitor and control the electrochemical processes, as the scanning electron microscope is limited to the examination of the surface after reduction-oxidation reaction (Redox). AFM enables the *in situ* observation of the early-stage crystal growth at nano scale and in liquid environment and is suitable for detailed study of crystal growth pattern and mechanism. The electrochemical control is accomplished by integrating a potentiostat with the AFM electrochemical cell which usually consists of a conductive substrate (such as graphite) as the working electrode, platinum (Pt) wire as the counter electrode and silver (Ag) wire as the quasi reference electrode.[66, 96-98] Potentiostat can

apply different voltammetric scans, such as step chronoamperometry, cyclic voltammetry. Liquid AFM in contact or tapping mode can measure real-time topographic images. In order to achieve precise control of the interfacial undersaturation for insulating surfaces, Macpherson et al.[99] initially present a novel integrated electrochemical/AFM technique using a Pt-coated, electrochemically-active AFM tip as the working electrode to measure the surface of potassium bromide single crystals in acetonitrile solution while simultaneously applying linear sweep voltammetry

In this dissertation, AFM is the most important characterization technique. The size and shape of the hybrid nanostructure are characterized by Dimension 3100 AFM (VEECO) operating in tapping mode in air. The height, amplitude, and phase images are obtained using silicon tapping tips (nanoScience Instruments, VistaProbes T300) with resonance frequency of 300 kHz and a nominal tip radius less than 10 nm. The scan rate is 1–3 Hz. Integral and proportional gains are approximately 0.4 and 0.8, respectively. Height images are plane-fit in the fast scan direction with no additional filtering operation.

3.5 SEM, FESEM, TEM, and EDAX

Scanning Electron Microscope (SEM) images sample surfaces by scanning with a high-energy beam of electrons and producing high-resolution images (1 - 10 nm). The typical electron energy used for SEM is 1 - 50 kV. The electrons interact with the atoms in the sample and produce signals that contain information about the sample's surface topography, composition and so on. The conventional SEM specimens must be electrically conductive to prevent the

accumulation of electrostatic charge at the surface. For nonconductive specimens, an ultrathin coating of electrically conductive material (commonly gold or carbon) needs to be deposited on the sample by low vacuum sputter coating or high vacuum evaporation.

Field Emission Scanning Electron Microscopy (FESEM) uses field-emission cathode in the electron gun which provides narrower probing beams at low electron energy (0.5 - 30 kV) to minimize sample charging and damage. FESEM is capable of scanning sample surfaces with clearer, less electrostatically distorted images with high resolution down to 1 nm. Another advantage of FESEM is simpler sample preparation without conducting coating on semiconductive and insulating materials.

Transmission Electron Microscope (TEM) is the original form of the electron microscope. The high voltage electron beam (60 keV to 3 MeV, typically 100 - 400 keV) is transmitted through an ultra thin specimen and interacts with the specimen as it passes through. TEM has a resolution of 0.2 – 0.3 nm and the high resolution TEM (HR-TEM) improves the resolution to less than 0.1 nm. TEM is suitable for characterizing nanomaterials, especially the inorganic nanocrystals, and provides size and shape information and even the crystalline planes inside the lattice crystal. The bright field imaging mode is most commonly used to observe the mass-thickness contrast of specimen. Thicker regions with a higher atomic number will scatter more X-rays and appear dark, while the regions with no sample in the beam path will appear bright.

Energy Dispersive X-ray Spectroscopy (EDS) is an analytical technique used for the elemental mapping or chemical composition analysis. A high-energy beam of electrons, protons, or X-rays is used to stimulate the emission of the characteristic X-rays from the inner shell of a specimen leaving an electron hole. An electron from an outer shell will fill this vacancy and release some energy in the form of X-ray. A semiconducting detector (SiLi) at low temperature measures the X-ray photon energy as the electron beam scans across the sample. The number and energy of the X-ray give the energy difference between the two shells and provide the chemical composition of the sample.

In this work, the nanostructures of the GNPs and semiconductive nanocrystals on the HOPG electrode are characterized by FESEM (JEOL JSM 7600F SEM) which is operated at an acceleration voltage of 15 kV, working distance of 8 mm, and probe current of 6 μA. The elemental compositions of the nanomaterials are obtained by *in situ* energy-dispersive spectroscopy (EDS) attached to the field-emission SEM at 15 kV in the secondary electron mode. TEM analysis is conducted by a JOEL FasTEM 2010 HR TEM in the bright field mode at an accelerating voltage of 200ekV to measure the size and shape of inorganic nanoparticle cores. The synthesized nanoparticles are deposited on the carbon-coated copper grid. The chemical composition of thiol-capped inorganic nanoparticles is measured by EDS attached to the Hitachi S-2400 SEM or JOEL FasTEM 2010 HR TEM. The estimation of thiol/nanoparticle and the area per thiol molecule on nanoparticle are based on EDS results.

3.6 X-ray Diffraction and Materials Studio Simulations

X-ray scattering techniques include a variety of non-destructive analytical techniques such as X-ray diffraction techniques, elastic scattering and inelastic scattering techniques. These techniques investigate the crystallographic structure, chemical composition, and physical properties of materials and thin films by observing the scattered intensity of an X-ray beam when it hits the materials. Elastic scattering techniques, including small angle X-ray scattering (SAXS), wide angle X-ray scattering (WAXS), and X-ray reflectivity, enable the study of nanostructures, monolayer or multilayer thin films and materials without long range order.

Materials Studio is designed for materials modeling and simulation. The software can model crystal structure and crystallization processes for the study of polymer properties, catalysis, and the study of structure-activity relationships.

In this dissertation, the crystalline structure of the GNPs are characterized by a Rigaku SmartLab X-ray diffractometer, using Cu $K\alpha_1$ radiation (λ=1.54056 Å) with a Ni filter working at 40 kV and 44 mA. General medium resolution parallel beam (PB) package is applied with a scan speed of 4 degree/min. Jade 8 software is used for data analysis. The single-crystal structure data of KCP crystal is collected by Rigaku Rotating Anode (Ru-2000) X-ray diffractometer using high intensity X-rays with a wavelength of 1.54 Å (Cu-anode) at a line focus. The maximum power is 8 kW (40 kV and 200 mA). Materials Studio software package (Accelrys) is used to view the crystal structures in 3D, generate template surfaces, dock guest crystalline lattices to template surfaces, and

simulate morphological transitions. The crystallographic data is available upon request at http://www.ccdc.cam.ac.uk/cgi-bin/catreq.cgi.

3.7 Conductivity Measurement

The electric conductivity is an important parameter for semiconducting materials and semiconductor devices for signal amplification, switching and energy conversion. In a semiconductor, the band gap between the conduction band and the valence band is small enough for the electrons to promote into conduction band. The conductivity of a semiconductor can be controlled by changing temperature, adding impurities and applying electrical fields or lights. The common methods for measuring conductivity are two-point probe and four-point probe methods. The four-point probe method separates the current and voltage electrode and therefore eliminates the contact resistances between the materials and the probes. The four-point probe method is also used for measuring the sheet resistance of thin films.

In this dissertation, the conductivity of the organic semiconductors (TTF and KCP crystals) are measured by KETHLEY 4200-SCS semiconductor characterization system using two-point probe method on a pre-fabricated Au electrode pattern.

CHAPTER 4

FORMATION OF CARBOXYLIC ACID NANORODS ON INORGANICNANOPARTICLES

4.1 Introduction

Physisorbed monolayers of amphiphiles are relevant to biological processes, lubrication, colloidal stabilization, detergency, patterning, and thin film devices.[100-101] Nanoparticle and/or nanowires arrays are employed in surface plasmon devices, surface-enhanced Raman scattering, single-electron devices, ion-sensitive field-effect transistors, and photocurrent generation modules.[1, 102-103] A key challenge for maximizing functionality of devices lies in establishing methods for connecting these disparate nano-components: nanoparticles, nanowires, and monolayers, in predefined spatial arrangements with distinct interfaces.[104-110] Self-assembly, such as the self-aligning tendency of nanorods (due to capillary forces[111] and entropy-driven minimization of the excluded volume[112]), can be used to connect and align nano-objects. However, self-assembly strategies for nano-component integration, that is, interfacing individual nanoparticles and nanorods are few. Furthermore, most studies are focused on inorganic nanocrystal self-assemblies, but molecular self-assembly based on organic nanocrystals[113-114] or hybrid inorganic/organic nanostructures is also expected to yield unique (and perhaps improved) properties. For example, junctions between self-assembled monolayers and metal nanoparticles allow the study of single electron transfer processes;[115] room-temperature light-emitting diodes have been created by the incorporation of a dye molecule within a

perovskite framework;[116] and attachment of oligonucleotides to Au nanoparticles triggers the self-assembly of DNA/nanoparticle arrays for biosensing and DNA sequencing.[117] Similarly, a single-wall carbon nanotube (CNT) placed between two Au electrodes and coated with enzymes shows higher detection sensitivity of enzymatic activity.[13] Hybrid Au nanoparticle CNT catalysts show an enhanced electrochemical catalytic activity for the oxygen reduction reaction.[25] Finally, the incorporation of high conductivity Au nanoparticles with the charge transport function of oligoaniline crosslinkers is shown to enhance the photocurrent generation of CdS nanoparticle arrays.[118]

This chapter reports a method to self-assemble organic nanorods of *n*-carboxylic acids directly on monolayer-protected inorganic nanoparticles.[119-120] Alkanes and alkane derivatives such as *n*-carboxylic acids physisorb on highly oriented pyrolytic graphite (HOPG) with their carbon chain skeletal plane parallel to the HOPG basal plane.[121-125] The nanoparticles are capable of disrupting this persistent physisorbed pattern of *n*-carboxylic acids on HOPG. In our previous work, nanorods of eicosanoic acid (arachidic acid, $C_{20}A$) have been shown to nucleate on mercaptoundecanoic acid-capped CdSe nanoparticles (MUA-CdSe) on HOPG.[126] In the absence of MUA-CdSe, $C_{20}A$ forms an epitaxial pattern in the form of parallel nano-stripes on HOPG with a periodicity of 5.6 nm - twice the $C_{20}A$ chain length. MUA-CdSe nanoparticles do not adsorb readily on HOPG; however, the nanoparticle/nanorod hybrid architecture forms spontaneously on HOPG from a mixed MUA-CdSe/$C_{20}A$ alcoholic solution during spin coating. The $C_{20}A$ nanorods possess uniform height (= 1.0 nm) and width (= 5.4 nm) despite

the stochastic crystallization kinetics.[43, 127] In this chapter, the formation mechanism of the nanoparticle/nanorod structure is investigated by varying film-forming conditions, carboxylic acid chain length, nanoparticle size, and nanoparticle chemical composition, including the inorganic core and protecting monolayer. The study contributes to the understanding of seed-mediated nucleation and crystallization, molecular ordering under nanoconfinement, and engineering of hybrid thin film materials.

4.2 Experiment

See Chapter 3 for nanoparticle synthesis, thin film fabrication via spin coating and characterization techniques.

4.3 Results

4.3.1 Nanoparticle characterization

Inorganic nanoparticles studied in this chapter involve CdSe, CdS, or Au surface modified with thiolates based on mercaptoundecanoic acid (MUA), mercaptopropionic acid (MPA), or dodecanethiol (DDT) as well as methyl-terminated oleylamide Au nanoparticles (OA-GNPs). The size and the chemical composition of the MUA-CdSe nanoparticles and OA-GNPs are given here separately in detail.

4.3.1.1 Characterization of thiolate-protected CdSe nanoparticles

TEM is used to determine the inorganic core size of the CdSe nanoparticles. TEM images of trioctylphosphine oxide (TOPO)-capped CdSe nanoparticles are displayed in Figure 12a, b. The average diameter of the CdSe nanoparticle core is determined to be 3.0 ± 0.6 nm. The nanoparticle size is also

measured by AFM sectional height analysis (Table 1). In order to immobilize negatively charged nanoparticles on mica, we use a method previously developed for DNA immobilization:[128] 20 μL of 10^{-6} M $MnCl_2$ solution is placed on 1 cm^2 freshly cleaved mica to render the substrate positively charged. The nanoparticle height values are used because the lateral values are convoluted by the AFM probe. The AFM height values differ from the TEM diameters by the capping layer thickness. A closely packed MPA monolayer presumably adds ~ 1 nm and an MUA monolayer adds ~ 3 nm to the overall particle diameter. The larger than expected size of MPA-CdSe is likely due to its tendency to aggregate.

The nanoparticle chemical compositions by EDAX are listed in Table 2. In the case of CdS nanoparticles, S content from the thiolate ligands is deduced from the difference of percentage of S in thiolate-capped and in TOPO-capped CdS nanoparticles. The results indicate that there is an excess of Cd in all the nanoparticles. Figure 12d is a schematic representation of CdSe with excess Cd near the surface (a similar structure for CdS is envisioned). We estimate a lower limit of thiolate capping layer coverage on the CdSe nanoparticles (for which TEM-derived core-sizes have been measured), thiolates/NP in Table 2, using the S to Cd ratio according to EDAX in the following equation (Eqn. 26):

$$\text{thiolate/NP} = \frac{p_S \times N_A}{\frac{p_{Cd} \times M}{\rho} \times \frac{1}{\frac{4}{3}\pi r^3}} \quad . \quad \text{(Equation 26)}$$

Here p_S and p_{Cd} are the atomic percentages of S and Cd according to EDAX, N_A is the Avogadro's number, M and ρ are the molecular weight and wurtzite crystal density of CdSe, and r is the TEM-determined CdSe nanoparticle

radius (1.5 nm). In comparison, a closely packed thiolate monolayer structure on planar surfaces gives an area per molecule of 21.4 Å^2.[129] MPA-CdSe is an outlier with the highest apparent surface coverage. This indicates that in this case the thiolate coverage is not monolayer coverage.

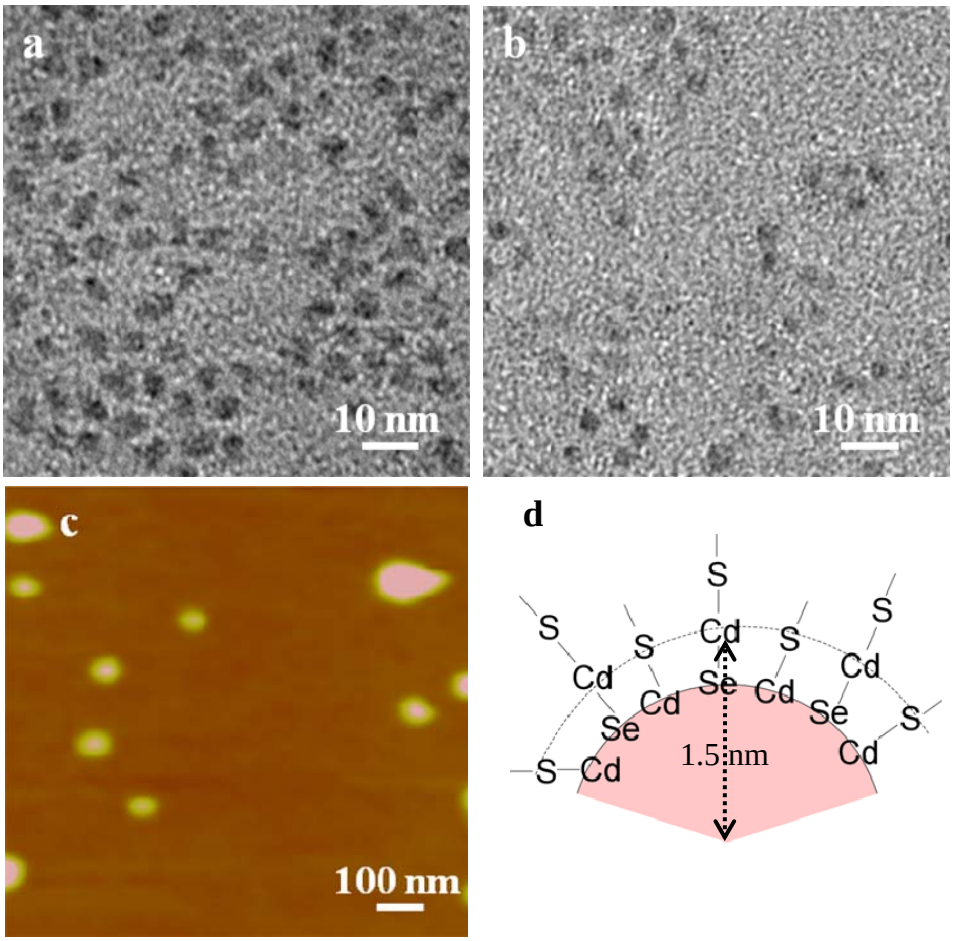

Figure 12. TEM images of (a) TOPO-CdSe nanoparticles and (b) MUA-CdSe nanoparticles. (c) AFM height image of MUA-CdSe nanoparticles deposited on Mn^{2+}-treated mica substrate (z range = 10 nm). (d) Schematic representation of a thiol-capped CdSe nanoparticle with Cd in excess.

Table 1. AFM sectional height analysis results of the nanoparticles.

Nanoparticle (synthesis ratio)	Vertical dimension (nm)	Lateral dimension (nm)
MUA-CdSe (3:1)	4.7 ± 1.9	16.9 ± 4.6
MUA-CdSe (5:1)	5.8 ± 2.1	40.2 ± 10.0
MPA-CdSe (5:1)	7.3 ± 2.3	30.8 ± 6.8
MUA-CdS (5:1)	3.1 ± 0.9	24.7 ± 8.6
DDT-CdSe (10:1)	3.6 ± 0.5	19.6 ± 5.0

Table 2. List of the chemical composition (atom %) and estimated thiolate surface coverage of the CdSe nanoparticles based on EDAX and TEM results.

Nanoparticle (synthesis ratio)	Cd (%)	Se or S from NP (%)	S from thiolate (%)	Thiolate/NP	Area/thiolate ($Å^2$)
MUA-CdSe (3:1)	49.23	38.36	12.41	71.6	39.4
MUA-CdSe (5:1)	48.11	36.07	15.82	94.7	29.8
MPA-CdSe (5:1)	41.58	28.50	29.92	213.6	13.2
MUA-CdS (5:1)	49.23	37.75	13.02	ND	ND
DDT-CdSe (10:1)	41.26	39.41	19.33	123.3	22.9

4.3.1.2 Characterization of OA-GNPs

The studies on methyl-terminated nanoparticles focus on OA-GNPs with characterizations using TEM, EDS, AFM, PXRD, FTIR, and TGA.

Figure 31(a) is a TEM image of the OA-GNPs dispersed on the TEM copper grid. The NIH ImageJ software was used to analyze the sphericity of the particles (N ~ 100) by measuring the area (*A*) and perimeter (*P*) of each particle. The average circularity of the OA-GNPs, *F* (*F = 1* for a perfect circle), was calculated to be $F = 4\pi A/P^2 = 0.98$. In the following discussion a spherical shape of the nanoparticle is assumed. Figure 13(b) shows a single nanoparticle with 2.3 Å fringes consistent with the interplanar spacing of face-centered cubic (FCC) Au

{111} planes. The arrow points to the reciprocal spacing in the 2D-FFT analysis (inset). Figure 13(c) shows the size histogram of the nanoparticles obtained from TEM images with a particle diameter range of 3–30 nm and an average diameter of 15.7 ± 5.6 nm. 80% of the particles are smaller than 20 nm. The atomic ratio of Au to N was determined to be ~ 0.25 from the EDS spectrum (Figure 13(d)). The Cu signal is from the TEM sample grid.

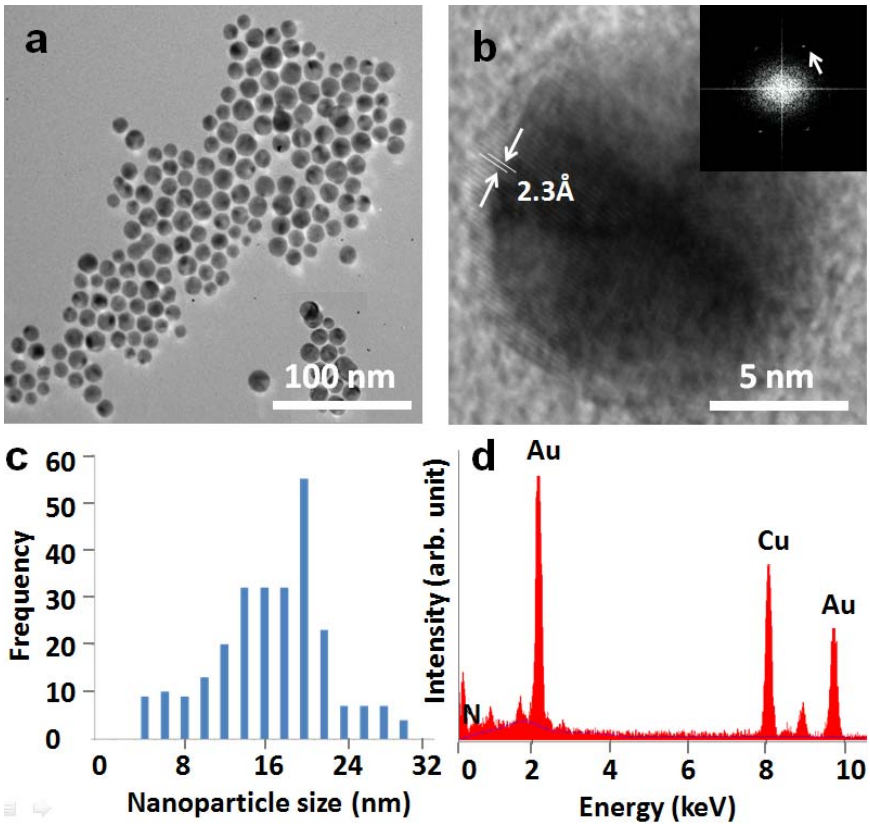

Figure 13. TEM images of OA-GNPs at (a) low magnification and (b) high magnification with a 2-D FFT image as the inset. (c) Histogram of OA-GNP diameters based on TEM. (d) EDS spectrum of OA-GNP chemical composition.

The size distribution of OA-GNPs was also measured using AFM. Figure 14(a) is a typical AFM image of OA-GNPs on HOPG. The AFM samples were prepared by spin coating of 0.1 mL 0.1 mM OA-GNPs chloroform solution on

HOPG. Chloroform quickly evaporates leaving a uniform particle layer on HOPG. The AFM images show well dispersed particles with no significant aggregation (a significant improvement over MUA-CdSe nanoparticles), an indication of a close-packed OA monolayer on GNPs. Figure 14(b) shows the particle diameter histogram measured in the z (height) direction using AFM height images. The particle size ranges from 2 to 20 nm with an average height of 8.2 ± 4.1 nm. The average OA-GNP size by AFM is less than that measured by TEM, especially considering that AFM values include the organic capping layer. It is possible that spin coating selectively deposits smaller particles.

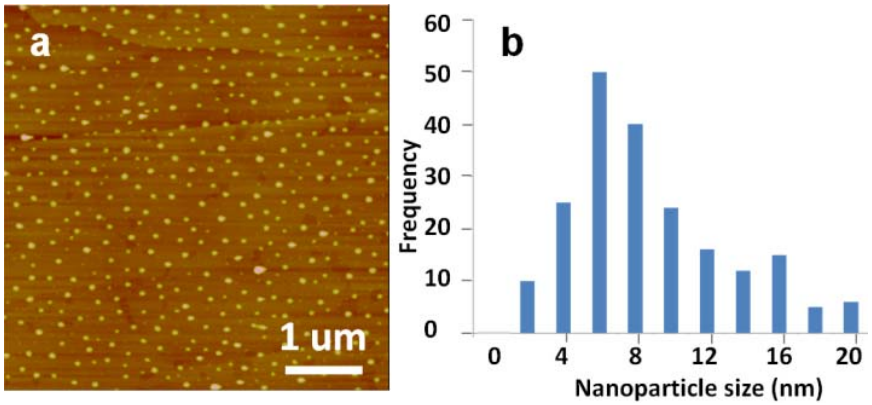

Figure 14. (a) AFM image (Z-range = 20 nm) of OA-GNPs on HOPG. (b) Size histogram of OA-GNPs measured by AFM sectional height analysis.

OA-GNPs were examined by PXRD as shown in Figure 15. The X-ray peaks at 2θ = 38.2°, 44.5°, 64.6°, and 77.5° correspond to {111}, {200}, {220}, and {311} crystalline planes with the interplanar d-spacing of 2.35 Å, 2.03 Å, 1.44 Å, and 1.23 Å, respectively. The intrinsic crystalline domain size, τ, is estimated using the Scherrer equation, $\tau = \frac{K\lambda}{\beta \cos\theta}$, where *K* is the shape factor equaling 0.9 for single crystal with a spherical shape, *λ* is Cu Kα wavelength, and *β* is the

full width at half maximum peak height. The estimated diameters of OA-GNPs using 4 individual peaks are 18.7, 12.5, 14.1 and 13.0 nm, respectively, and the average is 14.6 nm.

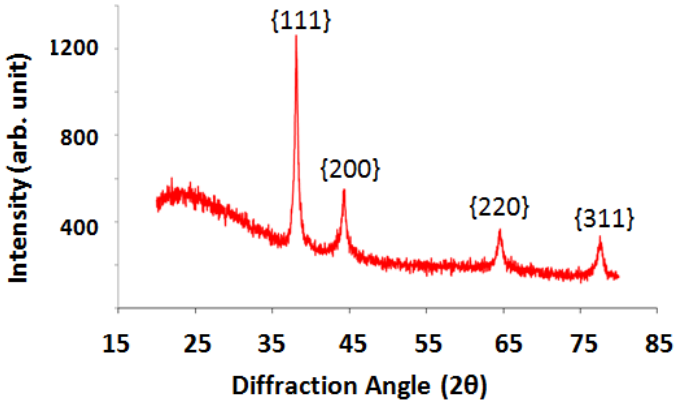

Figure 15. PXRD pattern of OA-GNPs.

Figure 16 shows the FTIR spectra of oleylamine (blue) and OA-GNPs (red). Both spectra display the characteristic C-H stretching vibration frequencies, ~ 2830 and 2900 cm^{-1}. After the reaction, the N-H bending peak at 1625 cm^{-1} disappears and new peaks associated with the amide bond, 1566 and 1653 cm^{-1}, appear. The results, consistent with those of others,[130] indicate that oxidation of oleylamine to oleylamide accompanies the reduction of Au(III) to Au(0). The hydrogen bond formation among the amide groups improves the monolayer chemical stability. The OA-GNPs dissolve readily in chloroform. We conclude that the OA-GNPs are terminated by the methyl group rendering them hydrophobic.

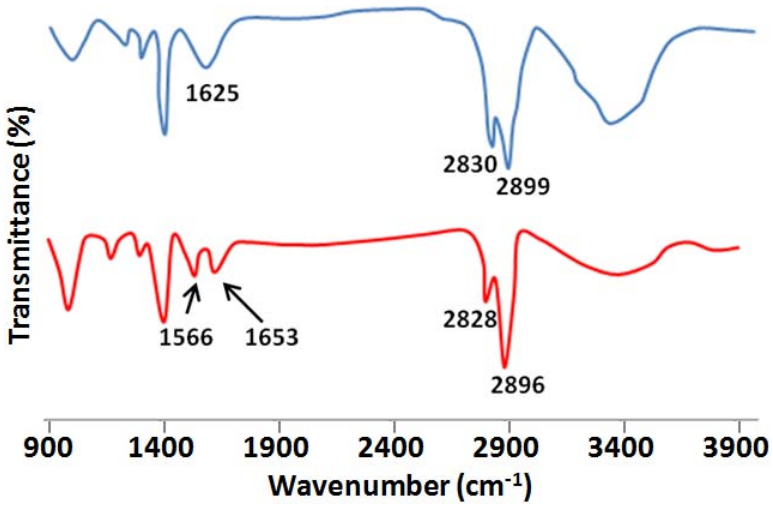

Figure 16. FTIR spectra of OA (blue) and OA-GNPs (red) powders.

In order to determine the surface coverage of OA monolayer on GNPs, TGA measurements were conducted as shown by Figure 17. The weight loss from 100°C to 375°C is attributed to the burn-off of the organic OA layer. The measured weight loss, 3.5% of the initial sample weight, corresponds to a molar ratio of Au to oleylamide of 39.5. In contrast, Au:N is 0.25 according to the EDS analysis. EDS overestimates the percentage of elemental N due to environmental impurities. The OA monolayer coverage on GNP surface in area per OA molecule is calculated to be 27.6 $Å^2$ using the average diameter of GNP (= 14.6 nm from PXRD), Au:OA molar ratio (= 39.5 from TGA), and density of Au (= 19.3 g/cm^3). For comparison, the limiting area per molecule for *n*-alkyl derivatives including carboxylic acids, amines, amides, and alcohols is 20–22 $Å^2$. The highest coverage of MUA on CdSe nanoparticles in our previous work yields an area per thiolate of 29.8 $Å^2$.[131]

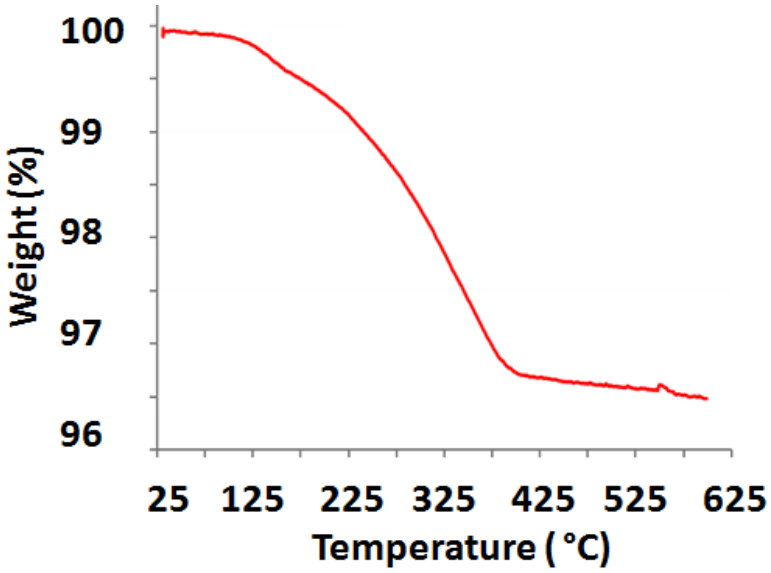

Figure 17. TGA graph of OA-GNPs.

4.3.2 Film structure of n-carboxylic acids on HOPG.

Representative AFM images of the nanopatterns formed by carboxylic acids with carbon numbers from 14 to 30, C_{14-30}A's, on HOPG are displayed in Figure 18. We are unable to obtain clear nanopatterns of carboxylic acids shorter than C_{14}A on HOPG by AFM in ambient environment. C_{14-30}A's are capable of self-assembling into the epitaxial nano-stripe pattern on HOPG at the monolayer coverage. The 2-D crystalline domains of nano-stripes display a rectangular shape whose size, a few hundred nanometers, is determined by the crystalline domain size of HOPG. The orientation of orthogonal stripe domains displays the three-fold symmetry of the HOPG lattice. The stripe thickness, 0.3 ± 0.1 nm, is consistent with the coplanar packing model in which the carbon skeleton plane of the carboxylic acid molecule lies parallel to the HOPG basal plane. All the nanopatterns formed, except that of C_{30}A, display a periodicity close to twice the molecular chain length (Table 3), as calculated by the following equation:

$$\text{Chain length} = \left(\frac{1}{2} \text{number of C atoms per chain} + \frac{1}{2} \text{number of O atoms per carboxyl group} \right) \times 0.246 \text{ nm}$$

(Equation 27)

The periodicity is consistent with carboxylic acid molecules lying in a head-to-head and tail-to-tail configuration (double-chain domain structure). $C_{30}A$ displays a predominant single-chain domain structure (periodicity = 3.9 nm) with inter-dispersed double-chain domains (periodicity = 8.0 nm) as shown by Figure 18h, i. Such coexisting domains have been observed on $C_{22}A$ on HOPG.[122] A unique film defect in the form of a row or network of holes is observed in the $C_{26}A$ film (Figure 19a–c), which we attribute to packing faults between double-chain and single-chain domains (Figure 19d). The packing fault forms if instead of aligning the tail to the previous molecular tail in the normal double-chain packing, the molecule points its tail to the opposite direction, which results in anti-parallel dimer arrangement in the single-chain domain. The hole-like defect occurs when molecular packing switches between double- and single-chain patterns. It is concluded that the carboxylic acids adopt a persistent epitaxial arrangement on HOPG, which has been reported by others,[121, 124, 132-134] by spin coating.

When switching the solvent from the ethanolic type to chloroform, the film nanostructures of $C_{16\text{-}30}A$'s on HOPG were found to be largely unchanged.

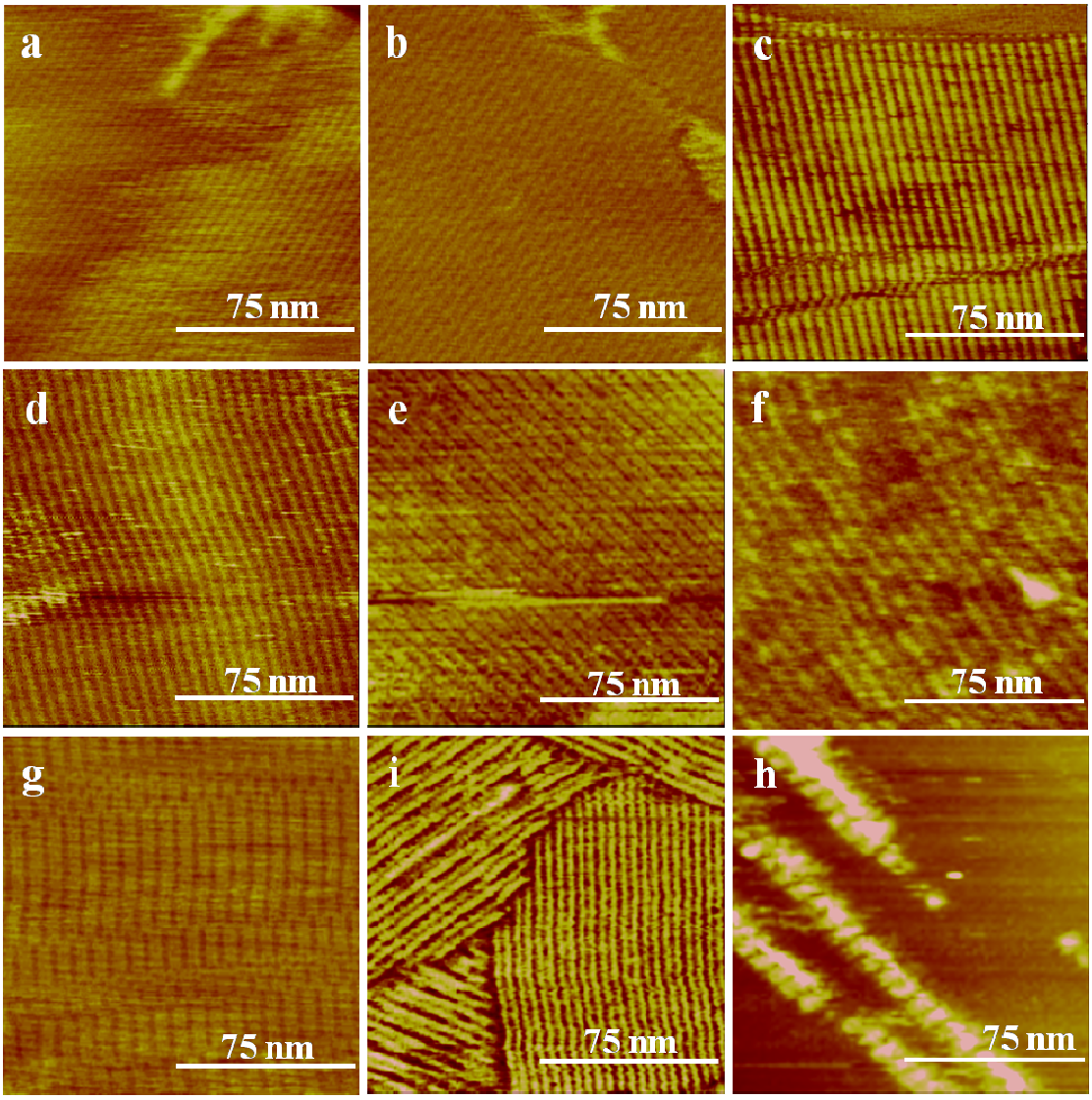

Figure 18. AFM images of *n*-carboxylic acid monolayers on HOPG. (a) $C_{14}A$. (b) $C_{16}A$. (c) $C_{18}A$. (d) $C_{20}A$. (e) $C_{22}A$. (f) $C_{24}A$. (g) $C_{26}A$. (h) $C_{30}A$ single-chain domain. (i) $C_{30}A$ double-chain domain (bright stripes) dispersed in the single-chain domain (smooth area). The z range is 2 nm for (a)–(g) and 10° for (h) and (i).

Table 3. List of periodicity of the stripe pattern by AFM and the corresponding all-trans molecular chain length of each carboxylic acid studied.

Carboxylic acid	Periodicity by AFM (nm)	2 × Molecular chain length (nm)	Domain structure
$C_{14}A$	4.0	3.936	Double-chain
$C_{16}A$	4.7	4.428	Double-chain
$C_{18}A$	5.0	4.920	Double-chain
$C_{20}A$	5.6	5.412	Double-chain
$C_{22}A$	6.1	5.904	Double-chain
$C_{24}A$	6.6	6.396	Double-chain
$C_{26}A$	7.0	6.888	Double-chain
$C_{30}A$	8.0/3.9	7.872	Double-chain/single-chain

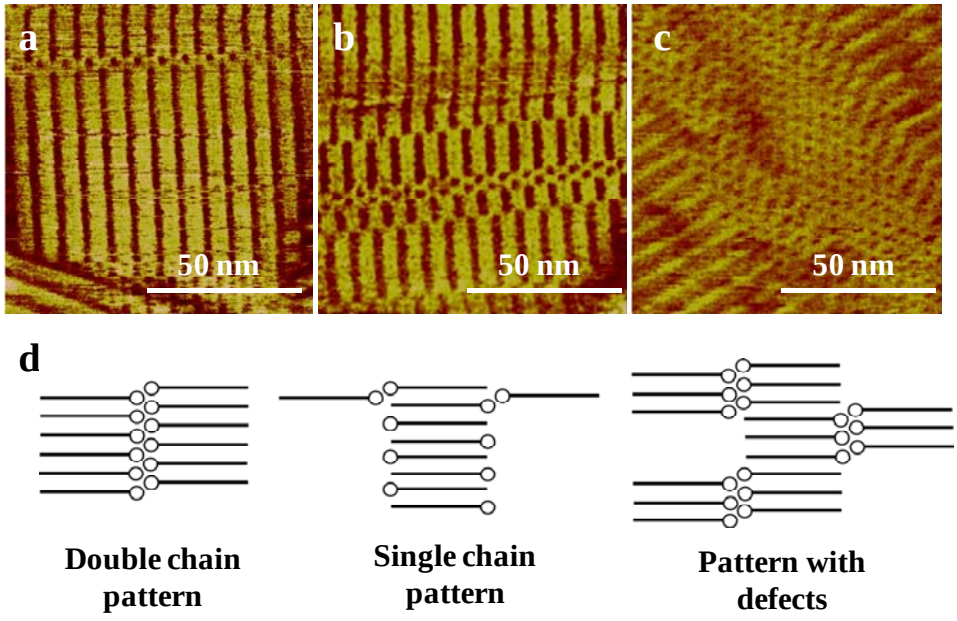

Figure 19. (a)–(c) AFM phase images of $C_{26}A$ films on HOPG with packing faults. Scan size = 100 nm. Z range = 5º. (d) Proposed scheme of the packing fault caused by coexisting double-chain and single-chain packing domains.

4.3.3 Film structure of *n*-carboxylic acids on HOPG in the presence of nanoparticles.

Nanoparticles are found to induce *n*-carboxylic acid nanorod formation. In this section, the factors that affect the carboxylic acid nanorod formation are investigated and studied.

4.3.3.1 Effect of carboxylic acid chain length on nanorod formation

Using similar film-forming conditions for the generation of MUA-CdSe nanoparticle/C_{20}A nanorod hybrid structure,[126] carboxylic acids of different chain length including C_{14}A, C_{16}A, C_{18}A, and C_{22}A can also form nanorods on MUA-CdSe nanoparticles. The results thus demonstrate that the hybrid structure is not limited to the MUA-CdSe/C_{20}A pair in the initial study. In addition, carboxylic acids with chain length longer than C_{22}A do not readily form nanorods on the nanoparticles. Figure 20 compiles AFM images of *n*-carboxylic acid films on HOPG in the presence of MUA-CdSe (5:1). Nanoparticle/nanorod objects can generally be found for the shorter *n*-carboxylic acid chains, but it becomes increasingly difficult to find the hybrid structures for the longer chains. A closer examination of Figure 20a shows that the C_{14}A rods contain doublets and triplets of nanorod in a row (marked by the arrows). The doublets and triplets are defined as two and three parallel nanorods in a close-packed structure, that is, the center-to-center separation distance equals the rod diameter. A close examination of Figure 20f, g determines that excess carboxylic acid molecules of C_{24}A and C_{26}A form the 2-D stripe domain instead of nanorods around the

nanoparticles. It can be concluded that the presence of the nanoparticles have minimal effect on the ordering of the two longer carboxylic acid molecules.

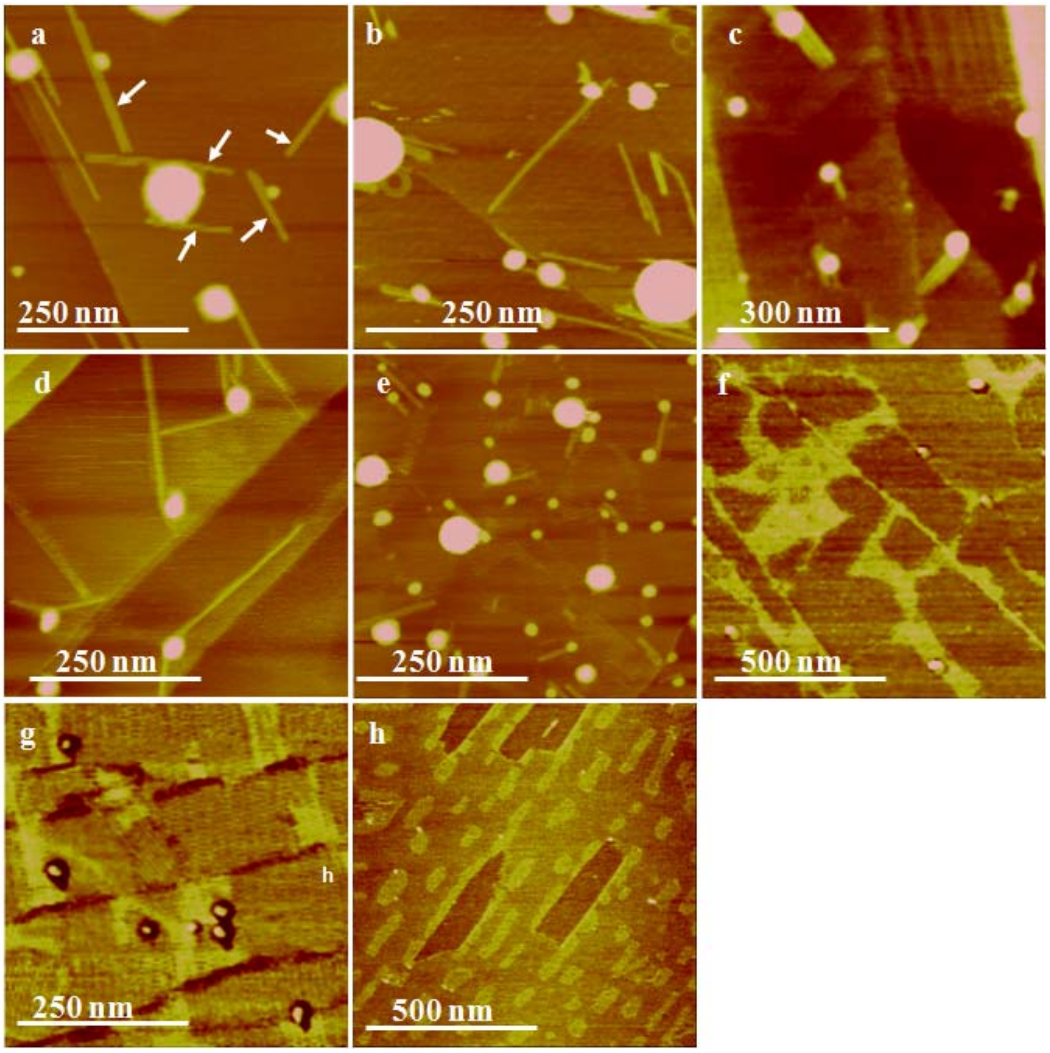

Figure 20. (a–g) AFM height images of film structure of *n*-carboxylic acids on HOPG in the presence of MUA-CdSe nanoparticles. (a) $C_{14}A$, (b) $C_{16}A$, (c) $C_{18}A$, (d) $C_{20}A$, (e) $C_{22}A$, (f) $C_{24}A$, (g) $C_{26}A$. The Z range is 8 nm for (a-e) and 10° for (f) and (g). (h) AFM height image of $C_{20}A$ film with excess partial layers in the absence of the nanoparticles (Z range = 3 nm). Arrows in (a) point to doublets or triplets of $C_{14}A$ nanorods.

The dimensional analysis results of the nanorods in Table 4 show that the individual nanorods have a fixed height, ~ 1 nm, a width proportional to the respective chain length, and a stochastic length distribution from 50 to 250 nm. The nanorods only form in the presence of nanoparticles. Figure 20h shows a situation when $C_{20}A$ coverage on HOPG is above the monolayer coverage, the excess $C_{20}A$ molecules form epitaxially oriented 2-D stripe domains in the absence of nanoparticles.

Table 4. List of the dimensions of carboxylic acid nanorods as determined by AFM sectional height analysis.

Carboxylic acid	Height of nanorods (Å)	Width of nanorods (Å)
$C_{14}A$	9.7 ± 1.2	43.8 ± 3.8
$C_{16}A$	9.7 ± 1.8	50.1 ± 3.4
$C_{18}A$	9.6 ± 0.8	52.6 ± 5.3
$C_{20}A$	9.5 ± 0.9	57.4 ± 3.3
$C_{22}A$	9.4 ± 1.1	62.5 ± 6.4

The competition between HOPG and the nanoparticle surface in directing the self-assembly of the carboxylic acids can be further modulated by solvents. Fast solvent removal is a prerequisite for the nanorod formation. If the solvent is allowed to slowly evaporate, the film becomes rougher.[135] Nanorods can be observed with a standing time up to 1 min prior to disk spinning. However, the nanorods have a tendency to display orientation along the HOPG lattice and they tend to form doublets and triplets instead of individual nanorods. With a 5 s standing time of a 2-propanol solution, before spinning, ~ 75% of the nanorods display a 120° mutual orientation angle. The rate of solvent removal can also be adjusted by the volatility of the solvent. High solvent volatility favors formation of

nanorods on the nanoparticle and the nucleated nanorods are oriented in an increasingly isotropic fashion. For example, using solvents of increasing volatility from ethanol, to 1-propanol, and to 2-propanol, the percentage of nanorods with three-fold symmetry increases approximately from 13%, to 27%, and to 65% (Figure 21). The orientation angle θ of the nanorod is measured by measuring the angle along each nanorod against the horizontal reference line using the angle command in Nanoscope. It is concluded that fast nucleation and crystallization kinetics favors the nanoparticle over the HOPG as a template for the ordering of *n*-carboxylic acids.

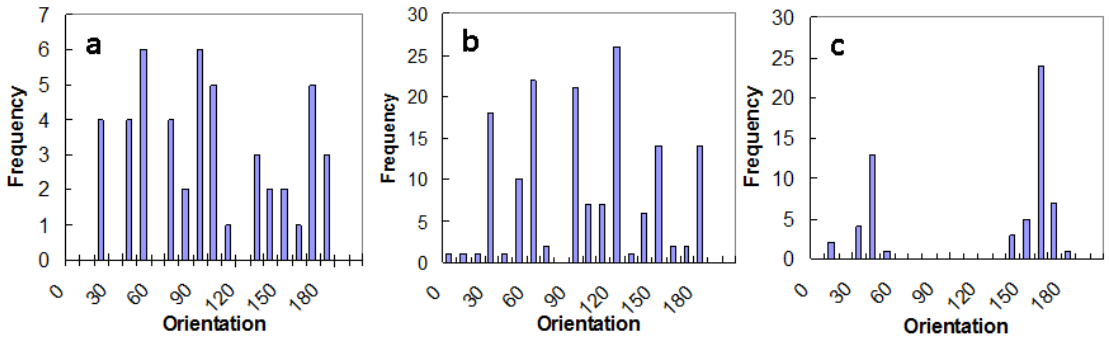

Figure 21. Orientation histogram of $C_{20}A$ nanorods attached to the MUA-CdSe nanoparticle in (a) ethanol, (b) 2-propanol, and (c) 1-propanol.

4.3.3.2 Effect of nanoparticle compositions on nanorod formation.

In order to determine the salient features of the nanoparticle governing nanorod formation, we investigated different core and shell compositions. We have determined that the chemical nature of the nanoparticle core is immaterial to nanorod formation. Thus, $C_{20}A$ nanorods form on both MUA-CdS and MUA-Au nanoparticles of similar size range and under similar film-forming conditions as MUA-CdSe nanoparticles (Figure 22a, b). On the other hand, when the capping layer, MUA, is replaced with other capping agents, film-forming conditions need

to be adjusted accordingly to facilitate nanorod formation. For example, under identical film-forming conditions, MPA-CdSe and DDT-CdSe are ineffective nucleation agents for the nanorods. Both types of nanoparticles have poor colloidal stability in ethanol and propanol. Indeed, MPA-CdSe has a strong tendency to aggregate in all the solvents studied and no conditions have been found that would enable nanorods to be induced by MPA-CdSe. The colloidal instability is attributed to the fact that the shorter chain of MPA may be less effective at preventing oxidation and subsequent aggregation.[136] DDT-CdSe nanoparticles, on the other hand, disperse well in non-polar solvents such as chloroform. Figure 22c shows the nanoparticle/nanorod hybrid structure formed by the DDT-CdSe/C_{20}A pair when chloroform is used as the solvent. We conclude that nanorods form when the thiolate capping layers permit good dispersion (indicated by the clarity and color intensity of the solution) of the nanoparticles in a chosen solvent. Fully dispersed nanoparticles make the nanoparticle surface available for heterogeneous nucleation. The DDT-CdSe case also refutes a previous hypothesis[126] that specific molecular interactions, for example, the H-bond between the carboxyl group of MUA and that of *n*-carboxylic acids, are responsible for nanorod formation since DDT-CdSe is terminated by methyl group.

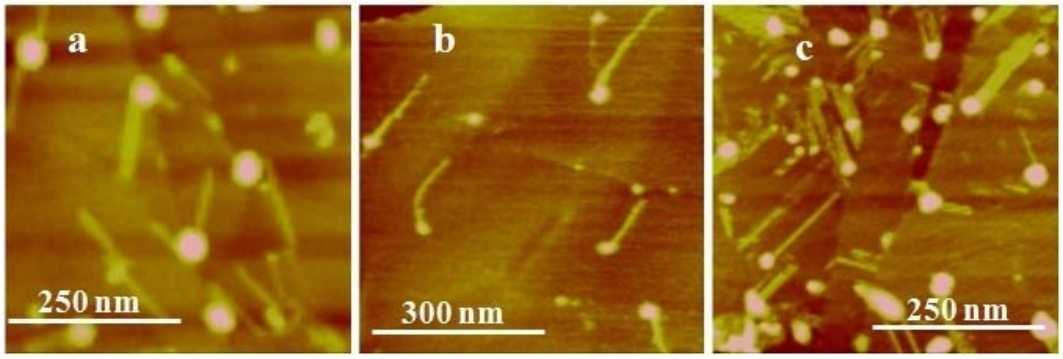

Figure 22. $C_{20}A$ nanorods attached to (a) MUA-CdS, (b) MUA-Au, and (c) DDT-CdSe. The z range is 8 nm.

In order to address the question whether the carboxylic nanorod formation requires a seed surface with the carboxyl group, a series of experiments were carried out using methyl-terminated OA-GNPs in chloroform. Figure 23 summarizes the results of $C_{16\text{-}30}A$'s film structure in the presence of OA-GNPs on HOPG. The dimensions of the nanorods by AFM height sectional analysis are reported in Table 5. The nanorod structure is identical to the one induced by MUA-CdSe nanoparticles, which displays the characteristic dimensions of the C-form carboxylic acid crystal structure exists in all these systems. No nanorods were obtained with carboxylic acids with fewer than 16 carbons. These shorter molecules form a 2-D layer around the nanoparticles. Carboxylic acids with more than 30 carbons were not studied. The individual nanorods display a fixed height, ~ 1 nm, a width close to twice the change length, and a stochastic length distribution in the range of 50–250 nm. The width of $C_{20\text{-}30}A$'s nanorods is ~ 2.6× the respective chain length, an apparent value due to tip convolution. The width of $C_{16}A$ nanorods is ~ 5× its chain length suggesting the formation of nanorod doublets.[131]

A qualitative difference between the nanorods induced by OA-GNPs and those produced by MUA-CdSe[131, 137] is that 1) fewer nanorods are produced by OA-GNPs and 2) a large percentage of the nanorods produced by OA-GNPs are detached from the seed (arrows pointing to this feature in Figure 23). The percentage of the detached nanorods of all nanorods formed was found to increase with increasing chain length. The percentage of detached nanorods is 22% for $C_{16}A$, 26% for $C_{20}A$, 55% for $C_{22}A$, and 74% for $C_{26}A$, respectively. There are not enough nanorods for meaningful statistical evaluation in the case of $C_{30}A$. One possible reason for the detached nanorods in the OA-GNP case may be the lower interfacial bonding energy between the nanorod and the methyl group at the surface of the OA-GNP as compared to that between the same nanorod and carboxyl-terminated MUA-CdSe nanoparticles. In the latter case, polar-polar and H-bond interactions are likely present to prevent nanorod detachment from the seed surface.

Table 5. AFM results of the periodicity of carboxylic acid stripe patterns and the height and width of carboxylic acid nanorods.

Carboxylic acid	Periodicity by AFM (nm)	Height of nanorods (nm)	Width of nanorods (nm)
$C_{16}A$	4.7	0.8 ± 0.2	10.9 ± 2.4
$C_{20}A$	5.6	0.8 ± 0.3	7.0 ± 1.7
$C_{22}A$	6.1	1.1 ± 0.4	7.8 ± 2.3
$C_{26}A$	7.0	1.0 ± 0.3	10.0 ± 2.1
$C_{30}A$	8.0	0.8 ± 0.2	11.4 ± 2.6

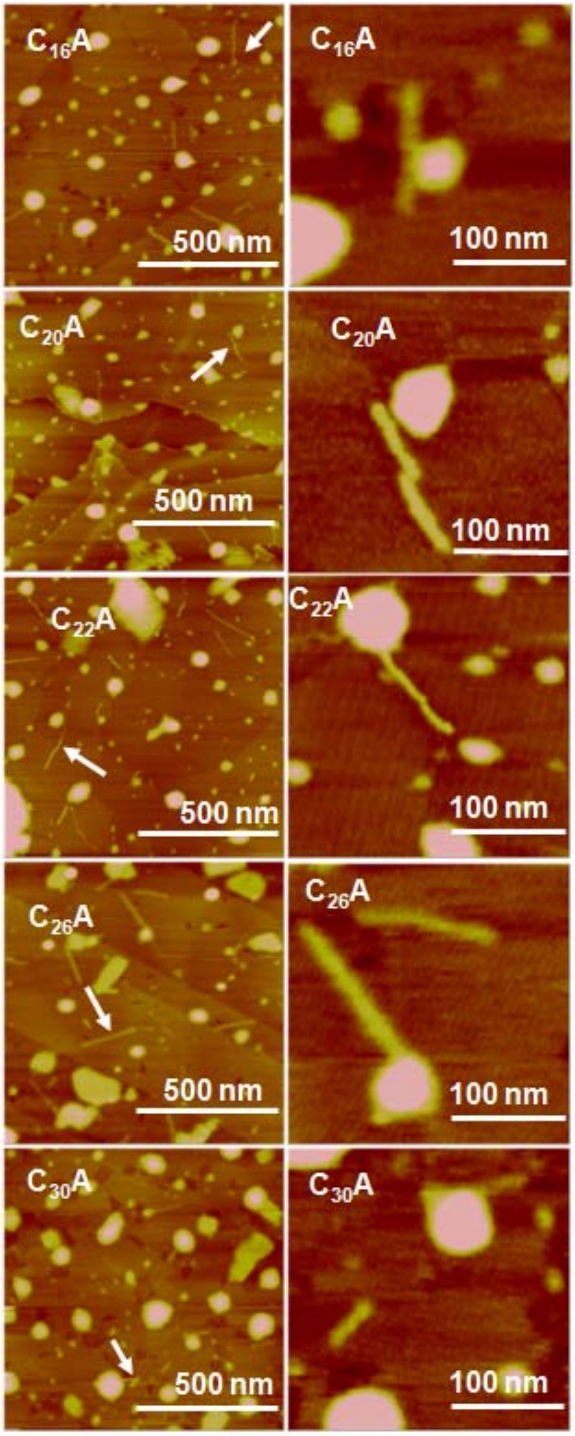

Figure 23. Low-magnification (left column, z-range = 10 nm) and high-magnification (right column, z-range = 5 nm) AFM height images of *n*-carboxylic acids on HOPG in the presence of OA-GNPs.

4.3.3.3 Effect of nanoparticle size on nanorod formation

The nanoparticle size is expected to be an important factor governing nanorod formation. Generally we find that the number of nanorods per nanoparticle increases with increasing particle size (as measured by AFM) with a cutoff particle size of ~ 15 nm. Figure 24 is a plot of the number of individual $C_{20}A$ nanorods per MUA-CdSe (5:1) nanoparticle as a function of d^2 where d is the nanoparticle height as measured by AFM height analysis. It shows a linear relationship between the number of nanorods per particle and the particle surface area (d^2). The data contain a standard deviation of 22%. Nanoparticles larger than 15 nm are ineffective nucleation seeds. While the majority of the nanorods are single rods for all nanoparticle sizes, there is an increasing occurrence of doublets, triplets, etc. (an upper limit of number of closely packed nanorods = 5) with increasing particle size. We also observe the likelihood of multiple nanorod formation to increase with increasing nanoparticle size to carboxylic acid chain length ratio, as the smallest chain, $C_{14}A$, has the highest tendency to form multiple closely packed rods (Figure 20a). Approximately 20% $C_{14}A$ nanorods are single rods and the rest are doublets, triplets, *etc.*

In the case of using OA-GNPs to induce carboxylic acid nanorods, the nanoparticle size effect is consistent with the MUA-CdSe case. There is a seed size range that favors nanorod formation and for OA-GNPs, the seed with height of 4−10 nm (Figure 25).

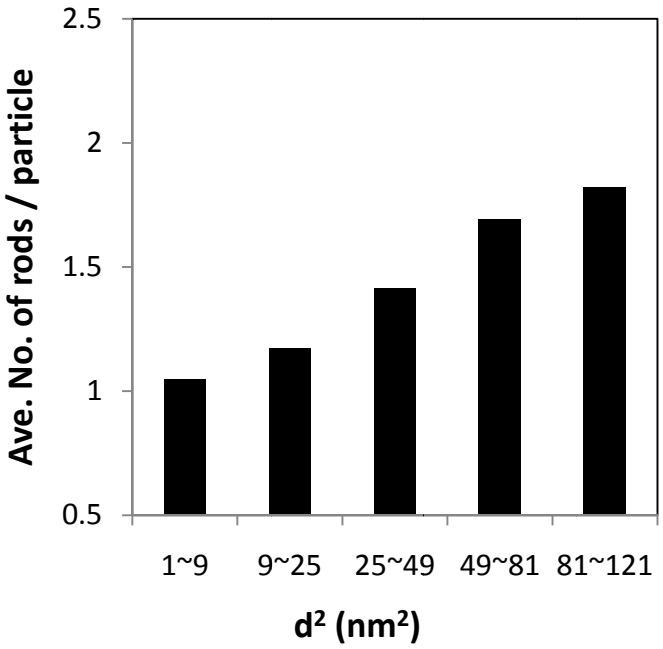

Figure 24. Histogram of the number of multiple nanorods per 2-D crystal as a function of the height of nanoparticle (in 2-propanol).

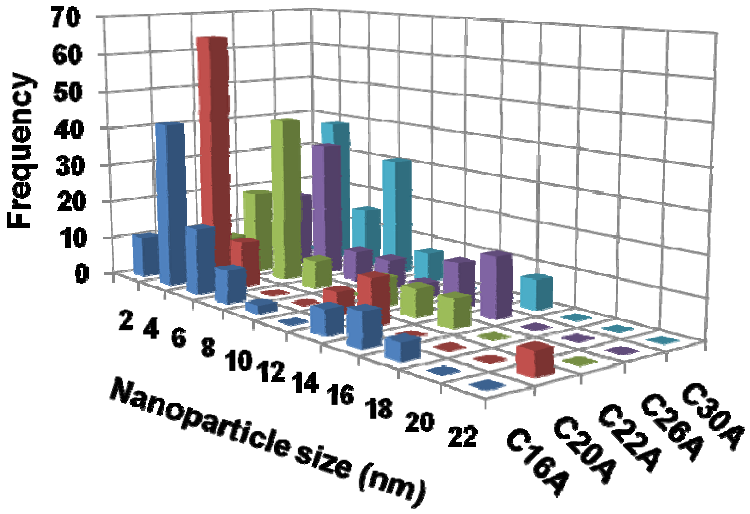

Figure 25. Histogram of the percentage (%) of nanorod induced by nanoparticles as a function of the height of the nanoparticles.

4.4 Discussion

4.4.1 n-Carboxylic acid packing structure in the nanorod vs. templated on HOPG.

Even-numbered long-chain *n*-carboxylic acids possess complex polymorphism, which include the triclinic A-, and monoclinic B-, C-, and E-forms.[43, 138-139] In all the forms the H-bonded dimers of the $R_2^2(8)$ symmetry pack into a bilayer pattern.[140] The main difference between the B- and C-form is that in the B-form the unit cell dimension along the *a*-axis is expanded due to a rotation along the *b*-axis while in the C-form the unit cell dimension along the *b*-axis is expanded due to a tilt over the *a*-axis.[141] While both B- and C-forms can be obtained by fast crystallization, kinetics[142] and the solvent ethanol both favor the C-form.[143] We therefore use the C-form crystal structure to interpret the AFM topographical measurement results. The C-form crystal structure of $C_{18}A$ ($P2_1/a$, $Z = 4$) has the following lattice parameters: $a = 0.9360$ nm, $b = 0.4950$ nm, $c = 5.0700$ nm, and $\beta = 128.250^{o}$.[127, 141, 144] The width of the $C_{18}A$ nanorods by AFM, 5.0 ± 0.6 nm, is consistent with the unit spacing between {001} planes. The height of the nanorods, 1.0 ± 0.1 nm, is slightly larger than the interplanar spacing of the {100} planes (0.74 nm) of the C-form $C_{18}A$ crystal structure. We hypothesize that the rods are formed by carboxylic acid unit cells attaching to each other along the *b* direction during crystallization. Figure 26 shows the crystalline packing structure of the molecular rod in relation to the nanoparticle and the solid surface. This is very different from the crystal habit of $C_{18}A$ formed from solution, which displays a thin prismatic plate shape with the most

prominent {001} face displaying an acute angle of 54° to the {110} faces. For the molecular nanorods obtained here, the interplanar distances of {001} and {110} are 5.07 and 0.41 nm, respectively. The length direction of the rod is defined by the largest face, the {001} face. The carboxylic acid nanorod possesses the unit cell dimensions (the smallest crystalline unit) in both width and height directions and it consists of a single bilayer row in the width direction with H-bonded carboxyl group in the center and terminal methyl groups at the sides. In comparison, in the stripe pattern templated by HOPG, the alkyl chain zigzag plane is parallel to the HOPG basal plane, which presents a smaller layer thickness of 0.3 nm. It is clear that the nanorods are nucleated from the nanoparticle and they show different packing structure than the stripe pattern templated by HOPG.

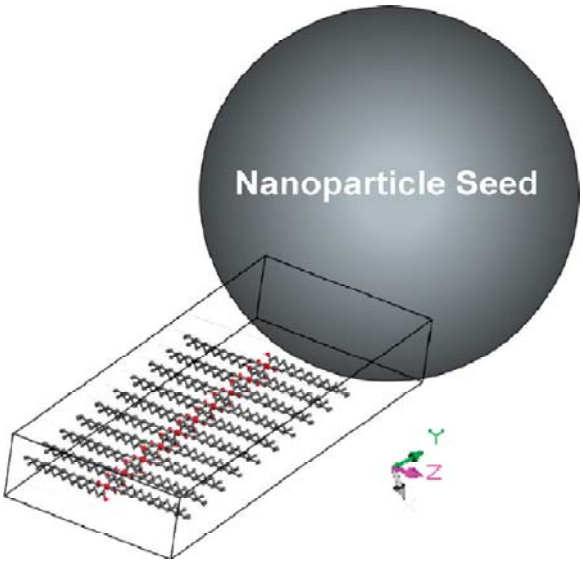

Figure 26. Hypothesized structure of a carboxylic acid molecular rod in the crystalline packing structure of the C-form attached to a nanoparticle nucleation seed.

4.4.2 Nanorod formation mechanism.

The spin coating process generates high supersaturation, $\Delta\mu$, which favors the formation of small crystals. In the case of a volatile fluid wetting the HOPG substrate, after an outward flow to produce a smooth film, the last stage of spin coating is dominated by solvent evaporation.[145-146] The film thickness is a function of spin speed, *s*, initial viscosity, ν_0, and evaporation rate, *e*, as shown in Equation 28:[145]

$$h \propto s^{-2/3} \nu_0^{1/3} e^{1/3}. \quad \text{(Equation 28)}$$

In our case, the high spin speed combined with low solution concentration result in ultrathin crystalline films reaching the monolayer limit. In addition, fast solvent evaporation results in high $\Delta\mu$, which leads to high nucleation rate, *J* (defined as the number of nuclei formed per particle per unit time per unit volume), and low crystal growth rate. This “burst” crystallization kinetic model is a common strategy in the synthesis of small and uniform inorganic nanoparticles. According to the classical nucleation theory[147-149] the critical nucleus size, r_c, decreases with increasing $\Delta\mu$, as shown in Equation 29:

$$r_c = \frac{2\Omega\gamma_{cf}}{\Delta\mu}. \quad \text{(Equation 29)}$$

In the above equation, Ω is the unit volume, and γ_{cf} is the surface free energy of the crystal-fluid interface. Our results suggest that r_c reaches the unit cell dimension (in height and width) of the nuclei at high $\Delta\mu$ (induced by high evaporation rate).

However, we suggest that spin coating alone does not produce the nanorod nanocrystals. In the absence of nanoparticles in solution, 2-D crystallites of *n*-carboxylic acids form on HOPG with an epitaxial orientation to the substrate. We surmise that nanoparticles play an essential role in nucleating the nanorod and possibly limiting the growth of the nanorod in the directions normal to the nanorod axis. Particle-mediated nucleation promotes heterogeneous nucleation and plays either a desirable role to control the nucleation process or an undesirable role as impurities. Despite the widespread use of crystallization seeds in material purification, the effect of seed size and composition on nucleation has yet to be understood, particularly when the seed size approaches the critical nucleus size. For example, the minimum seed size requirement for heterogeneous seed-mediated nucleation remains unknown.[44]

According to the classical nucleation theory,[147-149] the presence of a flat foreign surface lowers the nucleation energy barrier from ΔG_0^* to ΔG^* depending on the contact angle, θ, between the cap-shaped nucleus and the planar substrate surface:

$$\frac{\Delta G^*}{\Delta G_0^*} = f = \frac{1}{4}(1-\cos\theta)^2(2+\cos\theta). \text{ (Equation 30)}$$

Here, $\cos\theta = \left(\gamma_{sf} - \gamma_{sc}\right)\Big/\gamma_{cf}$, where γ_{sf}, γ_{sc}, and γ_{cf} are the substrate/fluid, substrate/crystal, and crystal/fluid interfacial tension, respectively. The nucleation capability of a substrate surface, which is defined by *f*, diminishes (*f* approaches the upper limit value of 1) if the substrate is a particle with a small radius of curvature, R^S. *f* is a function of θ and the normalized particle radius of

curvature $R' = R^S/r_c$,[30, 150-151] in which R^S is the radius of curvature of the seed particle. When the particle is large, *e.g.,* R' >10, the particle surface curvature approaches that of a flat surface, and the energy barrier is dominated by θ. When the particle is small, *e.g.,* R' < 0.1, f is close to 1, and the foreign particle is ineffective in nucleation. When 0.1 ≤ R' ≤ 10, f decreases drastically with decreasing r_c (or increasing $\Delta\mu$). Therefore small r_c or the presence of a good structural match compensates for the small seed size so that even nanoparticles can be effective nucleation substrates. In addition, small seed particles with high curvature dominate nucleation kinetics at high $\Delta\mu$.

Considering only the interfacial energy term, θ goes to zero when γ_{sf} is close to γ_{cf} . This will be the case when the chemical nature of the crystal is similar to that of the substrate. In heterogeneous nucleation, the presence of a foreign particle surface that is completely wetted by the nucleating fluid will reduce the nucleation energy barrier to zero. A good dispersion of the nanoparticle seeds in the crystallizing fluid allows a complete wetting of the seed surface by the fluid. This is governed by the chemical characteristics of the surface, which can be modulated by introducing capping ligands of suitable polarity.

Next we consider the elastic energy term. Our results show a possible competition between nanoparticle and HOPG substrates for the carboxylic acid crystal nucleation. At low $\Delta\mu$, J is dominated by the epitaxial match between the carbon chain plane and the basal plane of HOPG, which lowers the nucleation energy. In the competition between HOPG- and nanoparticle-mediated molecular

ordering, longer carbon chain length on the part of the *n*-carboxylic acid favors the epitaxial interaction with HOPG because the epitaxial interaction with HOPG increases with increasing chain length. Thus, the epitaxial mismatch between the HOPG lattice and carboxylic acid molecules in the randomly oriented nanorods nucleated from the nanoparticle becomes increasingly prohibitive for nanorods composed of longer chains.

The nanoparticle-induced nanorod formation is also consistent with the molecular simulation results of colloidal crystallization that identify a critical seed size.[44, 152] The simulations show that seed-mediated nucleation occurs only when the seed particle (substrate) radius is at least 5× the size of the colloidal particles (crystallizing species). Interestingly, snapshots of the nuclei of increasing size show that the initial colloidal cluster tends to wrap around the seed as a 2-D layer when the seed size is 7× that of the colloid. However, the cluster becomes a radially oriented "1-D" rod when the seed size is 5× that of the colloid. The authors hypothesize that the radially elongated cluster is induced by the high curvature of the small seed, which imposes an unsustainable strain for tangential growth. The length scale of our system may not be pertinent to the colloidal crystallization simulated, but our observation of the 1-D rods is consistent with the 1-D clusters in the simulations.

In comparison to the energetic considerations, nucleation kinetics may be more important for the nanorod formation. The nanorod structure with a poorer structural match than the 2-D stripe domains may represent a kinetically more favored state at high $\Delta\mu$. At high $\Delta\mu$, J is dominated by the pre-exponential

collision/attachment factor, *K*, and less by the exponential energy barrier term in the following expression:

$$J = K\exp\left(-\Delta G^{*}/kT\right). \qquad \text{(Equation 31)}$$

In particle-mediated nucleation, *J*, is proportional to the number and size of the nanoparticle seeds because nucleation occurs in the solution layer adjacent to the particle surface. We find that the nucleation rate per particle, J_p, as represented by the number of nanorods per particle on an AFM image, is indeed proportional to the nanoparticle surface area, $\left(R_i^S\right)^2$ or d^2 in Figure 24, where *d* is the nanoparticle height as measured by AFM height analysis.

A closer examination of the AFM images shows roughly two populations of nanorods. A majority of the nanorods are oriented along the radial direction of the particle while the rest adopt a tangential orientation. Their relative percentage, RP, is close to 1:

$$RP = \frac{\text{Number of tangential nanorods}}{\text{Number of radial nanorods}} = \frac{84}{77} = 1.09 \text{ . (Equation 32)}$$

The similar distribution of the two orientations is consistent with equal attachment probability of carboxyl dimers in the tangential and radial orientations to the particle seed surface. The similar size of the tangentially oriented nanorods and the radially oriented nanorods suggests that at least in this case the strain energy caused by misalignment of carboxylic acid nanorods on carboxylic acid monolayer-covered HOPG plays the more dominant role in limiting crystal growth width direction than the curvature constraint placed by the nanoparticle.

4.5 Conclusion

The work demonstrates a methodology of using monolayer-protected inorganic nanoparticles as nucleation seeds for the creation of extremely narrow organic nanorods. The hybrid nanoparticle/nanorod architecture deposited on HOPG is characterized by AFM. The carboxylic acid nanorods are 50 to 250 nm in length with cross-sections of dimensions similar to the *a* and *c* axes of the C-form crystals. It is deduced from the cross-sectional topographical analysis that a single H-bonded carboxyl dimer spans the width of the nanorod and they pack in a co-planar crystalline structure along the long axis of the nanorod. Nanoparticles of different core materials (CdSe, CdS, and Au) but with the same capping ligand (MUA) are capable of inducing identical carboxylic acid nanorods. We further determine that nanoparticles with methyl terminal groups are also capable of inducing the nanorod structure if a compatible solvent is used. Variation of the carboxylic acid chain length reveals a competitive crystallization templating process between the nanoparticle surface and the HOPG basal plane. The narrow width of the nanorod is attributed to two energetic factors. There is a significant mismatch between the carbon chain plane and HOPG for randomly oriented nuclei, which prevents the attachment of carboxyl dimers along the carbon chain direction (the *c* axis). The second factor is the high strain energy as a result of the highly curved surface of the nanoparticle in the tangential direction of the seed surface. A rough estimate of nucleation rate per nanoparticle shows that the kinetics of nanoparticle-mediated nanorod formation is consistent with the prediction from the classical nucleation theory. The nucleation rate is

proportional to the surface area of the seed substrate. This work shows that contrary to the common belief that particles of nanometer size have diminished effect in heterogeneous nucleation, they indeed are capable of nucleating and constraining the shape of molecular crystals. Imaging and probing the impact of size and shape of the critical clusters provides new insights into heterogeneous seed-mediated crystallization where few details are known. Moreover, it enables us to create and control the formation of unique hybrid nanostructures that employ the dual functionalities of the inorganic nanoparticle and organic nanorod.

CHAPTER 5

FORMATION OF $(TTF)Br_{0.76}$ NANORODS ON GNPs

5.1 Introduction

In thin film devices, such as single-electron transistors (SETs), electron transport can be regulated across multiple phase boundaries by connecting different nano-components, for example, nanoparticles with nanorods.[153] Ultrasensitive electrochemical sensors based on CV, ion-sensitive field-effect transistors, and enzymatic reactions have been constructed using GNP superstructures with improved sensor stability, sensitivity, and selectivity.[1, 154] Nanoparticle electrodes enhance electron transfer between redox agents and bulk electrodes and allow fine tuning of sensitivity via particle size, morphology, and number.[132] GNP electrodes show better selectivity when organic crosslinking units with π-donors complementary to analyte molecules are incorporated.[1, 155] Other examples of inorganic/organic hybrid devices include GNP-decorated π–conjugated oligo(p-phenylenevinylene) nano-tapes with enhanced electrical conductivity,[156] CdS/GNPs arrays crosslinked by oligo-anilines with enhanced photoconductivity,[118] and enzyme-coated CNTs placed between Au electrodes with higher enzymatic detection sensitivity.[13] As a final example, GNPs facilitate electron transport among redox reaction centers of TTF in TTF-derivatized GNP electrodes.[157] The transport properties of molecular conductors are intimately connected to their crystal structures. A better understanding of nucleation and crystallization of molecular crystals is necessary for crystalline materials of small molecules, such as TTF derivatives, to be used in nanodevices.

This chapter continuous the investigations on the confinement effect of nanoparticles on the nucleation and crystal growth of small organic molecules. The electrochemical deposition of gold nanoparticles (GNPs) on highly oriented pyrolytic graphite (HOPG) is investigated in which the GNP morphology is varied systematically by electrolytic conditions. The electrochemical synthesis of tetrathiafulvalene charge-transfer salt, (TTF)$Br_{0.76}$, nanorods using the GNPs as nucleation seeds is reported. Electrocrystallization is essential for the synthesis of molecular conductors of high purity and is desirable for establishing general applicability of molecular crystals.[47, 158] Electrocrystallization offers a more controlled environment than the previously used evaporative crystallization for observing nucleation at short length and time scales.[159] In electrocrystallization, the primary driving force is the applied overpotential, η, which can be precisely controlled. η is defined as the electrochemical potential difference between the applied potential and the standard redox couple potential. Seed-mediated crystallization can be further tuned by selecting seeds and nucleating materials with suitable electronic states of donors and acceptors.

Nanoparticle-decorated electrodes are useful for the understanding of charge transport phenomena including tunneling, single-electron charging, percolation effects, and scattering in granular materials.[160-163] Electrodeposition of Au on the HOPG obeys the Volmer-Weber 3-D island growth mechanism due to the weak van der Waals interaction.[164] Despite the weak interaction the electrodeposited GNPs display high stability when deposited on semiconductors. One reason is the irreversibility of the electrochemical reaction due to the large

bandgap energy between the states of the donor Au and the conduction band of the semiconductor.[165] This study will contribute to this area of research by correlated AFM and CV measurements in order to relate GNP size, shape, and surface coverage to the electrolytic conditions. AFM and CV have been used to characterize the GNP deposition on the HOPG.[60, 166-167] The standard oxidation potential for the redox couple Au/Au^{3+}, $E^0_{Au-Au^{3+}}$, is reported to be 0.76 V (*vs.* saturated calomel electrode (SCE)). The GNP electrodeposition on the HOPG has been described by nucleation and crystal growth steps. The presence of electrodeposited GNPs has been shown to enhance electrochemical reactivity of the bulk electrodes in the redox reactions of $Fe(CN)_6^{3-/4-}$ and $Ru(NH_3)_6^{3+}$, and hydroxymethyl-ferrocene (FcMeOH).[168]

TTF (π donor) and 7,7,8,8-tetracyanoquinodimethane (TCNQ, π acceptor) charge-transfer salt, TTF·TCNQ, is often considered the first synthesized organic metal.[63, 169] Organic metals display metallic electrical conductivity, $\sigma \sim 10–10^4\ \Omega^{-1}cm^{-1}$, which increases with decreasing temperature. The electrochemical synthesis and crystal structure of TTF-based materials have been well documented.[66, 170-172] The predominant needle crystal habit of TTF-based crystals suggests a high probability of nanorod formation on nanoparticles in maintaining an overall aspect ratio. The electrical conductivities of TTF-based crystals arise from the fact that electrons and holes are delocalized along segregated stacks of donor and acceptor free radicals in the crystal structure. Thus TTF-based metals are pseudo-1-D conductors with the highest conductivity along the stacking axis, which is also the long axis of the needle-shaped crystals.

TTF is oxidized at the anode surface in bromide electrolyte solution into mixed valence salt of needle habit, $(TTF)Br_{0.76}$, in the following reaction:[59, 66-67, 173] $TTF + 0.76Br^- = (TTF)Br_{0.76} + 0.76e^-$. The standard reduction potential for TTF/TTF^+, $E^0_{TTF-TTF^+}$, is 0.3 V (*vs.* SCE). This study investigates the effect of $HAuCl_4$ concentration, applied overpotential, and electrodeposition time on the morphology and electrochemical properties of the GNPs on the HOPG. The capability of the electrodeposited GNPs to act as nucleation seeds and to induce $(TTF)Br_{0.76}$ nanorod formation will be demonstrated.

5.2 Experiment

See Chapter 3 for nanoparticle electrodeposition, thin film fabrication via electrocrystallization and characterization techniques.

5.3 Results and Discussion

5.3.1 Electrodeposition of the GNPs on the HOPG electrodes.

0.05–10 mM $HAuCl_4$ aqueous solutions with 0.1 M KCl as supporting electrolyte are used for the GNP electrodeposition on the HOPG electrodes. The electrochemical reduction with a standard potential of $E^0_{Au(III)/Au(0)}$ = 0.761 V is:

$$AuCl_4^- + 3e^- \rightarrow Au(0) + 4Cl^- .$$ (Equation 33)

Considering the ion concentration that used in this paper (0.05–10 mM) the equilibrium reduction potential (E_{eq}) is 0.77 ± 0.02 V, calculated based on the Nernst Equation for reduction process from the following equation:

$$E_{eq} = E_{Au(III)/Au(0)} = E^0_{Au(III)/Au(0)} + \frac{0.059}{n}\log\frac{\left[AuCl_4^-\right]}{\left[Cl^-\right]^4} \text{ (at 25 °C)} .$$ (Equation 34)

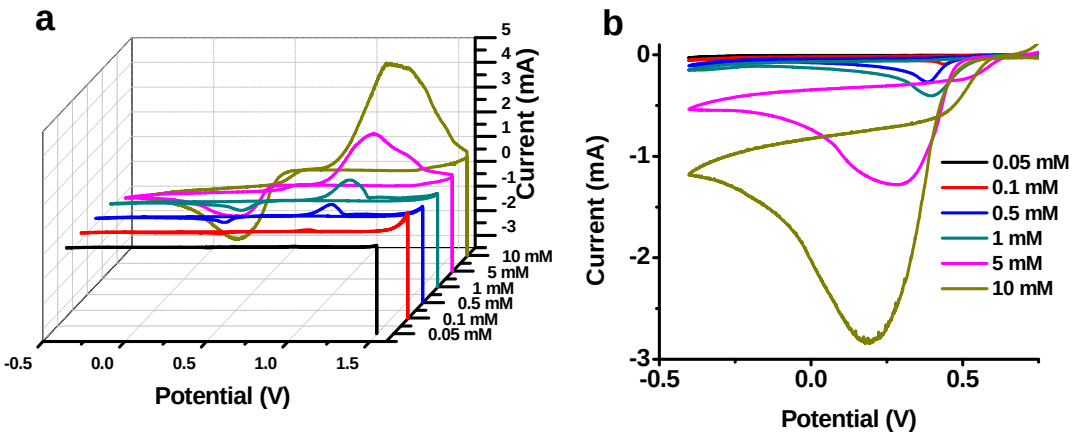

Figure 27. CV curves in 0.05–10 mM $HAuCl_4$ solutions on the HOPG electrode. (a) 3D plots of the full potential range. (b) Plots of the cathodic reduction region only.

CV measurements are used to determine the appropriate potential range for the GNP deposition. Figure 27 shows the typical CV curves on the HOPG in 0.05–10 mM $HAuCl_4$ aqueous solutions. The potential range is -0.5–1.5 V. The scan rate is fixed at 100 mV/s. All the CV curves display a cathodic peak at 0.2–0.5 V associated with the reduction of Au^{3+} to Au^0 and an anodic peak at 1.0–1.2 V associated with the oxidation of Au^0 to Au^{3+}.[60, 166-167] As the $HAuCl_4$ concentration increases, the absolute values of the cathodic/anodic peak currents increase, the cathodic peak potential shifts toward a more negative value, and the anodic peak potential shifts to a more positive one. The onset potential for $HAuCl_4$ reduction is 0.50–0.55 V for all the $HAuCl_4$ concentrations studied. The crossover potential of the forward and the backward scan (E_{co}) is 0.66 ± 0.02 V for the investigated concentration range, which is close to the calculated E_{eq}. The overpotential (η) required for Au nucleation on the HOPG is

defined by the difference between the applied potential, *E*, and the crossover potential, E_{co}: $\eta = E - E_{co}$.

The peak current, i_p, is determined by the Randles-Sevcik equation for simple redox reactions:

$$i_p = (2.69 \times 10^5) n^{\frac{3}{2}} A D^{\frac{1}{2}} C v^{\frac{1}{2}}. \quad \text{(Equation 35)}$$

where 2.69×10^5 is a constant at 25 °C, *n* is the number of electrons transferred in the redox event (*n* = 3 in this case), *A* is the electrode surface area (cm^2), *D* is the diffusion coefficient (cm^2/s), *C* is the concentration of the electroactive species in the bulk solution (mol/cm^3), and *u* is the scan rate (V/s). Figure 28a displays a linear relationship between the cathodic peak current, $i_{pc,}$ and the $HAuCl_4$ concentration at *u* = 100 mV/s. Figure 28b shows a linear relationship between i_{pc} and $u^{1/2}$ in the range of 50–500 mV/s in 0.5 mM $HAuCl_4$ solution. Both graphs indicate that the reduction of Au^{3+} to Au^0 is under the control of reactant diffusion to the electrode surface as opposed to either surface reaction or kinetic control.[46] *D* of the $AuCl_4^-$ ion in aqueous solution can be calculated from the slope of the graph in Figure 28b. The electrode surface area, *A*, is estimated by the droplet volume (=50 µL) and its contact angle on the HOPG substrate (= 50^o) to be 0.5 cm^2. *D* of $AuCl_4^-$ in 0.5 mM $HAuCl_4$/0.1 M KCl is calculated to be 5.6×10^{-6} cm^2/s. In comparison, the literature value of *D* of complex metal ions in aqueous solutions is around 10^{-5} cm^2/s.[174]

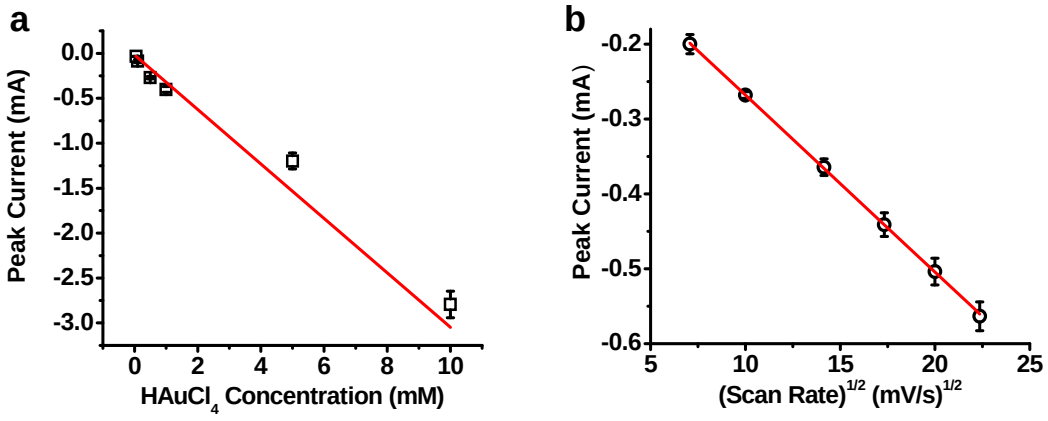

Figure 28. (a) The dependence of the reduction peak current (i_{pc}) on the $HAuCl_4$ concentration in the range of 0.05–10 mM at a scan rate of 100 mV/s. (b) The dependence of the reduction peak current (i_{pc}) on (scan rate)$^{1/2}$ in 0.5 mM $HAuCl_4$ solution.

AFM is used to study electrodeposited GNP morphology on the HOPG as a function of the $HAuCl_4$ concentration, applied overpotential, and deposition time. We define the GNP size as the average volume per particle (by bearing analysis), GNP density as the average number of particles per μm^2 on the HOPG, and GNP surface area as the total surface area covered by the GNPs on 1×1 cm^2 HOPG. AFM height images in Figure 29 (low magnification) and Figure 30 (high magnification) illustrate the dependence of the GNP morphology as a function of the $HAuCl_4$ concentration. The applied overpotential is fixed at -0.5 V and the deposition time is fixed at 10 ms. The AFM images show that the GNPs change from smooth hemi-spheres to irregular dendrites when the $HAuCl_4$ concentration is increased above 0.5–1 mM similar to observations by others.[58, 60, 166] With increasing $HAuCl_4$ concentration, the GNP size increases accompanied by a decrease in the particle number density (Figure 29 and Table 6). Typical GNP

dimensions made from 0.1 mM $HAuCl_4$ solution are 11 ± 2 nm in height and 32 ± 6 nm in diameter by AFM sectional analysis. The particle dimensions in 0.5 mM $HAuCl_4$ solution are 20 ± 2 nm in height and 48 ± 7 nm in diameter. The GNP dendrites display a center core with a height of 36–54 nm and dendritic shell whose overall diameter increases from 400 nm in 1 mM $HAuCl_4$ to 1.5 μm in 10 mM $HAuCl_4$ (Figure 30c–e). The data indicate that the $HAuCl_4$ concentration should be kept below 0.5 mM to avoid dendritic crystal growth. We also notice an abrupt change in the particle density coincides with the morphological transition. The particle density below the transition concentration, ~13 particles/μm^2, is roughly 13× the value obtained in 1 mM $HAuCl_4$ and 40× the value in 5–10 mM $HAuCl_4$. It suggests that both primary and secondary nucleation rates increase with increasing concentration. The total GNP covered surface area on 1×1 cm^2 HOPG by AFM shows an increase of the GNP coverage with increasing $HAuCl_4$ concentration (Table 6). The surface area values are obtained from AFM and CV measurements for comparison.

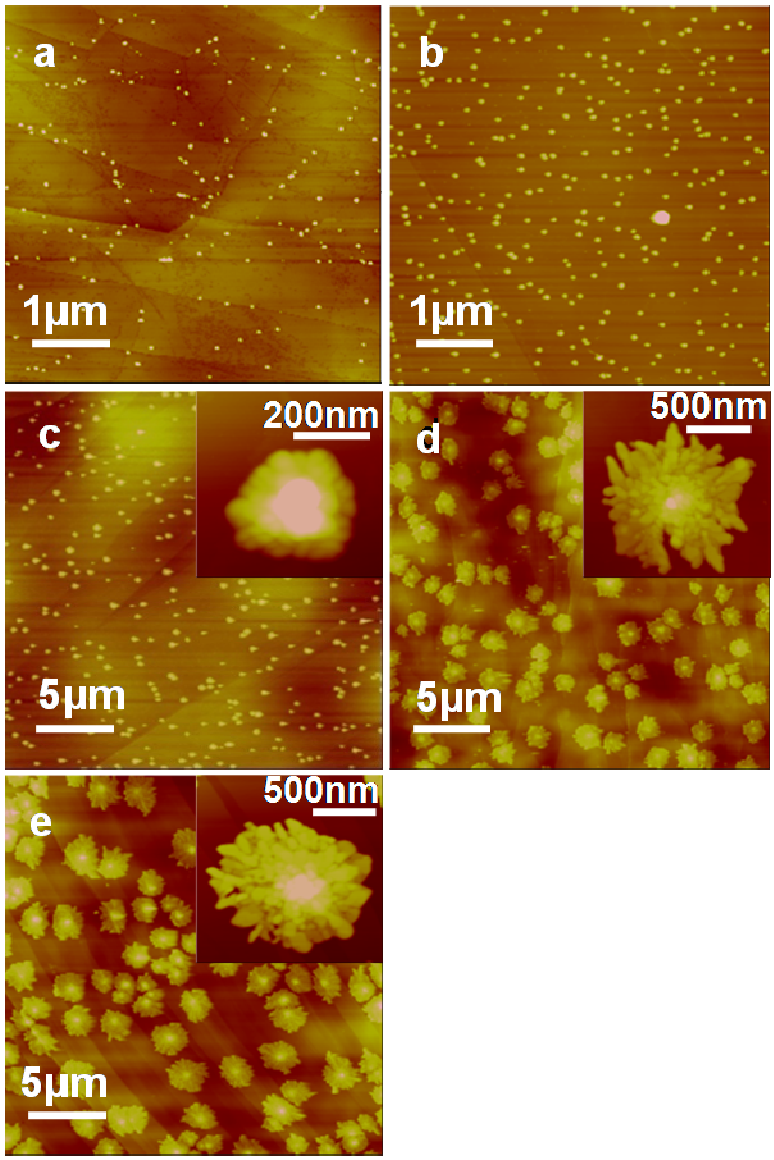

Figure 29. AFM height images of GNP electrodeposition on freshly cleaved HOPG. An overpotential of -0.5 V is applied for 10 ms in electrolyte solutions containing: (a) 0.1 mM; (b) 0.5 mM; (c) 1 mM; (d) 5 mM; and (e) 10 mM $HAuCl_4$. Z range is 20 nm for (a), 50 nm for (b), 100 nm for (c–e), and 50 nm for the inserted images in (c–e).

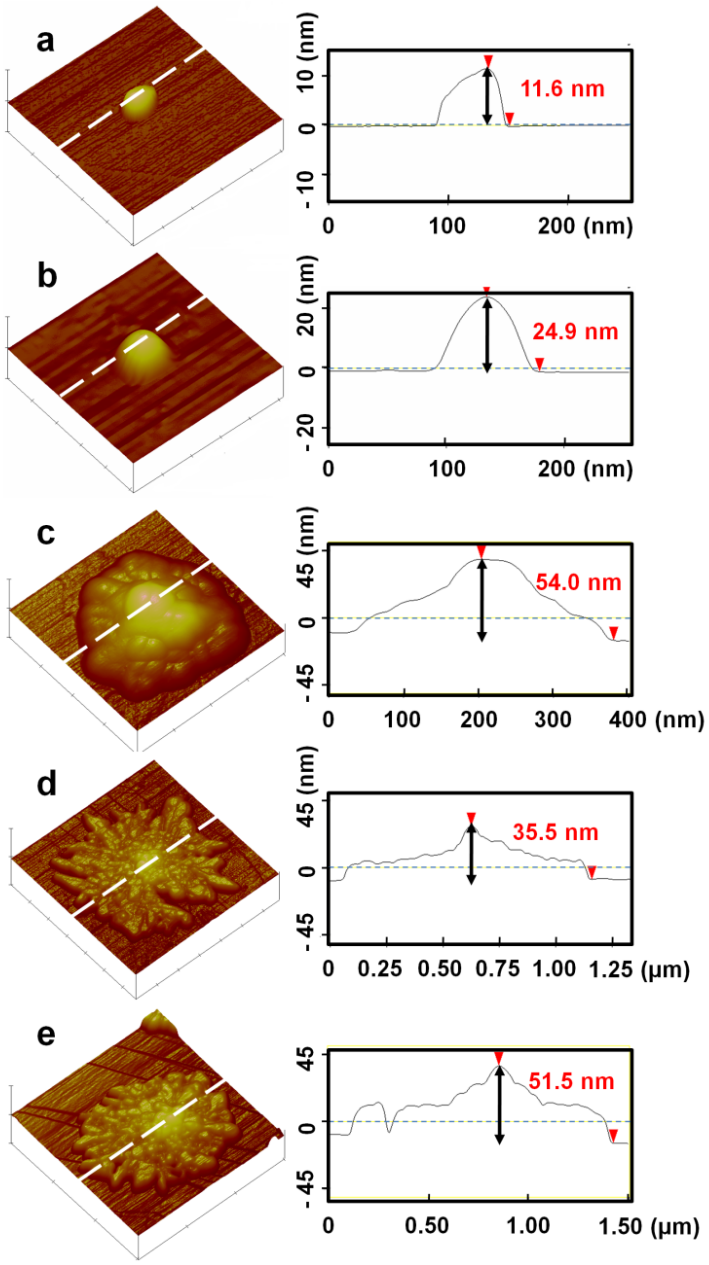

Figure 30. The 3D surface plot (left) and sectional height analysis (right) of AFM images of single GNP electrodeposition on freshly cleaved HOPG. GNP is electrodeposited from (a) 0.1 mM; (b) 0.5 mM; (c) 1 mM; (d) 5 mM; and (e) 10 mM $HAuCl_4$ at overpotential of -0.5 V for 10 ms. The sectional height analysis is measured along the dashed white line on their corresponding 3D surface plot image. Z range is 20 nm for (a), 30 nm for (b), 100 nm for (c-e).

Table 6. The particle size (bearing volume per particle), density (number of particles per μm^2) and surface area (cm^2) of GNP electrodeposited on HOPG with varying $HAuCl_4$ concentration.

$HAuCl_4$ Concentration (mM)	Particle Size ($\times 10^{-3}$ μm^3/particle)	Particle Density (particle/μm^2)	Surface Area by AFM (cm^2)	Surface Area by CV (cm^2)
0.1	0.006 ± 0.004	13.0 ± 3.8	0.005	--
0.5	0.024 ± 0.008	13.3 ± 1.4	0.012	0.007 ±0.003
1.0	0.6 ± 0.3	0.98 ± 0.15	0.032	0.019 ±0.006
5.0	7.2 ± 5.9	0.28 ± 0.05	0.115	0.094 ±0.012
10.0	12.2 ± 8.0	0.22 ± 0.04	0.170	0.206 ±0.019

The surface area of the GNPs on the HOPG can be independently determined from the CV curves obtained during the reduction reaction of the GNP-decorated HOPG in 0.05 M H_2SO_4.[56, 175-183] The CV curves are obtained in the potential range of -0.5–2.0 V at a scan rate of 100 mV/s. The GNP-decorated HOPG electrodes are prepared from 0.1–10 mM $HAuCl_4$ solutions at an overpotential of -0.5 V for 10 ms. Figure 31 shows the cathodic reduction peaks corresponding to the reduction of the oxide of Au^{3+}, formed during the anodic cycle,[46, 47] to Au^0 occurring near 0.4 V on the GNP-decorated HOPG prepared in 0.5–10 mM $HAuCl_4$.[177-178] The cathodic reduction peak of the GNP-decorated HOPG made from 0.1 mM $HAuCl_4$ is too small to be measured. CV scans of freshly cleaved HOPG show no peaks. The reduction peak current on the GNP-decorated HOPG electrodes increases with increasing $HAuCl_4$ concentration.

The surface area of electroactive GNPs is thus estimated based on the number of charges consumed during the Au^{3+} oxide reduction by integrating the catholic peak area in Figure 6. [43, 44] [43, 44] The number of charges for the reduction of a fully covered monolayer is assumed to be 400 μC/cm^2.[56, 181-183] The total surface areas of electroactive GNPs obtained from the CV curves are in a general agreement with those measured by AFM analysis (Table 6).

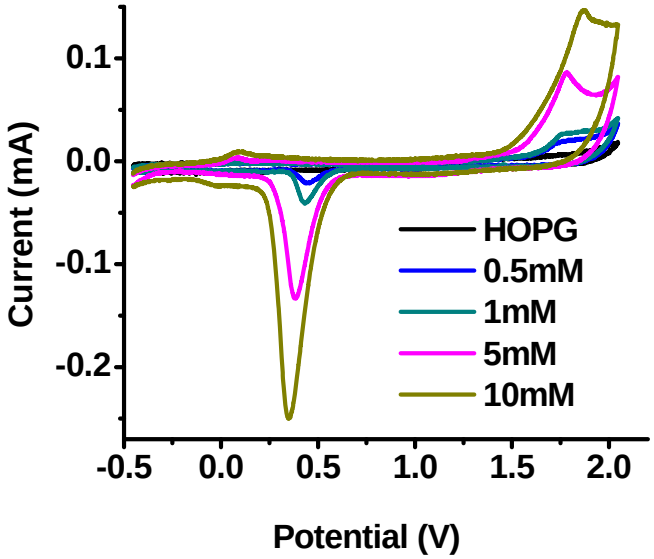

Figure 31. Cyclic voltammograms in 0.05 M H_2SO_4 from -0.5 to 2.0 V with scan rate 100 mV/s on freshly cleaved HOPG and GNP-decorated HOPG electrodes.

Electrodeposition of the GNPs is also studied as a function of applied overpotential and pulse time (Figure 32). The $HAuCl_4$ concentration is fixed at 0.1 mM. Table 7 reports corresponding AFM analysis results of the deposited GNP height, diameter, particle number density, and total covered surface area. The results show that as the applied overpotential becomes more negative (increasing driving force) the height, diameter, and surface area decrease while

the particle density increases. In the applied pulse time range studied no significant changes in the GNP morphology has been observed.

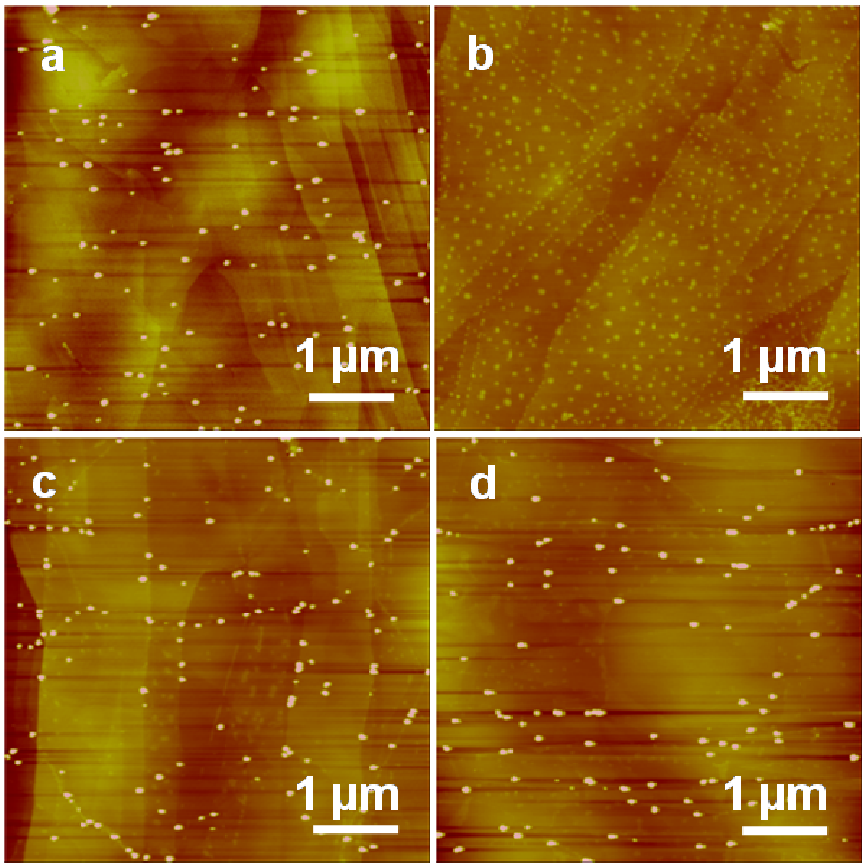

Figure 32. AFM height images of GNP electrodeposition (0.1 mM $HAuCl_4$) on freshly cleaved HOPG. The applied overpotential and deposition time is (a) -0.1 V and 10 ms, (b) -0.9 V and 10 ms, (c) -0.5 V and 0.1 s, and (d) -0.5 V and 1 s, respectively. Z range is 20 nm for all the images.

Table 7. AFM analysis of vertical and lateral dimensions, particle density, and surface area of GNP electrodeposited on HOPG with varying overpotential and deposition time. The gold salt concentration is 0.1 mM.

Overpotential (V)	Deposition Time (s)	Vertical Height (nm)	Lateral Diameter (nm)	Particle Density (particle/μm^2)	Surface Area ($\times 10^{-3} cm^2$)
-0.1	0.01	18.2 ± 4.1	50.3 ± 11.1	4.9 ± 0.8	4.9
-0.5	0.01	11.3 ± 2.1	32.3 ± 6.2	13.0 ± 3.8	5.3
-0.5	0.1	17.9 ± 3.4	43.8 ± 8.2	6.2 ± 1.1	4.7
-0.5	1	20.0 ± 3.8	52.5 ± 7.9	3.9 ± 0.9	4.2
-0.9	0.01	2.3 ± 0.6	34.4 ± 6.4	50.0 ± 5.2	23.2

The electrochemical activities of the GNP-decorated HOPG are further studied by the CV curves of the redox couple of $Fe(CN)_6^{4-/3-}$. Figure 33 shows the CVs obtained in 1 mM $K_3Fe(CN)_6$ with 0.1 M KCl (potential range = -0.5–0.8 V and scan rate = 100 mV/s) on the HOPG with and without the GNPs. Upon the GNP deposition both the anodic peak current (i_{pa}) and the absolute value of cathodic peak current ($|i_{pc}|$) of $Fe(CN)_6^{3-/4-}$ redox activities are increased while the peak potential separation (ΔE_p) is decreased (Figure 33b–e) in comparison the HOPG (Figure 33a). All three attributes point to higher electrochemical activity upon the GNP deposition. Our observations are consistent with studies by others that show increased redox activities when the GNPs are deposited on indium tin oxide.[184] Figure 33b–e show increase in i_{pa} and $|i_{pc}|$ and decease in ΔE_p with increasing $HAuCl_4$ concentration further supporting the conclusion that the increase in the HOPG electrode activities is directly related to the GNP deposition.

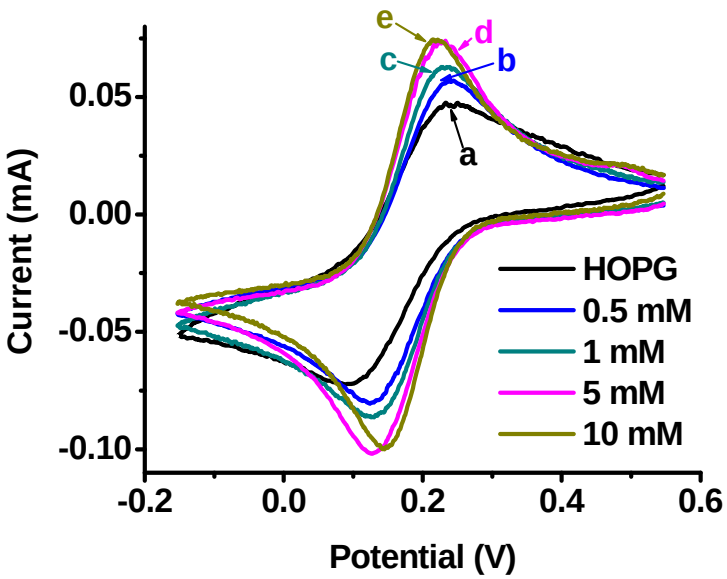

Figure 33. Cyclic voltammegrams in 1 mM $K_3Fe(CN)_6$ /0.1 M KCl from 0.8 V to -0.5 V with scan rate 100 mV/s on (a) freshly cleaved HOPG electrode and (b−e) GNP-decorated HOPG electrodes. GNP-decorated HOPG are electrodeposited at -0.5 V overpotential for 10 ms in (b) 0.5 mM; (c) 1 mM; (d) 5 mM; (e) 10 mM $HAuCl_4$ solutions.

The GNPs electrodeposited on freshly cleaved HOPG are examined by XRD as shown in Figure 34. The GNPs are deposited at overpotential of -0.5 V for 10 ms from 0.1 mM (hemi-spherical GNPs in Figure 29a) and 10 mM $HAuCl_4$ (dendritic GNPs in Figure 29e). The 2θ values at 38.2°, 44.5°, and 82° correspond to the {111}, {200} and {222} crystalline planes of the Au face-centered cubic (fcc) crystal structure. The expected {220} plane at 2θ = 64.6° is too low to be detected. The expected {311} plane at 2θ = 77.5° overlaps graphite C{110} plane.[58] The peak for {222} in the case of dendritic GNPs splits into two peaks at 81.7° and 82.5° (Figure 34c). This may be due to reduced symmetry associated with the dendritic shape. The intensity ratio of {111} and {100} planes

is 146 and 2.2 for Figure 34b and 34c, respectively. The intensity ratio for spherical GNPs is close to the intensity ratio of 1.9 for synthetic GNPs (PDF 00-004-0784).[184] The extremely high intensity of the {111} plane for dendritic GNPs electrodeposited on HOPG indicates that the dendritic GNPs possess the most prominent {111} face parallel the HOPG basal plane. The intrinsic crystalline grain size, τ, is estimated using the Scherrer equation, $\tau = \frac{K\lambda}{\beta \cos\theta}$, where K is the shape factor equaling 0.9 for single crystal with a spherical shape, λ is Cu Kα wavelength, and β is the full width at half maximum peak height. The estimated grain sizes are 28.0 and 26.6 nm for spherical and dendritic GNPs, respectively, by averaging values from 3–4 individual peaks.

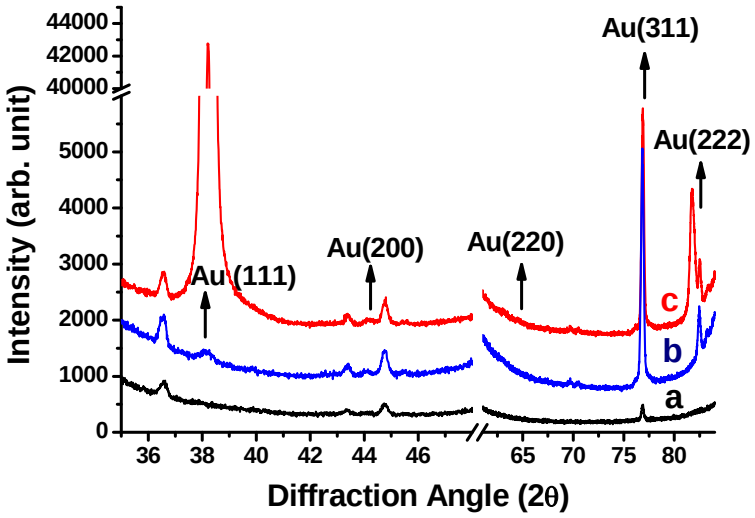

Figure 34. XRD patterns of (a) freshly cleaved HOPG and (b-c) GNP-decorated HOPG electrodes. GNPs are electrodeposited on HOPG at -0.5 V overpotential for 10 ms in (b) 0.1 mM and (c) 10 mM $HAuCl_4$ solutions.

For Au crystals, the surface energy for low-crystalline plane is γ(111) < γ(100) < γ(110), and the thermodynamically most stable structure is truncated octahedron with eight (111) and six (100) faces derived from Wulff construction.[185-187] At kinetically favored conditions using fast growth methods and adding capping agent, a variety of structures of GNPs have been synthesized such as trigonal lamellar plate, icosahedron, octahedron and truncated octahedron, decahedron and truncated decahedron, rhombic dodecahedron, spherical and dendritic structures.[188-197] Our GNPs show several faceted structures as truncated octahedron, cubic, decahedron, spherical and dendritic structures. The spherical and dendritic structures are observed in AFM images in Figure 29&30. Figure 35 presents the FESEM images of GNP with truncated octahedron, cubic and decahedron.

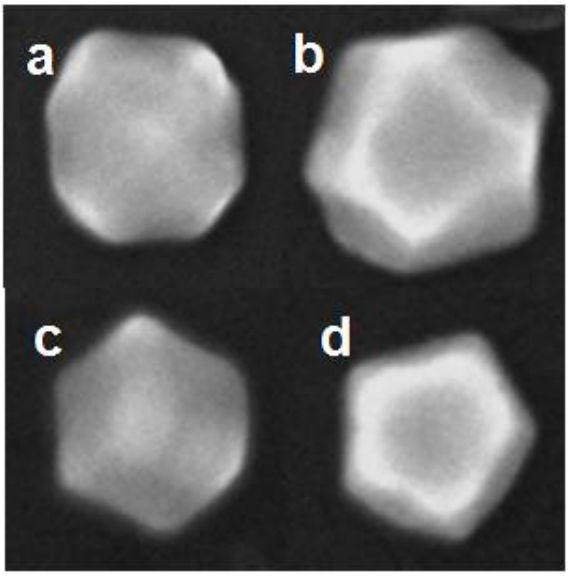

Figure 35. Selected FESEM images of faceted GNP with shapes of (a) and (b) truncated octahedron; (c) cubic; (d) decahedron.

5.3.2 Electrocrystallization of (TTF)$Br_{0.76}$ nanorods on the HOPG electrode.

The control experiments of (TTF)$Br_{0.76}$ electrocrystallization on the bare HOPG are conducted in 5 mM TTF and 0.1 M TBAB in acetonitrile with a potential pulse of 0.5 V for 4 s following the literature.[66] The (TTF)$Br_{0.76}$ crystals grown on the HOPG are needle-like in shape and they do not appear to orient epitaxially on the HOPG basal plane. The (TTF)$Br_{0.76}$ crystal morphology is studied using both AFM and field-emission SEM. Figure 36 shows a side by side comparison of AFM and field-emission SEM images of similarly prepared (TTF)$Br_{0.76}$ crystals on the HOPG. Elongated needle-like crystals can be visualized clearly by both imaging methods. AFM provides precise measurements of the crystal thickness as well as the lateral dimensions of the crystal after taking the tip convolution effect into consideration. The crystal size distribution has been determined to be 250–800 nm in width and 3–13 μm in length by both AFM and field-emission SEM while the crystal height has been determined to be 100–500 nm by AFM sectional height analysis. The EDS attachment to the field-emission SEM provides a means to determine chemical composition of the (TTF)$Br_{0.76}$ crystal. The atomic ratio of S/Br has been determined to be 5.4±1.2 (N=16), which is close to the expected value of 5.3 of the (TTF)$Br_{0.76}$ single crystal structure.

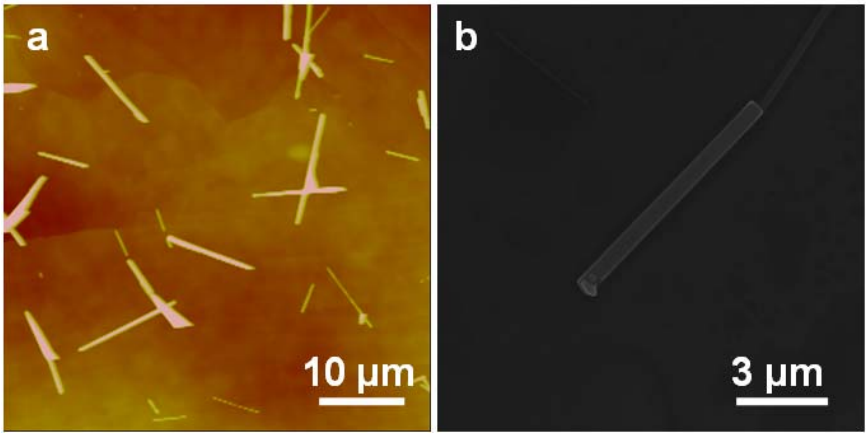

Figure 36. (a) AFM and (b) Field-emission SEM images of the (TTF)$Br_{0.76}$ electrocrystallization on freshly cleaved HOPG. The Z range is 500 nm for (a).

5.3.3 Electrocrystallization of (TTF)$Br_{0.76}$ nanorods on the GNP seeds.

The same electrolytic conditions used in the control experiments are used to grow (TTF)$Br_{0.76}$ crystals on the GNP-decorated HOPG. The TTF concentration is varied from 1 to 10 mM. The crystal morphology is studied by AFM and field-emission SEM. Figure 37 displays the SEM results of GNP induced (TTF)$Br_{0.76}$ rods with various TTF concentrations. It shows a preferential nucleation of the (TTF)$Br_{0.76}$ on the GNP over the HOPG. The percentages of the number of the (TTF)$Br_{0.76}$ crystals attached to a GNP over all (TTF)$Br_{0.76}$ crystals are determined from the SEM images to be 58%, 36%, 66.7%, and 45% for 1, 2.5, 5, and 10 mM TTF, respectively. The preferential nucleation on the GNP is consistent with the higher electrochemical activities of the GNP over the HOPG shown by the CV curves. The results also display much smaller (TTF)$Br_{0.76}$ rods compared with the rods grown on bare HOPG which is due to the higher nucleation rate on the GNP-decorated HOPG. The size of the GNPs and their induced (TTF)$Br_{0.76}$ rods are listed in Table 8. The smallest (TTF)$Br_{0.76}$

rods are found in Figure 37c at 5 mM TTF with 99 ± 48 nm in width and 1.26 ± 0.50 μm in length. The $(TTF)Br_{0.76}$ rods tend to grow into bigger crystals at the TTF concentration below or above 5 mM when using similar GNP-decorated HOPG as the working electrode. Therefore, the optimal concentration for $(TTF)Br_{0.76}$ rod growth is 5 mM.

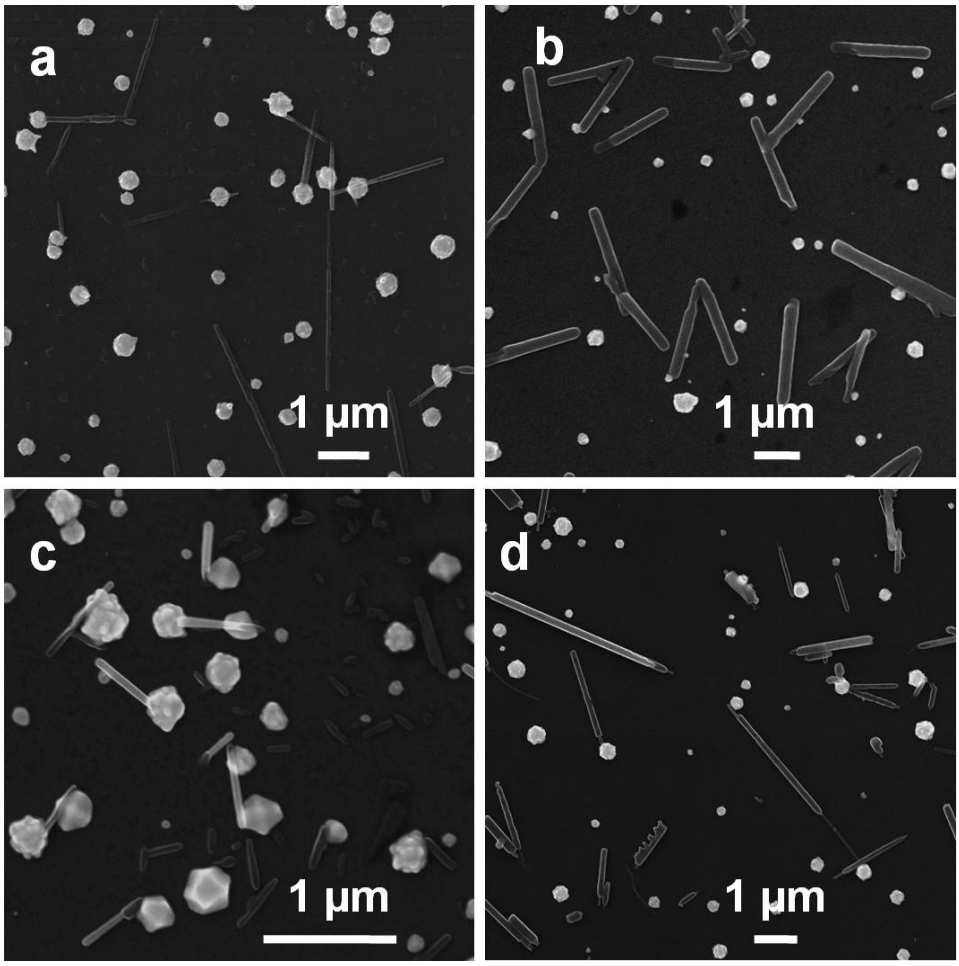

Figure 37. SEM of $(TTF)Br_{0.76}$ electrocrystallization on the GNP-decorated HOPG. The average diameter of GNPs is 300–400 nm. The $(TTF)Br_{0.76}$ rods are electrocrystallized from (a) 1 mM, (b) 2.5 mM, (c) 5 mM, and (d) 10 mM TTF with 0.1 M TBAB in acetonitrile at 0.5 V for 4s.

Table 8. The dimensions of GNP and $(TTF)Br_{0.76}$ rod structure with varying TTF concentration by AFM.

TTF concentration (mM)	GNP Diameter (nm)	$(TTF)Br_{0.76}$ Rod Width (nm)	$(TTF)Br_{0.76}$ Rod Length (μm)
1	401 ± 90	173 ± 65	2.11 ± 1.03
2.5	397 ± 94	254 ± 74	2.03 ± 0.71
5	333 ± 85	99 ± 48	1.26 ± 0.50

Next the GNP size effect on the $(TTF)Br_{0.76}$ electrocrystallization is studied in 5 mM TTF and 0.1 M TBAB in acetonitrile with a potential pulse of 0.5 V for 4 s. Figure 38 shows that preferential nucleation of $(TTF)Br_{0.76}$ crystals on the GNPs and formation of smaller $(TTF)Br_{0.76}$ rods due to the higher nucleation rate on the GNP-decorated HOPG. Table 9 summaries the size measurements of the GNPs and attached $(TTF)Br_{0.76}$ rods by AFM and field-emission SEM. The FESEM images in Figure 38b' and 38c' show similar particle/rod structures with similar size range as obtained by AFM. Both results show that smaller GNPs induce smaller $(TTF)Br_{0.76}$ rod (Figure 38a-b). The smallest $(TTF)Br_{0.76}$ rods were induced by the smallest spherical GNPs as shown in Figure 38a with height of 6.9 ± 1.1 nm, diameter of 32.1 ± 7.7 nm, and length varies from 100 to 500 nm. The smallest spherical GNPs have average height of 19.6 ± 2.1 nm and diameter of 48.1 ± 6.8 nm. The data analysis suggests that the confinement effect on the size of the $(TTF)Br_{0.76}$ rod is different between the spherical and the dendritic GNPs. The $(TTF)Br_{0.76}$ rods induced by the large dendritic GNPs in Figure 38c display smaller height, width, and length than those induced by the large spherical GNPs in Figure 38b.

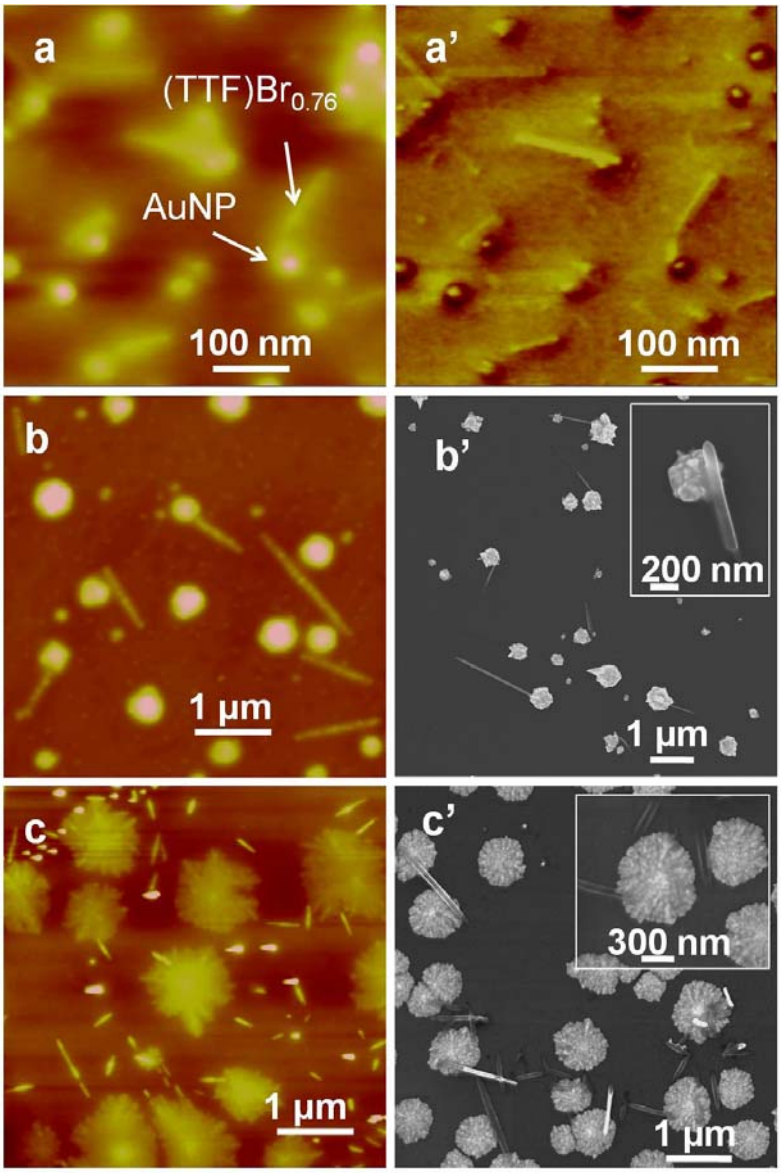

Figure 38. AFM and FESEM images of $(TTF)Br_{0.76}$ electrocrystallization on the GNP-decorated HOPG with various GNP size. (a) – (c) are the AFM height images of $(TTF)Br_{0.76}$ rods attached to the GNP size with increasing GNP diameter. The Z range is 40 nm for (a), 500 nm for (b), and 100 nm for (c). (a') is the AFM phase image of (a). (b') and (c') are the respective FESEM images of (b) and (c). The inserted images in (b') and (c') displays the particle-rod structure with higher resolution.

Table 9. The dimensions of GNP and $(TTF)Br_{0.76}$ rod structure with varying GNP size by AFM.

GNP			$(TTF)Br_{0.76}$			
Height by AFM (nm)	Diameter by AFM (nm)	Diameter by SEM (nm)	Height by AFM (nm)	Width by AFM (nm)	Length by AFM (μm)	Width by SEM (nm)
19.6 ± 2.1	48.1 ± 6.8		6.9 ± 1.1	32.1 ± 7.7	0.1 – 0.5	
134.8 ± 44.1	289 ± 57	333 ± 85	31.8 ± 6.2	106.4 ± 16.8	0.8–2	99 ± 48
19.2 ± 4.8	1050 ± 208	683 ±139	11.4 ± 4.8	54.3 ± 11.8	0.1 – 0.5	71± 20

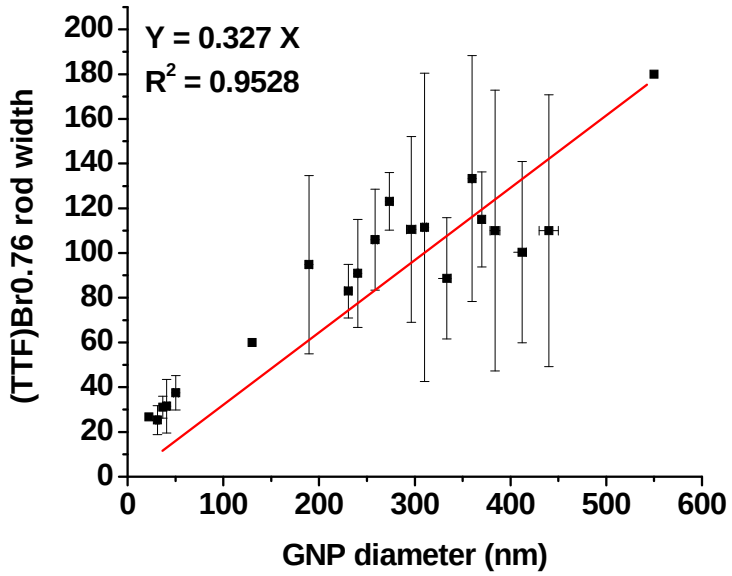

Figure 39. Plot of the average width of the KCP rods as a function of the diameter of the GNPs.

Further data analysis on GNP size effect collects data in several separate experiments. Figure 39 plots the average width of the $(TTF)Br_{0.76}$ rods as a function of the diameter of the spherical GNPs. The GNP diameter ranges from 20 nm to 550 nm and the width of $(TTF)Br_{0.76}$ rods ranges from 25 nm to 180 nm. The plot shows a linear relationship between the GNP diameter and the width of $(TTF)Br_{0.76}$ rods with correlation coefficient R^2= 0.9558. The slope of the plot is 0.327, which means that the average width of the $(TTF)Br_{0.76}$ crystals is 0.327 of

the GNP diameter on which it nucleates and grows. The data analysis is consist with the previous report.[59] Figure 40a presents the histogram of the diameter of the dendritic GNPs and the width of their induced $(TTF)Br_{0.76}$ crystals. The GNP diameter ranges from 250 nm to 1.4 μm and the nanorod width ranges from 30 nm to 100 nm. The nanorod width displays no size dependence of the diameter of the dendritic GNPs on which it nucleates and grows. We then measure the local curvature of the dendritic GNPs which is defined as the vertex width of the dendritic GNPs where the nanorod is attached to. The histogram in Figure 40b shows that the width of the $(TTF)Br_{0.76}$ rods depends more on the local curvature than the overall diameter of the dendritic GNPs. The data analysis suggests that the confinement effect on the size of the $(TTF)Br_{0.76}$ rod is different between the spherical and the dendritic GNPs and the smaller nanorods induced by the dendritic GNPs are due to the small local curvature of the GNPs.

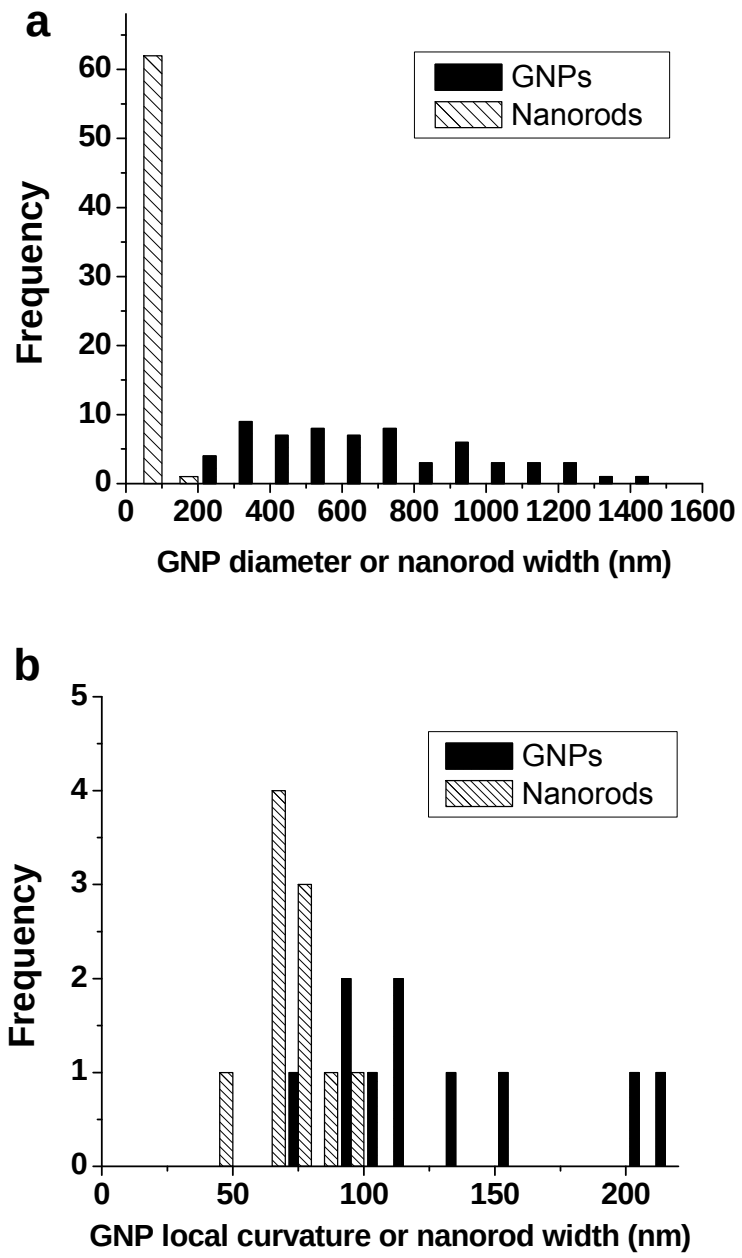

Figure 40. Size distribution for the diameter (a) and local curvature (b) of the dendritic GNPs and the width of their induced (TTF)Br0.76 crystals.

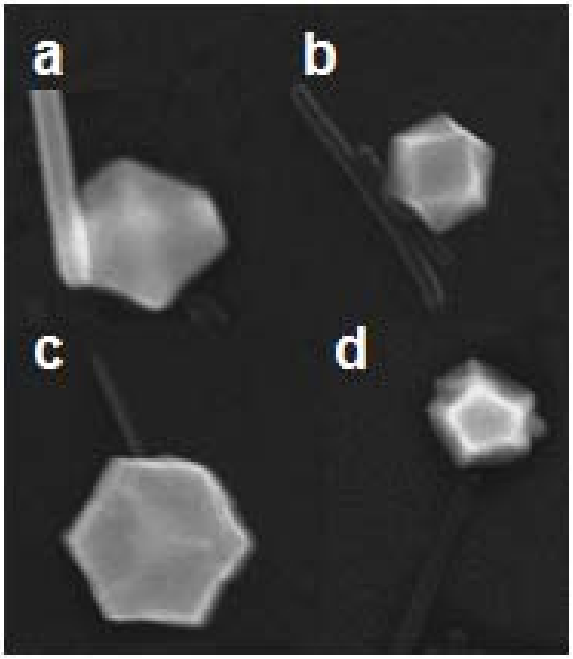

Figure 41. Selected FESEM images of $(TTF)Br_{0.76}$ electrocrystallization on the GNP-decorated HOPG with various GNP shapes: (a) and (b) truncated octahedron; (c) cubic; (d) decahedron.

The faceted GNPs as presented in Figure 35 are also able to induce the electrocrystallization of $(TTF)Br_{0.76}$ nanorods. The field-emission SEM images in Figure 41 show that the $(TTF)Br_{0.76}$ nanorods growing on truncated octahedron, cubic and decahedron GNPs. Most of these nanorods grow at the vertices or sharply truncated edges instead of the dominant (111) face, indicating the nanorod nucleation favors high surface energy.

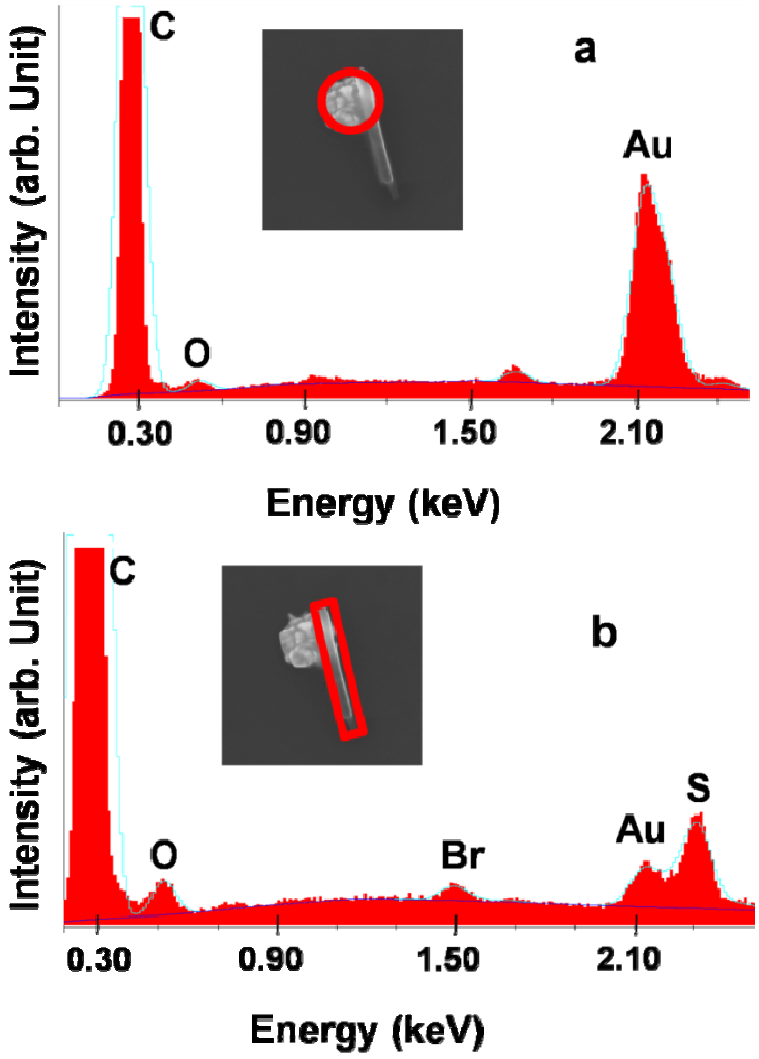

Figure 42. EDS results of one GNP (a) with one (TTF)$Br_{0.76}$ rod (b) on HOPG.

The EDS attached to FESEM provides the chemical composition of the GNP and (TTF)$Br_{0.76}$ rod. The results in Figure 42 indicate that the particle marked by a red circle has a predominant Au peak and the rod marked by a red rectangular has Br, Au and S peaks. The Au peak in the (TTF)$Br_{0.76}$ rod part may due to the overlap of the rod and the GNP. The atomic ratio of S to Br is

estimated to be 5.4 (N = 16), similar with the data of $(TTF)Br_{0.76}$ rod grown on bare HOPG.

5.4 Discussion

5.4.1 GNP Electrodeposition Mechanism.

Metal nanoparticles deposited on planar electrodes promise improved electron transfer kinetics and redox reaction reversibility with characteristics such as narrower peak separation, greater current, and more symmetrical peaks. Metals likely deposit on HOPG as particulates obeying the Volmer-Weber 3-D island growth mechanism because of the weak van der Waals interaction between the metal and graphite lattice.[164] Despite the weak mutual interaction electrodeposited metal nanoparticles on semiconductors display higher electrochemical stability than on metal substrates. One reason is the irreversibility of the electrochemical reaction due to the large bandgap energy between the donor (*e.g.,* Au) states and the conduction band of the semiconductor.[165] In addition, the electrochemical stability of metal nanoparticles is a function of particle size. Ostwald ripening predicts a negative shift in oxidation potential for smaller sizes, which was confirmed by linear sweep voltammograms.[198] One study suggested oxide formation as a reason for the electrochemical stability of metal nanoparticles.[199] Others showed the dissolution behavior to depend on particle coverage and diffusion profiles.[200]

The electrodeposition of gold on HOPG displays different morphologies that depend on the electrolyte concentration, and overpotential. In the classical nucleation theory,[28, 201-202] the free energy of forming a cluster of radius *r*,

interfacial tension γ, and containing *n* molecules, $\Delta G = 4\pi r^2\gamma - n\Delta\mu$, leads to the critical nucleation energy, ΔG_c, and critical nucleus size, $r_c = \frac{2\gamma V}{\Delta\mu}$, for growing into a stable crystal (*V* = molecular volume of the crystallizing compound). The driving force for electrodeposition is expressed as $\Delta\mu = ze|\eta|$, where *z* is the ion valence, *e* is the electron charge, and η is the overpotential.

In the case of changing overpotential at the same electrolyte concentration, the higher driving force for the reaction is achieved by applying more negative overpotential for cathodic reduction or more positive value for anodic oxidation.[46] The nucleus size, $r_c = \frac{2V\gamma}{ze|\eta|}$ is proportional to the reciprocal of η. GNP electrodeposition under our studied conditions shows that applying higher overpotential results in smaller size and more particle coverage which is consistent with the nucleation theory. In the case of changing electrolyte concentration at the same applied overpotential, the definition of the overpotential changes in terms of electrolyte activity as $\eta = \frac{kT}{ze}\ln\frac{a}{a_{eq}}$.[203] The chemical potential difference is governed by the electrolyte activity, similar concept as the supersaturation (*S*) for solution crystallization. The higher driving force is then attained by using a higher electrolyte activity, or concentration. Our results show that at lower Au salt concentration (< 0.5 mM), spherical particles are nucleated during the primary nucleation event. At higher Au salt concentration (> 0.5 mM), the primary nucleation event is followed by secondary nucleation of the dendritic structure giving rise to a characteristic core/shell

structure of spherical core/dendritic shell. In the case of changing electrodeposition time, longer time results in larger size and less particle coverage in consistent with Ostwald ripening.

5.4.2 Nucleation of $(TTF)Br_{0.76}$ nanorods on the GNP-decorated HOPG.

Similar as electrodeposition, the driving force for electrocrystallization can be precisely controlled by overpotential and electrolyte concentration, thus, allowing precise variation of nucleation free energy. The advantage of changing electrolyte concentration and keeping the constant overpotential is to preserve the similar energy state of the electrode surface. We first investigated the electrocrystallization of $(TTF)Br_{0.76}$ on GNP-decorated HOPG electrode by varying TTF concentration and keeping the constant overpotential and deposition time. Our results show the preferred nucleation and confined growth of $(TTF)Br_{0.76}$ crystals on GNPs. The optimal TTF concentration (5 mM) for $(TTF)Br_{0.76}$ crystals is determined at the concentration that the smallest $(TTF)Br_{0.76}$ nanorods grown on the GNPs.

We then studied the GNP size effect on the electrocrystallization of $(TTF)Br_{0.76}$, which follows the seed-mediated nucleation theory. In seed-mediated nucleation (*SMN*),[30] the foreign particle seed lowers the nucleation energy barrier and promotes nucleation at lower supersaturation. The nucleation capability of the surface, *f*, is defined as the ratio of the heterogeneous nucleation barrier, $\Delta G^*_{\text{heter}}$, and the homogeneous nucleation barrier, ΔG^*_{homo} . *f* is a function of *m* and *R'*. Here, $m = (\gamma_{sf} - \gamma_{sc})/\gamma_{cf}$, γ_{ij} is the surface free energy between phases *i* and *j*. The *s*, *f*, and *c* stand for substrate, fluid, and crystal, respectively. In

electrocrystallization, the surface free energy term in *m* factor is related to the electrical activities of the substrate and the foreign particle seed. *R'* is the normalized particle radius of curvature and is the ratio of the radius of the foreign particle seed (R^s) and the critical nucleus size (r_c).

Considering the effect of *m*, the foreign particle seed is more effective in lowering the free energy barrier when the interaction between substrate and crystalline unit becomes stronger. The CV study in Figure 33 shows a higher electric activity of HOPG electrode upon GNP deposition, indicating the electric activity of GNPs is higher than that of the planar HOPG. Therefore, we observed that the $(TTF)Br_{0.76}$ nanorods prefer to nucleate and grow into smaller crystals on GNPs as in Figure 37.

Concerning the effect of *R'*, if the *R'* value is too small (*e.g.* $R' \leq 0.1$) or too large (*e.g.* $R' \geq 10$), the foreign particle seed is considered as either nonstable or a flat surface to the nucleating species and in either case the seed plays no role in lowering the nucleation energy barrier. The effective seed size range is when the seed size is comparable to the size of the nucleating unit (*e.g.* $0.1 < R' < 10$), and *f* decreases with decreasing r_c or increasing *S*.

We are capable of lowering the nucleation energy barrier of $(TTF)Br_{0.76}$ by choosing the proper GNP size range. Under the same electroccrystallization condition with the optimized TTF concentration, the dimensions of the $(TTF)Br_{0.76}$ nanorods are significantly reduced as the GNP size reduces. In Figure 38a, the $(TTF)Br_{0.76}$ crystals nucleated from the smallest GNPs (19.3 ± 10.3 nm in height, 39.1 ± 9.2 nm in diameter) are 6.9 ± 1.1 nm in height and 32.1 ± 7.7 nm in width.

Figure 43a shows the crystal structure of $(TTF)Br_{0.76}$ crystal using the data requested from Cambridge Crystallographic Database. The crystal structure of $(TTF)Br_{0.76}$ is monoclinic, $P2_1/a$, $Z=12$, similar with $(TTF)_7I_5$.[204-207] The lattice parameters for $(TTF)Br_{0.76}$ is a = 4.6851 nm, b = 1.5627 nm, c = 2.4943 nm, and $\beta = 91.23^{o}$ according to single-crystal X-ray data.[66, 206] The crystal has the prominent (010) face parallel to HOPG and extended along the needle axis which is c axis. The interplanar spacing is 1.56 nm of (010) planes and 4.68 nm of (100) planes. The height and width of the smallest $(TTF)Br_{0.76}$ crystals are slightly larger than 4× the interplanar spacing of (010) and (100) planes, respectively. Therefore, the resulting $(TTF)Br_{0.76}$ crystal is formed in needle shape along c axis with 16 unit cells in the cross section (Figure 43b).

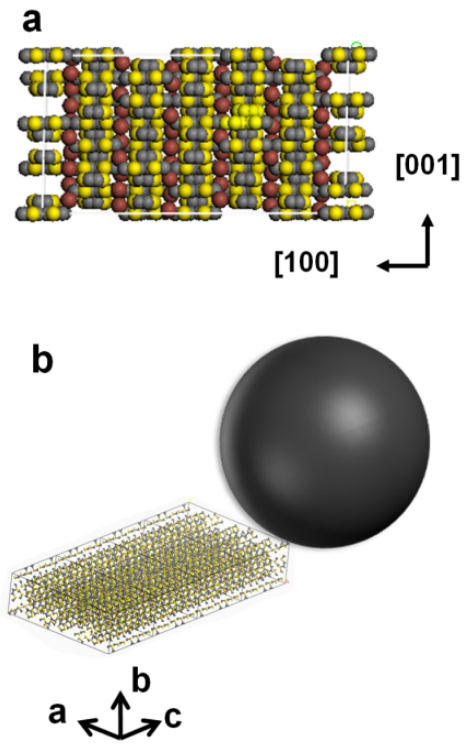

Figure 43. (a) Crystal structure of $(TTF)Br_{0.76}$ exposing the (010) face generated by the Materials Studio program. The structure is based on a single-

crystal X-ray structure in J. Chem. Phys. 64, 2271, 1976. (b) Hypothesized structure of the smallest (TTF)$Br_{0.76}$ molecular rod in Figure 38a attached to one GNP.

One molecular simulation study shows that the foreign particle seeds are effective in colloidal crystallization when the ratio of the seed size and the colloidal particle(crystallzing species) size is larger than five.[44] The simulation results also show that the colloidal cluster forms a 2-D layer around the seed when the ratio is seven and then changes into a radially oriented 1-D narrow rod when the ratio decrease to five. The authors hypothesize that the high curvature of the small seed plays a key role in the formation of the radially elongated 1-D rod. In our case, the high curvature of the GNPs reduces the nucleation energy barrier and promotes (TTF)$Br_{0.76}$ nucleation at the given overpotential and the crystallization is confined to nano scale.

Upon closer examination of the microscopic images, we found that nucleation of TTF nanorods occurs preferentially at the vertices or sharply truncated edges of GNP crystals as well as the tips of GNP dendrites. The electrochemically synthesized GNPs on graphite adopt several apparent shapes including the predominant twinned icosahedral or decahedron shape, hexagonal thin plate shape, and spheroidal shape. Our study suggests that in seed-mediated nucleation morphological features at the nanoscale plays an important role. The well defined predominant seed crystalline faces are less likely to nucleate than those less defined faces.

5.5 Conclusion

This chapter demonstrates a methodology of using inorganic nanoparticles as nucleation seeds for the creation of narrow organic nanorods. By using electrochemical method, the electrodeposition of GNPs on HOPG shows controllable morphology by changing electrolyte concentration and overpotential. The GNP-decorated HOPG shows an improved electrochemical activity upon GNP deposition. Also, the electrocrystallization of TTF displays a preference in nucleation on the GNPs rather than on planar HOPG. The resulting $(TTF)Br_{0.76}$ crystal size is confined and controlled by the TTF concentration, GNP size and morphology. The confinement effect is affected by the NP size. Our study gives rise to the understanding of the nanoconfinement effect imposed by the nanoparticle seed and enables us to create and control the formation of hybrid nanostructures using electrochemical method.

CHAPTER 6

FORMATION OF KCP NANORODS ON GNPs

6.1 Introduction

This chapter describes electrochemical synthesis of partially oxidized potassium tetracyanoplatinate ($K_{1.75}Pt(CN)_4 \cdot 1.5H_2O$, or KCP) nanorod on gold nanoparticle (GNP) nucleation seeds. The seed-mediated process is monitored by cyclic voltammetry, AFM, and FESEM. First the electrodeposition of the GNP nucleation seed on highly oriented pyrolytic graphite (HOPG) electrodes is studied as a function of the electrolytic conditions. The GNP particle size and density is controlled by two-pulse method.[52] The increase in electrochemical activity of the HOPG electrode upon the GNP deposition enables the investigation of seed-mediated nucleation of KCP crystals on the GNP-decorated electrode. We have observed preferential nucleation of KCP crystal on the GNP and the incipient phase displays a confined crystal morphology in comparison to that nucleated on bare HOPG. The confinement effect is investigated as a function of GNP diameter. The KCP nanorod as small as 37 nm in width is nucleated on GNPs of 43 nm in diameter.

$K_{1.75}Pt(CN)_4 \cdot 1.5H_2O$, or KCP, which is known as the Krogmann's salt, is a mixed-valence complex of platinum and tetra-cyanide bonded through linear Pt metal chains.[208-209] The electrical conductivity of KCP crystals measured by four-point probe measurement is 25-50 $\Omega^{-1}cm^{-1}$ at room temperature and increases with increasing temperature.[210] Its metallic conductivity is due to the overlap of the Pt $5d_z^2$ orbitals and the linearly stacked Pt metal chains. $K_2[Pt(CN)_4] \cdot 3H_2O$

can be partially oxidized at the anode surface by applying a potential of 1.5 V and forms needle-shaped KCP crystals with metallic bronze color.[95, 211] The partial oxidation reaction is $1.75K^+ + Pt(CN)_4^{2-} + 1.5H_2O \rightarrow 0.25e^- + K_{1.75}Pt(CN)_4 \bullet 1.5H_2O$, This study contributes basic knowledge to electrocrystallization in nanoconfinement and a possible solution-based nanorod manufacture method. Nanorods have potential applications as ultrasensitive electrochemical sensors, switches, and surface modifiers.

6.2 Experimental

See Chapter 3 for nanoparticle electrodeposition, thin film fabrication via electrocrystallization and characterization techniques.

6.3 Results and Discussion

6.3.1 Electrodeposition of GNPs on HOPG electrode.

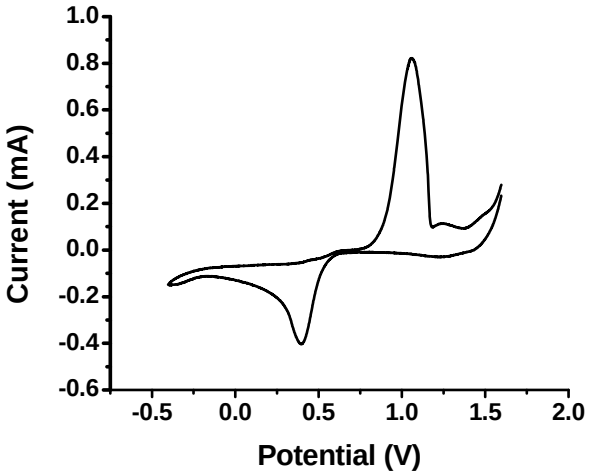

Figure 44. CV curve in 1 mM $HAuCl_4$ solution with 0.1 M KCl as supporting electrolyte on HOPG electrode. The potential range is -0.5–1.5 V. The scan rate is fixed at 100 mV/s.

1–10 mM $HAuCl_4$ aqueous solutions with 0.1 M KCl as supporting electrolyte are used for the GNP electrodeposition on HOPG electrodes. The reduction process occurs on HOPG electrode is under diffusion control with more details analysis in previously chapter. The typical CV curve of $HAuCl_4$ aqueous solutions is shown in Figure 44 with the Au^{3+} reduction peak at 0.4 V and Au oxidation peak at 1.0 V. The onset potential for reduction and oxidation are 0.55 V and 0.85 V, respectively. The equilibrium potential (E_{eq}) for the redox reaction from CV curve is determined as 0.67 V. The overpotential (η) required to initiate the formation of the gold nuclei on HOPG is defined here by the difference between the applied potential, E, and the equilibrium potential, E_{eq}: $\eta = E - E_{eq}$.

Two-pulse method has great potential in controlling the electrodeposition of metal nanoparticles on HOPG electrode by Penner's group.[52-54] Here, we present a modified two-pulse method which is able to control the particle size and density of the electrodeposited GNPs on HOPG electrode. The first pulse is a short nucleation pulse of E = 0.15V (η = -0.5 V) for 10 ms. The second pulse is a long pulse of E = 1.0 V for a few seconds. The applied potential (E = 0.15V) for the first pulse is in the reduction region of the CV curve in Figure 44. The Au^{3+} is reduced to Au^0 and forms GNPs on HOPG during the first pulse. The applied potential (E =1.0 V) for the second pulse is in the oxidation region of the CV curve in Figure 44. Therefore, the electrodeposited GNPs are dissolved into Au ions during the second pulse. The typical FESEM images in Figure 45 presented the morphologies of the GNPs at different electrodeposition conditions. Figure 45a-c presents GNPs electrodeposited from 1 mM $HAuCl_4$ solutions with first

applied pulse of η = -0.5 V for 10 ms and second applied pulse of E = 1.0 V for 0 s, 1 s and 5 s, respectively. The GNPs in Figure 45a is similar to the AFM results in the previous chapter as shown in Figure 29c. In Figure 45b the GNPs dissolved slightly into irregular shapes by applying a second pulse of 1.0 V for 1s. As the applied second pulse extends 5s, the GNPs in Figure 45c become small individual particles. FESEM data analysis demonstrates that the average diameter of the GNPs in Figure 45a is 495 ± 128 nm and reduces to 110 ± 64 nm after dissolving at 1.0 V for 5s (Figure 45c). The average particle densities of the GNPs in Figure 45a-c are 0.17 ± 0.02, 0.20 ± 0.03, and 0.15 ± 0.06 μm^{-2}, respectively. The data analysis indicates that the GNP size can be gradually reduced by carefully applying a dissolving pulse with potentials in the oxidation region of its CV curve and the GNP density remains unchanged during the dissolving process. Figure 45d-f presents GNPs electrodeposited from 10 mM $HAuCl_4$ solutions with same electrodeposition conditions as in Figure 45a-c. Similarly, the morphology of the GNPs changes from dendritic to irregular shaped and finally individual spherical nanoparticles. The average diameter of the dendritic GNPs in Figure 45d is 1.49 ± 0.28 μm and the spherical GNPs in Figure 45f is 47.2 ± 21.3 nm. The large size distribution of the spherical GNPs as displayed in the histogram in Figure 46 is mainly due to the dissolving process of the two-pulse method. GNPs with large size distribution are favored for investigating the GNP size effect on the KCP nanorod formation. The average particle densities of the GNPs in Figure 45d-f are 0.06, 0.22 ± 0.02 and 1.77 ± 0.05 μm^{-2}, respectively.

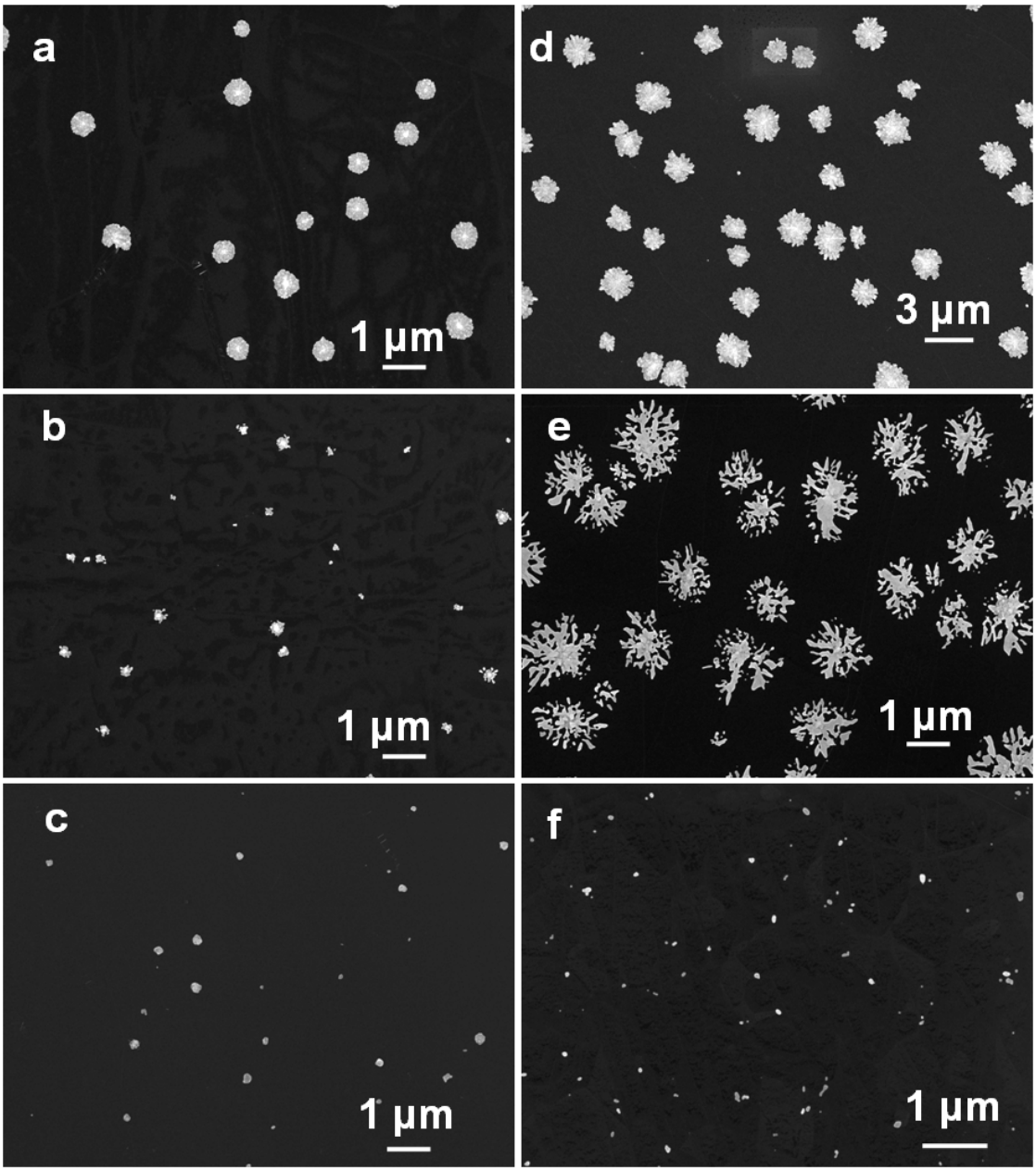

Figure 45. Electrodeposition of GNPs on HOPG using two-pulse method. The HAuCl4 concentration is 1 mM for (a-c) and 10 mM for (d-f). The applied potential and the duration time are as follows: the first pulse is 0.1V for 10ms for all cases, and the second pulse is 1V for 0s for (a, d); 1s for (b, e); and 5s for (c, f).

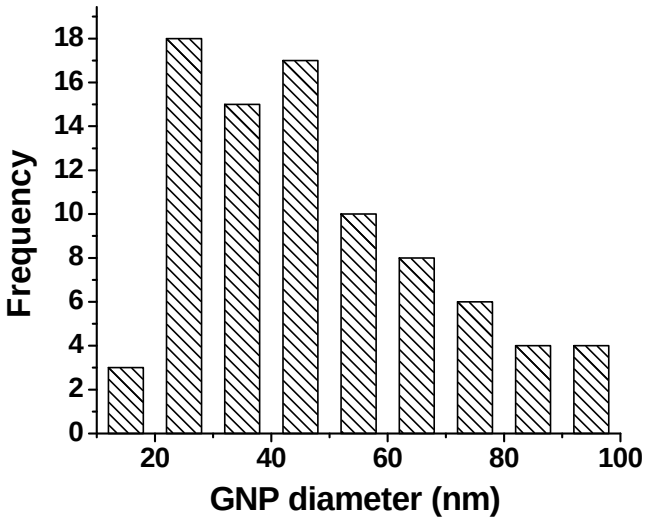

Figure 46. Histogram of the diameters of the GNPs based on FESEM.

6.3.2 Electrocrystallization of KCP on HOPG

The crystalline structure of the KCP is first studied by single X-ray crystallography using a well-formed KCP crystal which is synthesized from 0.3 M $K_2[Pt(CN)_4]\cdot 3H_2O$ in aqueous solution with a potential pulse of 1.5 V for 24 h following the literature.[95] The approximate dimensions of the well-formed KCP crystal are 0.050 mm x 0.090 mm x 0.740 mm. A total of 4255 frames are collected. The total exposure time was 11.82 hours. The frames are integrated with the Bruker SAINT software package using a narrow-frame algorithm. The integration of the data using a triclinic unit cell yield a total of 12479 reflections to a maximum θ angle of 42.41° (0.53 Å resolution), of which 12479 are independent (average redundancy 1.000, completeness = 97.8%, R_{sig} = 6.72%) and 9461 (75.82%) are greater than $2\sigma(F^2)$. The final cell constants of a = 9.2167(10) Å, b = 10.2424(12) Å, c = 11.3110(13) Å, α = 104.232(6)°, β = 109.944(5)°, γ = 106.368(6)°, volume = 891.14(18) $Å^3$, are based upon the

refinement of the XYZ-centroids of 9513 reflections above 20 σ(I) with 4.810° < 2θ < 81.13°. Data are corrected for absorption effects using the multi-scan method (SADABS). The ratio of minimum to maximum apparent transmission is 0.700. The calculated minimum and maximum transmission coefficients (based on crystal size) are 0.0286 and 0.5043. The structure as shown in Figure 47 is solved and refined using the Bruker SHELXTL Software Package, using the space group P - 1, with Z = 2 for the formula unit, $K_3Pt_2(CN)_8 \cdot 3H_2O$. The final anisotropic full-matrix least-squares refinement on F^2 with 226 variables converged at R1 = 4.85%, for the observed data and wR2 = 13.92% for all data. The goodness-of-fit is 0.857. The largest peak in the final difference electron density synthesis is 3.995 $e^-/Å^3$ and the largest hole is -7.569 $e^-/Å^3$ with an RMS deviation of 0.500 $e^-/Å^3$. On the basis of the final model, the calculated density is 1.033 g/cm^3 and F(000), 238 e^-. The single X X-ray crystallography data is consistent with previous reports.[208-209, 212-213]

The control experiments of KCP electrocrystallization on the bare HOPG are then conducted in 0.3 M $K_2[Pt(CN)_4] \cdot 3H_2O$ in aqueous solution with a potential pulse of 1.5 V for various time (few seconds to hrs). Figure 48 shows the typical optical image of KCP crystals grown at 1.5 V for 10 and 60 s on the HOPG electrodes, respectively. The KCP crystals synthesized are needle-shaped crystals with wide size distribution and no epitaxial orientation. The morphology of the KCP crystals electrodeposited on HOPG electrodes is similar with the reported results.[211]

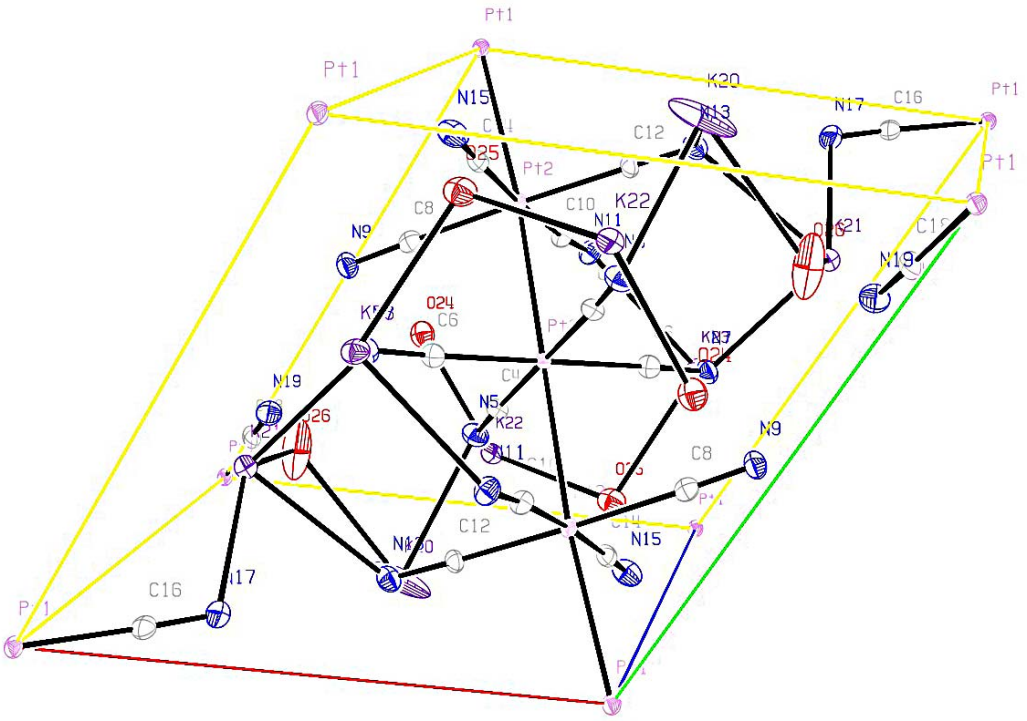

Figure 47. The unit cell drawing of $K_3Pt_2(CN)_8 \cdot 3H_2O$ showing the nonlinear Pt(I)-Pt(2)-Pt(S) chain which extends along [111] direction and has equal Pt-Pt separations.

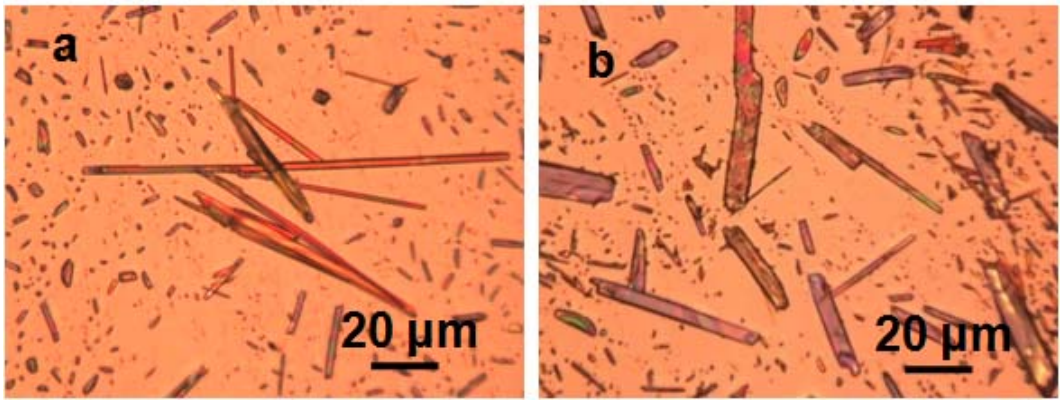

Figure 48. Optical images of KCP crystals grown on HOPG electrodes from 0.3 M $K_2[Pt(CN)_4] \cdot 3H_2O$ solution at 1.5 V for (a) 10 s and (b) 60s.

6.3.3 Electrocrystallization of KCP on GNP-decorated HOPG

The electrocrystallization of KCP crystals is then investigated on various GNP-decorated HOPG electrodes. The particle size and density of the GNP electrodeposited on HOPG electrodes is controlled by the two-pulse methods as discuss in previous section 6.3.1. The electrocrystallization condition for KCP crystal growth is adjusted according to the GNP size and density to ensure the crystallization of KCP rods on GNPs. The $K_2[Pt(CN)_4]\cdot 3H_2O$ concentration is varied from 0.03 for small GNPs to 0.3 M for large and dendritic GNPs. The applied potential for partial oxidation is fixed at 1.5 V and the applied time varies from 0.1 s to 1 s. The KCP crystal morphology is studied by AFM and FESEM. Figure 49 summaries the representative FESEM results of KCP rods induced from GNPs with various diameters. The GNPs are electrodeposited from 10 mM $HAuCl_4$ solutions with 0.1 V for 10 ms for (a), and 0.1 V for 10 ms followed by 1 V for 5 s for (b&c). The KCP electrocrystallization is carried out on GNP-decorated HOPG electrodes in 0.3 M $K_2[Pt(CN)_4]\cdot 3H_2O$ aqueous solutions with applied potential of 1.5 V and applied time of 1 s. In Figure 49c&c' an application of 10 pulses of 1.5 V is applied for 0.1 s per pulse with total applied time of 1 s. The average diameter of the GNPs is 436 ± 251 nm and the average width of the KCP crystals is 190 ± 121 nm. The length of the KCP rods is in the range of 100 nm to 3 μm. Figure 50 presents the FESEM images of KCP crystals induced on small GNPs (diameter of 141.6 ± 84.4 nm) with adjusted electrocrystallization conditions, *i.e.* 0.03 M $K_2[Pt(CN)_4]\cdot 3H_2O$ aqueous solutions with applied potential of 1.5 V and applied time of 0.1s. The average width of the KCP rods is 65.2 ±

15.7 nm. All the FESEM results show a preferential nucleation of the KCP rods on the GNPs over the HOPG. The percentages of the number of the KCP crystals attached to a GNP over all KCP crystals are determined from the FESEM images to be 78%, 100%, 88% and 62% for Figure 49a - c and 50a, respectively. The preferential nucleation on the GNP is consist with the higher electrochemical activities of the GNP over the HOPG shown in previous chapter.

Next the GNP size effect on the KCP electrocrystallization is analyzed from data collecting in several separate experiments due to the wide GNP size distribution. Figure 51 plots the average width of the KCP rods as a function of the diameter of the GNPs. The GNP diameter ranges from 43 nm to 1.1 μm and the average width of KCP rods ranges from 37 nm to 651 nm. The plot shows a linear relationship between the GNP diameter and the width of KCP rods with correlation coefficient R^2= 0.9558. The slope of the plot is 0.422, which means that the average width of the KCP crystals is 0.422 of the GNP diameter on which it nucleates and grows. The data analysis is consist with the previous report.[59]

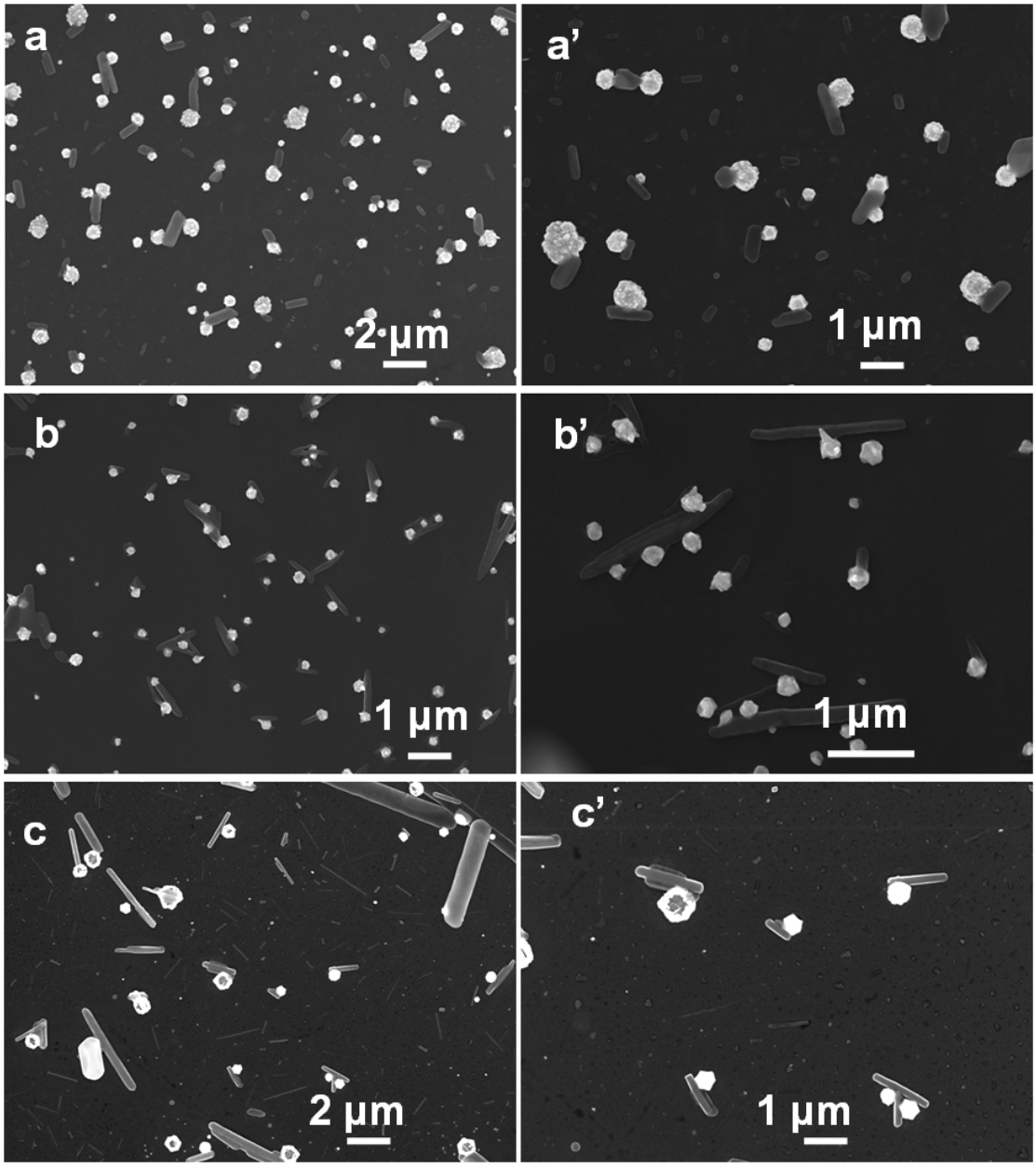

Figure 49. FESEM results of KCP rods induced from GNPs with various diameters in 0.3 M $K_2[Pt(CN)_4]\cdot 3H_2O$ aqueous solutions with applied potential of 1.5 V and applied time of 1s. Figure (a'-c') are high magnification images for Figure (a-c).

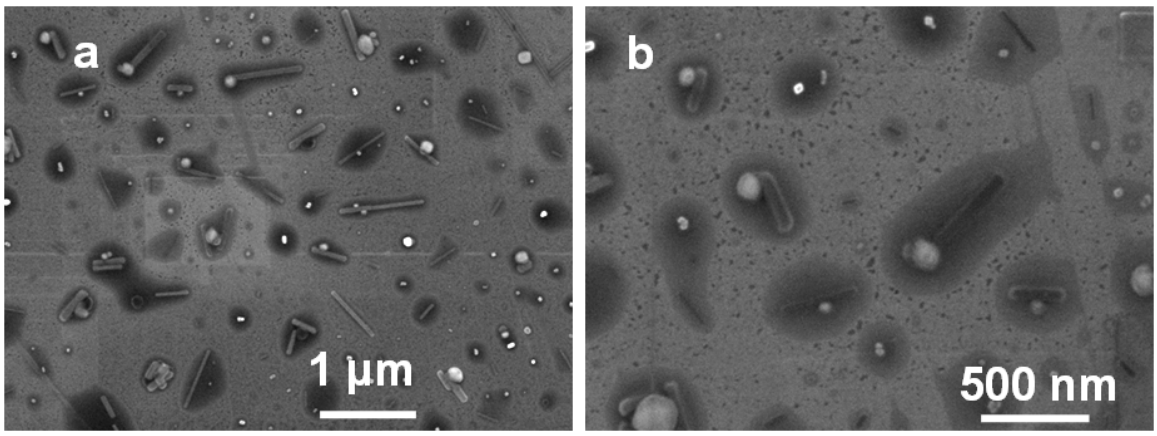

Figure 50. FESEM results of KCP rods induced from GNPs in 0.03 M $K_2[Pt(CN)_4]\cdot 3H_2O$ aqueous solutions with applied potential of 1.5 V and applied time of 0.1s. (a) Low magnification and (b) high magnification.

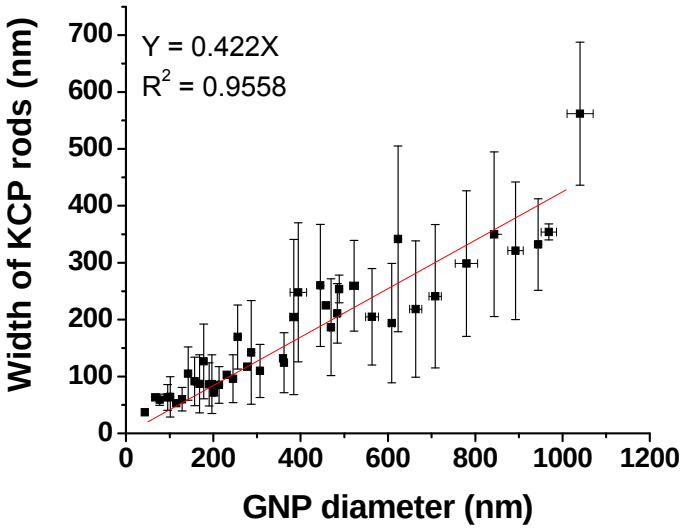

Figure 51. Plot of the average width of the KCP rods as a function of the diameter of the GNPs.

6.3.4 Conductivity measurement of KCP crystals

The electrical conductivity of KCP crystals is measured on patterned Au electrodes using two-point probe method. Figure 52 is a schematic illustration of two prefabricated Au electrodes with a gap of 1 mm between the electrodes. The

Au electrodes are sputtered on SiO_2/Si wafer at 1 mA for 200 s. The KCP crystals are synthesized in 0.3 M $K_2[Pt(CN)_4]\cdot 3H_2O$ aqueous solutions with applied potential of 1.5 V for 24 h. The large needle-shaped KCP crystals (length ~ 1 mm) are collected on Pt (as WE) electrode and then dispersed between the two Au electrodes. The characteristic source-drain current *vs*. source-drain voltage plot of the KCP bulk crystals is shown in Figure 53. The resistance of the KCP crystals is 0.3 MΩ. No clear gate-effect is observed in the source-drain current *vs.* gate voltage plot in the insert plot which indicates that KCP crystal is metallic material.

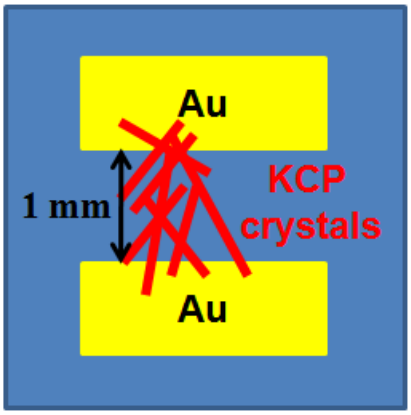

Figure 52. Patterned Au electrodes with electrode gap of 1 mm.

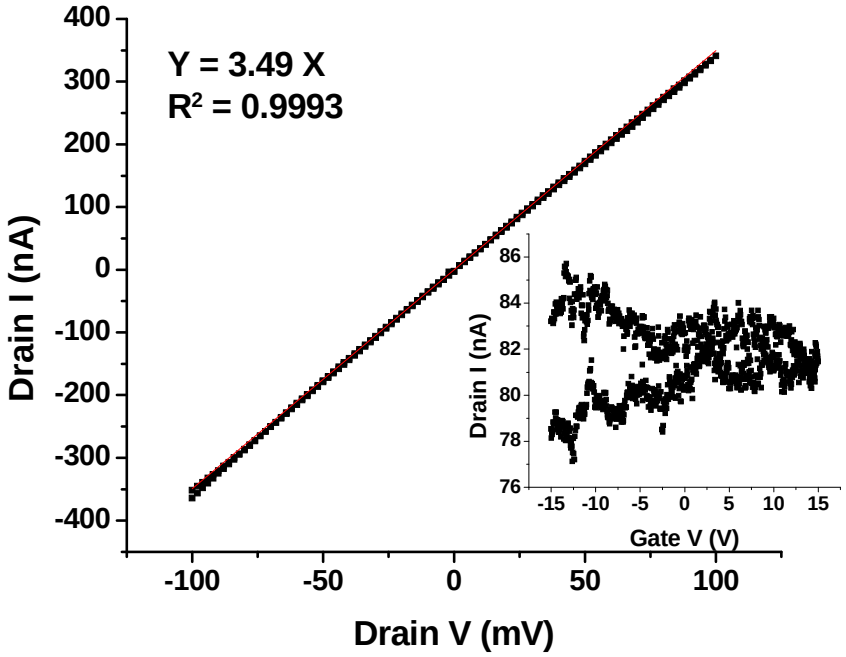

Figure 53. Source-drain current *vs*. source-drain voltage for KCP crystals dispersed between two prefabricated Au electrodes 1 mm apart. Insert image is the plot of source-drain current as a function of gate voltage at source-drain voltage of 0.5 V.

The conductivity measurement is improved for measuring single KCP crystal on patterned Cr/Au electrodes. Figure 54 is a schematic illustration of the fabrication process of the patterned Cr/Au electrodes. The fabrications of these electrodes are done by standard photolithography. In detail, a 300 nm thick SiO_2 layer is thermally grown on the Si substrates as insulator. A 1.1 μm thick photoresist (S1811) is spin coated onto the substrates and followed by softbake at 95°C for 2 min. The expose dose is 35 mJ and the develop time is 1~2 min. The Cr/Au thin film are deposited by E-beam evaporation with thicknesses 5nm/50nm and then defined by the following lift-off process.

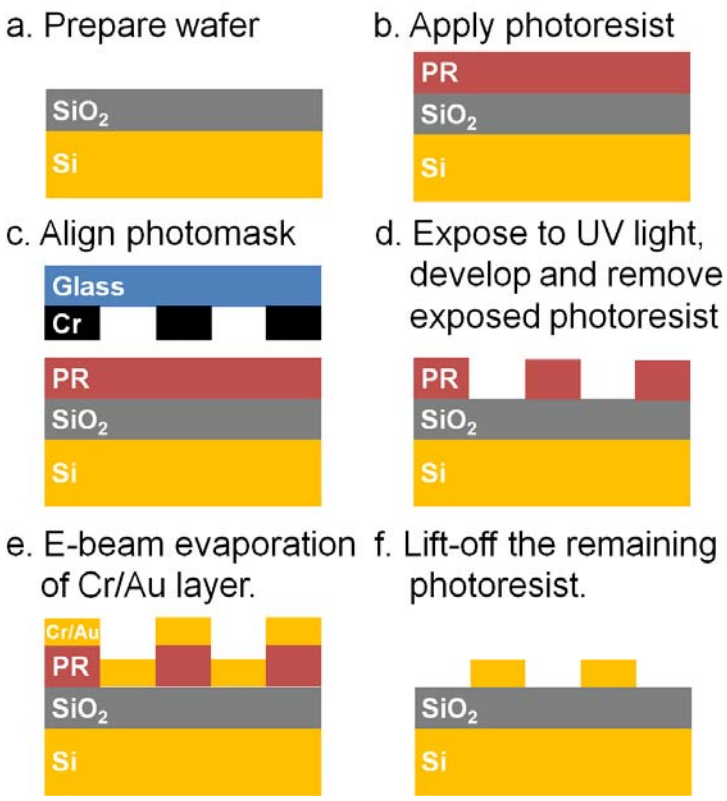

Figure 54. Scheme of the standard photolithography process for patterned Cr/Au electrodes fabrication

Figure 55a illustrates one unit of the patterned electrodes. The width (W) of the Cr/Au electrodes arises from 5 to 50 μm and the separation distance (D) between the microelectrodes changes from 5 to 500 μm. Figure 55b presents one optical image of a KCP rod grow on the patterned Cr/Au electrodes with electrode width (W) and gap (D) of 50 μm. The KCP rod is electrocrystallized in 0.3 M $K_2[Pt(CN)_4]\cdot 3H_2O$ aqueous solutions at 1.5 V for 30 min. The approximate dimensions of the KCP rod is 25 μm × 25 μm × 570 μm. The characteristic source-drain current *vs*. source-drain voltage plot of the KCP bulk crystals is shown in Figure 56. The resistance of the KCP crystals is 23 MΩ. The estimated conductivity of single KCP rod is $0.4 \times 10^{-3}\ \Omega^{-1}cm^{-1}$ at room temperature. No clear

gate-effect is observed in the source-drain current *vs.* gate voltage plot (insert plot in Figure 56) which indicates that KCP crystal is metallic material..

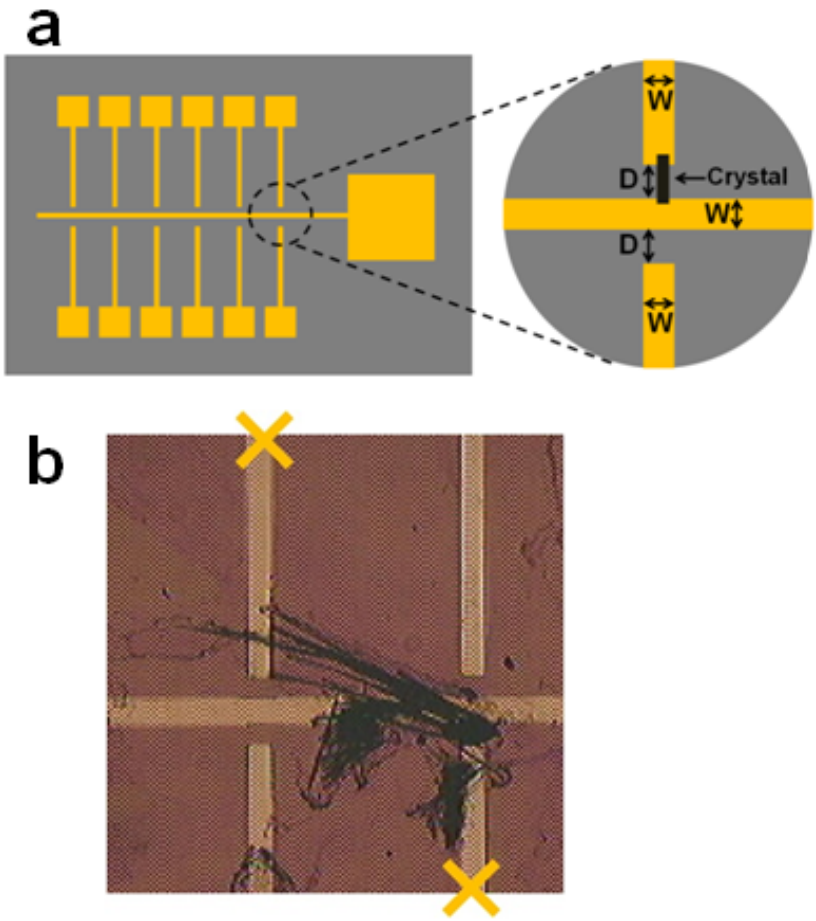

Figure 55. (a) Scheme of the patterned Cr/Au electrodes on SiO_2/Si substrates using standard photolithography process. (b) Optical image of one KCP rod grow on the patterned Cr/Au electrodes. The crosses indicate the electrodes connected for two-point probe measurement.

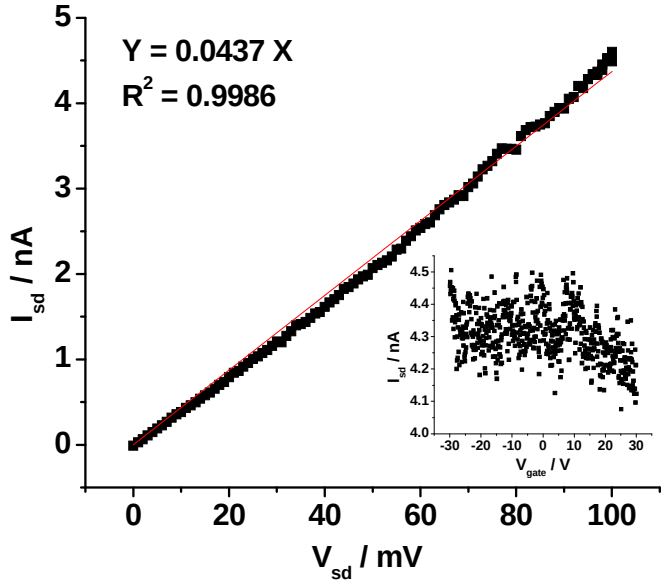

Figure 56. Source-drain current *vs*. source-drain voltage for one KCP crystal grown on patterned Au electrodes. Insert image is the plot of source-drain current as a function of gate voltage at source-drain voltage of 0.5 V.

6.4 Conclusion

This chapter continues the study of using inorganic nanoparticles as nucleation seeds for the creation of narrow organic nanorods via electrochemical method. The electrodeposition of GNPs on HOPG shows controllable morphology using two-pulse method with one nucleation pulse and one dissolving pulse. The GNP size distribution and the particle density are controllable by varying the electrolyte concentration and the electrodeposition conditions. The GNP-decorated HOPG shows an improved electrochemical activity upon GNP deposition. Also, the electrocrystallization of KCP displays a preference in nucleation of over 60% on the GNPs rather than on planar HOPG. The resulting KCP crystal size is confined by the GNP size. The average width of

the KCP crystals is ~ 0.422 of the GNP diameter on which it nucleates and grows. The electrical conductivity of KCP crystals is ~ 0.4×10^{-3} $\Omega^{-1}cm^{-1}$ measured on patterned Au electrodes using two-point probe method. This study gives rise to the understanding of the nanoconfinement effect imposed by the nanoparticle seed and enables us to create and control the formation of hybrid nanostructures using electrochemical method.

CHAPTER 7

CONCLUSIONS AND RECOMMENDATIONS FOR FUTURE RESEARCH

7.1 Conclusions

The overall conclusion of this dissertation is the successful fabrication of organic-inorganic hybrid materials with unique and well-defined particle-rod nanostructure on HOPG. The inorganic metal nanoparticles act as nucleating seeds to initiate and confine the nucleation of organic nanorods via spin coating and electrochemical methods.

One successful method is the formation of *n*-carboxylic acid nanorods on monolayer-protected metal nanoparticles on highly oriented pyrolytic graphite (HOPG) substrate via spin coating. Alkanes and alkane derivatives, such as *n*-carboxylic acids, self-assemble on highly oriented pyrolytic graphite (HOPG) into a persistent molecular packing structure that is dictated by the epitaxial interaction between the carbon chain plane and the HOPG basal plane. Carboxylic acids form 2-D crystalline layers consisting of nano-stripe domains whose periodicity is one or two times the molecular chain length. However, when the molecular ordering occurs in the vicinity of a nanoparticle, this persistent HOPG-dominated nano-stripe pattern is disrupted, and nanorods attached to the nanoparticles become the dominant structure. It is determined that carboxylic acid nanorods can be induced by nanoparticles of different core materials including CdSe, CdS, and Au, as long as the protecting monolayer allows sufficient dispersion and colloidal stability of the nanoparticles in solution. A carboxylic chain length range amenable to the nanorod formation is identified, as

is the relationship between the nanoparticle size and the number of nanorods per nanoparticle. The nanorods tend to be attached on carboxyl-terminated nanoparticles while detached when methyl-terminated nanoparticles are used and the percentage of detached nanorods increases with increasing carbon chain length.

Another successful method is the formation of tetrathiafulvalene bromide ($(TTF)Br_{0.76}$) nanorods and partially oxidized potassium tetracyanoplatinate ($K_{1.75}Pt(CN)_4 \cdot 1.5H_2O$ or KCP) nanorods on GNPs on HOPG by electrocrystallization. By using electrochemical method, the electrodeposition of GNPs on HOPG shows controllable morphology by changing electrolyte concentration and electrodeposition conditions. The GNP-decorated HOPG shows an improved electrochemical activity upon GNP deposition. Both TTF and KCP crystals prefer to nucleate on the GNPs rather than on planar HOPG. The confinement effect is affected by the GNP size. The average width of the TTF and KCP crystals is 0.327 and 0.422 of the GNP diameter on which it nucleates and grows.

This dissertation establishes a universal strategy to form organic-inorganic hybrids with particle-rod nanostructures on HOPG using simple solution-based methods. Our study gives rise to the understanding of the nanoconfinement effect imposed by the nanoparticle seed and enables us to create and control the formation of hybrid nanostructures using electrochemical method.

7.2 Recommendations for Future Research

In this research organic semi-conductors are fabricated on GNP-decorated HOPG electrodes by electrocrystallization. More work is needed to better understand the crystalline structure and the formation mechanism of the semi-conductive rods. The GNP size effect on the nanorod formation provides experimental data for studying nanoconfinement effect in *SMN*. One particularly interesting direction is to study the effect of GNP morphology, i.e. the crystalline structure of the GNPs, on nanorod growth. Liquid-AFM enables the *in situ* observation of the early-stage crystal growth at nano scale and is suitable for the detailed study of electrocrystallization of organic semi-conductions on GNP-decorated electrodes.

In this research the molecular crystallization is directed mainly by random dispersed or electrodeposited metal nanoparticles. More systematic work is needed on molecular crystallization directed by nanopatterns. GNP arrays can be fabricated using particle lithography adapted from Li et al.[67-68] Close-packed monodisperse latex particles are used as an evaporative mask to generate rings or pore-shaped octadecyltrichlorosilane (OTS) structures *via* vapor deposition. After removal of the latex spheres, an array of GNP clusters can be deposited inside the rings or pore-shaped structures. By varying the drying condition to control the water amount, the well-ordered rings or pore-shaped structures can be obtained on the silicon wafer substrate. By varying the latex particle size, the separation distance of the ordered rings or pores will be precisely controlled. These GNP arrays are suitable templates for studying particle-induced carboxylic

acid nanorod nucleation and crystallization. The nanoconfinement effect will be addressed using varied GNP sizes and varied separation distances.

In the future, it is promising to fabricate organic-inorganic electronic devices in nano scale by using electrocrystallization methods based on the seed-mediated nucleation theory.

REFERENCES

1. Shipway, A. N.; Katz, E.; Willner, I., Nanoparticle arrays on surfaces for electronic, optical, and sensor applications. *Chemphyschem* **2000,** 1, (1), 18-52.

2. Guo, S. J.; Wang, E. K., Synthesis and electrochemical applications of gold nanoparticles. *Analytica Chimica Acta* **2007,** 598, (2), 181-192.

3. Cooper, J. S.; Raguse, B.; Chow, E.; Hubble, L.; Muller, K. H.; Wieczorek, L., Gold Nanoparticle Chemiresistor Sensor Array that Differentiates between Hydrocarbon Fuels Dissolved in Artificial Seawater. *Analytical Chemistry* **2010,** 82, (9), 3788-3795.

4. Tokonami, S.; Shiigi, H.; Nagaoka, T., Preparation of nanogapped gold nanoparticle array for DNA detection. *Electroanalysis* **2008,** 20, (4), 355-360.

5. Tokonami, S.; Shiigi, H.; Nagaoka, T., Open Bridge-Structured Gold Nanoparticle Array for Label-Free DNA Detection. *Analytical Chemistry* **2008,** 80, (21), 8071-8075.

6. Favier, F.; Walter, E. C.; Zach, M. P.; Benter, T.; Penner, R. M., Hydrogen sensors and switches from electrodeposited palladium mesowire arrays. *Science* **2001,** 293, (5538), 2227-2231.

7. Walter, E. C.; Favier, F.; Penner, R. M., Palladium mesowire Arrays for fast hydrogen sensors and hydrogen-actuated switches. *Analytical Chemistry* **2002,** 74, (7), 1546-1553.

8. Walter, E. C.; Ng, K.; Zach, M. P.; Penner, R. M.; Favier, F., Electronic devices from electrodeposited metal nanowires. *Microelectronic Engineering* **2002,** 61-2, 555-561.

9. Katz, H. E.; Huang, J., Thin-Film Organic Electronic Devices. *Annual Review of Materials Research* **2009,** 39, (1), 71-92.

10. Norbert, K., Organic Electronic Devices and Their Functional Interfaces. In *Chemphyschem*, 2007; pp 1438-1455.

11. Keng-Hoong, Y.; Zijian, Z.; Ziqi, L.; Richard, H. F.; Wilhelm, T. S. H.; Ji-Seon, K., Efficient Conjugated-Polymer Optoelectronic Devices Fabricated by Thin-Film Transfer-Printing Technique. In *Advanced Functional Materials*, 2008; pp 1012-1019.

12. Essig, S.; Marquardt, C. W.; Vijayaraghavan, A.; Ganzhorn, M.; Dehm, S.; Hennrich, F.; Ou, F.; Green, A. A.; Sciascia, C.; Bonaccorso, F.; Bohnen, K. P.; Löhneysen, H. v.; Kappes, M. M.; Ajayan, P. M.; Hersam, M. C.; Ferrari, A. C.; Krupke, R., Phonon-Assisted Electroluminescence from Metallic Carbon Nanotubes and Graphene. *Nano Letters* **2010**.

13. Besteman, K.; Lee, J. O.; Wiertz, F. G. M.; Heering, H. A.; Dekker, C., Enzyme-coated carbon nanotubes as single-molecule biosensors. *Nano Letters* **2003,** 3, (6), 727-730.

14. Munge, B.; Liu, G. D.; Collins, G.; Wang, J., Multiple enzyme layers on carbon nanotubes for electrochemical detection down to 80 DNA copies. *Analytical Chemistry* **2005,** 77, (14), 4662-4666.

15. Bi, S.; Zhou, H.; Zhang, S., Multilayers enzyme-coated carbon nanotubes as biolabel for ultrasensitive chemiluminescence immunoassay of cancer biomarker. *Biosensors and Bioelectronics* **2009,** 24, (10), 2961-2966.

16. Wang, Y. D.; Joshi, P. P.; Hobbs, K. L.; Johnson, M. B.; Schmidtke, D. W., Nanostructured biosensors built by layer-by-layer electrostatic assembly of enzyme-coated single-walled carbon nanotubes and redox polymers. *Langmuir* **2006,** 22, (23), 9776-9783.

17. Haberkorn, N.; Lechmann, M. C.; Sohn, B. H.; Char, K.; Gutmann, J. S.; Theato, P., Templated Organic and Hybrid Materials for Optoelectronic Applications. *Macromol Rapid Comm* **2009,** 30, (14), 1146-1166.

18. Hirst, A. R.; Escuder, B.; Miravet, J. F.; Smith, D. K., High-Tech Applications of Self-Assembling Supramolecular Nanostructured Gel-Phase Materials: From Regenerative Medicine to Electronic Devices. *Angew Chem Int Edit* **2008,** 47, (42), 8002-8018.

19. Ana, B. D.; Ramón, M.-M.; Félix, S.; Katrin, H.; Knut, R., The Supramolecular Chemistry of Organic-Inorganic Hybrid Materials. In *Angewandte Chemie International Edition*, 2006; pp 5924-5948.

20. Katz, E.; Willner, I., Integrated nanoparticle-biomolecule hybrid systems: Synthesis, properties, and applications. *Angew Chem Int Edit* **2004,** 43, (45), 6042-6108.

21. Li, J.; Zhang, J. Z., Optical properties and applications of hybrid semiconductor nanomaterials. *Coordination Chemistry Reviews* **2009,** 253, (23-24), 3015-3041.

22. Fischler, M.; Simon, U., Metal nanoparticle-DNA hybrids - from assembly towards functional conjugates. *J Mater Chem* **2009,** 19, (11), 1518-1523.

23. Buonsanti, R.; Grillo, V.; Carlino, E.; Giannini, C.; Curri, M. L.; Innocenti, C.; Sangregorio, C.; Achterhold, K.; Parak, F. G.; Agostiano, A.; Cozzoli, P. D., Seeded growth of asymmetric binary nanocrystals made of a semiconductor TiO_2 rodlike section and a magnetic gamma-Fe_2O_3 spherical domain. *Journal of the American Chemical Society* **2006,** 128, (51), 16953-16970.

24. Buonsanti, R.; Grillo, V.; Carlino, E.; Giannini, C.; Gozzo, F.; Garcia-Hernandez, M.; Garcia, M. A.; Cingolani, R.; Cozzoli, P. D., Architectural Control of Seeded-Grown Magnetic-Semicondutor Iron Oxide-TiO2 Nanorod Heterostructures: The Role of Seeds in Topology Selection. *Journal of the American Chemical Society* **2010,** 132, (7), 2437-2464.

25. Shi, Y.; Yang, R. Z.; Yuet, P. K., Easy decoration of carbon nanotubes with well dispersed gold nanoparticles and the use of the material as an electrocatalyst. *Carbon* **2009,** 47, (4), 1146-1151.

26. Soundrapandian, C.; Sa, B.; Datta, S., Organic-Inorganic Composites for Bone Drug Delivery. *Aaps Pharmscitech* **2009,** 10, (4), 1158-1171.

27. Ostwald, W., Studien über die Bildung und Umwandlung fester Körper. 1. Abhandlung: Übersättigung und Überkaltung. *Zeitschrift für Physikalische Chemie* **1897,** 22, 289-330.

28. Kashchiev, D., *Nucleation: Basic Theory with Applications*. Butterworth-Heinemann: Oxford: **2000**.

29. Fletcher, N. H., Size Effect in Heterogeneous Nucleation. *The Journal of Chemical Physics* **1958,** 29, (3), 572-576.

30. Liu, X. Y., *Generic Mechanism of Heterogeneous Nucleation and Molecular Interfacial Effects* Elsevier Sci. B. V.: Amsterdam, **2001**.

31. Chayen, N. E.; Saridakis, E.; El-Bahar, R.; Nemirovsky, Y., Porous silicon: an effective nucleation-inducing material for protein crystallization. *Journal of Molecular Biology* **2001,** 312, (4), 591-595.

32. Chayen, N. E.; Saridakis, E.; Sear, R. P., Experiment and theory for heterogeneous nucleation of protein crystals in a porous medium. *Proceedings of the National Academy of Sciences of the United States of America* **2006,** 103, (3), 597-601.

33. Ha, J. M.; Wolf, J. H.; Hillmyer, M. A.; Ward, M. D., Polymorph selectivity under nanoscopic confinement. *Journal of the American Chemical Society* **2004,** 126, (11), 3382-3383.

34. Ha, J. M.; Hillmyer, M. A.; Ward, M. D., Thermotropic properties of organic nanocrystals embedded in ultrasmall crystallization chambers. *Journal of Physical Chemistry B* **2005,** 109, (4), 1392-1399.

35. Hamilton, B. D.; Weissbuch, I.; Lahav, M.; Hillmyer, M. A.; Ward, M. D., Manipulating Crystal Orientation in Nanoscale Cylindrical Pores by Stereochemical Inhibition. *Journal of the American Chemical Society* **2009,** 131, (7), 2588-2596.

36. Ha, J. M.; Hamilton, B. D.; Hillmyer, M. A.; Ward, M. D., Phase Behavior and Polymorphism of Organic Crystals Confined within Nanoscale Chambers. *Crystal Growth & Design* **2009,** 9, (11), 4766-4777.

37. Hamilton, B. D.; Ha, J. M.; Hillmyer, M. A.; Ward, M. D., Manipulating Crystal Growth and Polymorphism by Confinement in Nanoscale Crystallization Chambers. *Accounts Chem. Res.* **2012,** 45, (3), 414-423.

38. Ha, J.-M.; Hamilton, B. D.; Hillmyer, M. A.; Ward, M. D., Alignment of Organic Crystals under Nanoscale Confinement. *Crystal Growth & Design* **2012,** 12, (9), 4494-4504.

39. Mao, G. Z.; Chen, D. Z.; Handa, H.; Dong, W. F.; Kurth, D. G.; Mohwald, H., Deposition and aggregation of aspirin molecules on a phospholipid bilayer pattern. *Langmuir* **2005,** 21, (2), 578-585.

40. Mao, G. Z.; Dong, W. F.; Kurth, D. G.; Mohwald, H., Synthesis of copper sulfide nanorod arrays on molecular templates. *Nano Letters* **2004,** 4, (2), 249-252.

41. Dong, W. F.; Wang, R. M.; Mao, G. Z.; Mohwald, H., Self-assembled molecular patterns of fatty acid on graphite in the presence of metal ions. *Soft Matter* **2006,** 2, (8), 686-692.

42. Chen, D. Z.; Wang, R. M.; Arachchige, I.; Mao, G. Z.; Brock, S. L., Particle-rod hybrids: Growth of arachidic acid molecular rods from capped cadmium selenide nanoparticles. *Journal of the American Chemical Society* **2004,** 126, (50), 16290-16291.

43. Bond, A. D., On the crystal structures and melting point alternation of the n-alkyl carboxylic acids. *New Journal of Chemistry* **2004,** 28, (1), 104-114.

44. Cacciuto, A.; Auer, S.; Frenkel, D., Onset of heterogeneous crystal nucleation in colloidal suspensions. *Nature* **2004,** 428, (6981), 404-406.

45. Cacciuto, A.; Frenkel, D., Simulation of colloidal crystallization on finite structured templates. *Physical Review E* **2005,** 72, (4), -.

46. Bard, A. J.; Faulkner, L. R., *Electrochemical Methods: Fundamentals and Applications*. 2nd ed.; Wiley: New York, **2001**; p 833.

47. Batail, P.; Boubekeur, K.; Fourmigue, M.; Gabriel, J. C. P., Electrocrystallization, an invaluable tool for the construction of ordered, electroactive molecular solids. *Chemistry of Materials* **1998,** 10, (10), 3005-3015.

48. Michev, A., *Electrocrystallization: fundamentals of nucleation and growth*. Boston, Mass.; Kluwer Academic Publishers: c2002.

49. Staikov, G., *Electrocrystallization in Nanotechnology*. WILEY-VCH Verlag GmbH & Co. KGaA: Weinheim, 2007; p 6.

50. Milchev, A., Electrocrystallization: Nucleation and growth of nano-clusters on solid surfaces. *Russian Journal of Electrochemistry* **2008,** 44, (6), 619-645.

51. Milchev, A., Electrochemical phase formation: some fundamental concepts. *Journal of Solid State Electrochemistry* **2011,** 15, (7-8), 1401-1415.

52. Penner, R. M., Mesoscopic metal particles and wires by electrodeposition. *Journal of Physical Chemistry B* **2002,** 106, (13), 3339-3353.

53. Liu, H.; Penner, R. M., Size-selective electrodeposition of mesoscale metal particles in the uncoupled limit. *Journal of Physical Chemistry B* **2000,** 104, (39), 9131-9139.

54. Liu, H.; Favier, F.; Ng, K.; Zach, M. P.; Penner, R. M., Size-selective electrodeposition of meso-scale metal particles: a general method. *Electrochimica Acta* **2001,** 47, (5), 671-677.

55. Wang, L. P.; Mao, W.; Ni, D. D.; Di, J. W.; Wu, Y.; Tu, Y. F., Direct electrodeposition of gold nanoparticles onto indium/tin oxide film coated glass and its application for electrochemical biosensor. *Electrochemistry Communications* **2008,** 10, (4), 673-676.

56. Lin, T. H.; Hung, W. H., Electrochemical Deposition of Gold Nanoparticles on a Glassy Carbon Electrode Modified with Sulfanilic Acid. *Journal of The Electrochemical Society* **2009,** 156, (2), D45-D50.

57. Coskun, U. C.; Mebrahtu, H.; Huang, P. B.; Huang, J.; Sebba, D.; Biasco, A.; Makarovski, A.; Lazarides, A.; LaBean, T. H.; Finkelstein, G., Single-electron transistors made by chemical patterning of silicon dioxide substrates and selective deposition of gold nanoparticles. *Applied Physics Letters* **2008,** 93, (12).

58. El-Deab, M. S.; Sotomura, T.; Ohsaka, T., Morphological selection of gold nanoparticles electrodeposited on various substrates. *Journal of The Electrochemical Society* **2005,** 152, (11), C730-C737.

59. Favier, F.; Liu, H. T.; Penner, R. M., Size-selective growth of nanoscale tetrathiafulvalene bromide crystallites on platinum particles. *Advanced Materials* **2001,** 13, (20), 1567-1570.

60. Boxley, C. J.; White, H. S.; Lister, T. E.; Pinhero, P. J., Electrochemical deposition and reoxidation of Au at highly oriented pyrolytic graphite. Stabilization of Au nanoparticles on the upper plane of step edges. *Journal of Physical Chemistry B* **2003,** 107, (2), 451-458.

61. Bayati, M.; Abad, J. M.; Nichols, R. J.; Schiffrin, D. J., Substrate Structural Effects on the Synthesis and Electrochemical Properties of Platinum

Nanoparticles on Highly Oriented Pyrolytic Graphite. *Journal of Physical Chemistry C* **2010,** 114, (43), 18439-18448.

62. Chiang, T. C.; Reddoch, A. H.; Williams, D. F., Electrolytic Preparation and EPR Study of Crystalline Pyrene, Perylene, and Azulene Perchlorates. *The Journal of Chemical Physics* **1971,** 54, (5), 2051-2055.

63. Ferraris, J.; Cowan, D. O.; Walatka, V.; Perlstein, J. H., Electron transfer in a new highly conducting donor-acceptor complex. *Journal of the American Chemical Society* **1973,** 95, (3), 948-949.

64. Coleman, L. B.; Cohen, M. J.; Sandman, D. J.; Yamagishi, F. G.; Garito, A. F.; Heeger, A. J., Superconducting fluctuations and the peierls instability in an organic solid. *Solid State Communications* **1973,** 12, (11), 1125-1132.

65. Euler, W. B.; Melton, M. E.; Hoffman, B. M., Thermodynamics of Molecular-Metal Formation - Metallophthalocyanine and Tetrathiafulvalene Iodides. *Journal of the American Chemical Society* **1982,** 104, (22), 5966-5971.

66. Hillier, A. C.; Ward, M. D., Atomic force microscopy of the electrochemical nucleation and growth of molecular-crystals. *Science* **1994,** 263, (5151), 1261-1264.

67. Mas-Torrent, M.; Hadley, P., Electrochemical growth of organic conducting microcrystals of tetrathiafulvalene bromide. *Small* **2005,** 1, (8-9), 806-808.

68. Hillier, A. C.; Maxson, J. B.; Ward, M. D., Electrocrystallization of an Ordered Organic Monolayer - Selective Epitaxial-Growth of Beta-(Et)2i3 on Graphite. *Chemistry of Materials* **1994,** 6, (12), 2222-2226.

69. Last, J. A.; Hillier, A. C.; Hooks, D. E.; Maxson, J. B.; Ward, M. D., Epitaxially driven assembly of crystalline molecular films on ordered substrates. *Chemistry of Materials* **1998,** 10, (1), 422-437.

70. Minemawari, H.; Naito, T.; Inabe, T., Control of Molecular Packing in the ET Based Conductor by Supramolecular Mellitate Networks (ET = Bis(ethylenedithio)tetrathiafulvalene). *Crystal Growth & Design* **2009,** 9, (11), 4830-4833.

71. Ferraro, J. R.; Williams, J. M., *Introduction to Synthetic Electrical Conductors.* Academic Press: San Diego: 1987.

72. Long, Y.-Z.; Li, M.-M.; Gu, C.; Wan, M.; Duvail, J.-L.; Liu, Z.; Fan, Z., Recent advances in synthesis, physical properties and applications of conducting polymer nanotubes and nanofibers. *Progress in Polymer Science* **2011,** 36, (10), 1415-1442.

73. Martin, C. R., NANOMATERIALS - A MEMBRANE-BASED SYNTHETIC APPROACH. *Science* **1994,** 266, (5193), 1961-1966.

74. Martin, C. R., TEMPLATE SYNTHESIS OF ELECTRONICALLY CONDUCTIVE POLYMER NANOSTRUCTURES. *Accounts Chem. Res.* **1995,** 28, (2), 61-68.

75. Granstrom, M.; Inganas, O., ELECTRICALLY CONDUCTIVE POLYMER FIBERS WITH MESOSCOPIC DIAMETERS .1. STUDIES OF STRUCTURE AND ELECTRICAL-PROPERTIES. *Polymer* **1995,** 36, (15), 2867-2872.

76. Park, J. G.; Kim, B.; Lee, S. H.; Park, Y. W., Current-voltage characteristics of polypyrrole nanotube in both vertical and lateral electrodes configuration. *Thin Solid Films* **2003,** 438, 118-122.

77. Xiong, S.; Wang, Q.; Chen, Y., Study on electrical conductivity of single polyaniline microtube. *Materials Letters* **2007,** 61, (14-15), 2965-2968.

78. Liu, L.; Zhao, Y. M.; Jia, N. Q.; Zhou, Q.; Zhao, C. J.; Yan, M. M.; Jiang, Z. Y., Electrochemical fabrication and electronic behavior of polypyrrole nano-fiber array devices. *Thin Solid Films* **2006,** 503, (1-2), 241-245.

79. Zach, M. P.; Ng, K. H.; Penner, R. M., Molybdenum nanowires by electrodeposition. *Science* **2000,** 290, (5499), 2120-2123.

80. Aleshin, A. N., Polymer nanofibers and nanotubes: Charge transport and device applications. *Advanced Materials* **2006,** 18, (1), 17-27.

81. Aleshin, A. N.; Lee, H. J.; Jhang, S. H.; Kim, H. S.; Akagi, K.; Park, Y. W., Coulomb-blockade transport in quasi-one-dimensional polymer nanofibers. *Physical Review B* **2005,** 72, (15).

82. Kim, B. H.; Park, D. H.; Joo, J.; Yu, S. G.; Lee, S. H., Synthesis, characteristics, and field emission of doped and de-doped polypyrrole, polyaniline, poly (3,4-ethylenedioxythiophene) nanotubes and nanowires. *Synthetic Metals* **2005,** 150, (3), 279-284.

83. Gence, L.; Faniel, S.; Gustin, C.; Melinte, S.; Bayot, V.; Callegari, V.; Reynes, O.; Demoustier-Champagne, S., Structural and electrical characterization of hybrid metal-polypyrrole nanowires. *Physical Review B* **2007,** 76, (11).

84. Callegari, V.; Gence, L.; Melinte, S.; Demoustier-Champagne, S., Electrochemically Template-Grown Multi-Segmented Gold-Conducting Polymer Nanowires with Tunable Electronic Behavior. *Chemistry of Materials* **2009,** 21, (18), 4241-4247.

85. Zhang, X. Y.; Lee, J. S.; Lee, G. S.; Cha, D. K.; Kim, M. J.; Yang, D. J.; Manohar, S. K., Chemical synthesis of PEDOT nanotubes. *Macromolecules* **2006,** 39, (2), 470-472.

86. Long, Y. Z.; Zhang, L. J.; Chen, Z. J.; Huang, K.; Yang, Y. S.; Xiao, H. M.; Wan, M. X.; Jin, A. Z.; Gu, C. Z., Electronic transport in single polyaniline and polypyrrole microtubes. *Physical Review B* **2005,** 71, (16).

87. Duvail, J. L.; Long, Y.; Cuenot, S.; Chen, Z.; Gu, C., Tuning electrical properties of conjugated polymer nanowires with the diameter. *Applied Physics Letters* **2007,** 90, (10).

88. Lu, G.; Li, C.; Shen, J.; Chen, Z.; Shi, G., Preparation of highly conductive gold-poly(3,4-ethylenedioxythiophene) nanocables and their conversion to poly(3,4-ethylenedioxythiophene) nanotubes. *Journal of Physical Chemistry C* **2007,** 111, (16), 5926-5931.

89. Das, A.; Lei, C. H.; Elliott, M.; Macdonald, J. E.; Turner, M. L., Non-lithographic fabrication of PEDOT nano-wires between fixed Au electrodes. *Organic Electronics* **2006,** 7, (4), 181-187.

90. Thapa, P. S.; Yu, D. J.; Wicksted, J. P.; Hadwiger, J. A.; Barisci, J. N.; Baughman, R. H.; Flanders, B. N., Directional growth of polypyrrole and polythiophene wires. *Applied Physics Letters* **2009,** 94, (3).

91. Peng, Z. A.; Peng, X., Formation of High-Quality CdTe, CdSe, and CdS Nanocrystals Using CdO as Precursor. *Journal of the American Chemical Society* **2000,** 123, (1), 183-184.

92. Aldana, J.; Wang, Y. A.; Peng, X. G., Photochemical instability of CdSe nanocrystals coated by hydrophilic thiols. *Journal of the American Chemical Society* **2001,** 123, (36), 8844-8850.

93. Chirea, M.; Pereira, C. M.; Silva, F., Catalytic Effect of Gold Nanoparticles Self-Assembled in Multilayered Polyelectrolyte Films. *The Journal of Physical Chemistry C* **2007,** 111, (26), 9255-9266.

94. Hiramatsu, H.; Osterloh, F. E., A simple large-scale synthesis of nearly monodisperse gold and silver nanoparticles with adjustable sizes and with exchangeable surfactants. *Chemistry of Materials* **2004,** 16, (13), 2509-2511.

95. Miller, J. S., Electrochemical Syntheses of Partially Oxidized Platinum Complexes. In *Inorganic Syntheses*, Balch, A. L.; Hartman, C., Eds. John Wiley & Sons, Inc.: 1979; Vol. 19, pp 13-18.

96. Carter, P. W.; Hillier, A. C.; Ward, M. D., Nanoscale Surface-Topography and Growth of Molecular-Crystals - the Role of Anisotropic Intermolecular Bonding. *Journal of the American Chemical Society* **1994,** 116, (3), 944-953.

97. Bergamini, J. F.; Ghilane, J.; Guilloux-Viry, M.; Hapiot, P., In situ EC-AFM imaging of cathodic modifications of platinum surfaces performed in dimethylformamide. *Electrochemistry Communications* **2004,** 6, (2), 188-192.

98. Dale, S. E. C.; Bending, S. J.; Peter, L. M., Real-Time In Situ Atomic Force Microscopy Imaging of Bismuth Crystal Growth. *Langmuir* **2009,** 25, (19), 11228-11231.

99. Macpherson, J. V.; Unwin, P. R.; Hillier, A. C.; Bard, A. J., In-situ imaging of ionic crystal dissolution using an integrated electrochemical/AFM probe. *Journal of the American Chemical Society* **1996,** 118, (27), 6445-6452.

100. Clarke, S. M., Neutron diffraction and incoherent neutron scattering from adsorbed layers. *Current Opinion in Colloid & Interface Science* **2001,** 6, (2), 118-125.

101. De Feyter, S.; De Schryver, F. C., Self-assembly at the liquid/solid interface: STM reveals. *Journal of Physical Chemistry B* **2005,** 109, (10), 4290-4302.

102. Orlin, D. V.; Shalini, G., Materials Fabricated by Micro- and Nanoparticle Assembly - The Challenging Path from Science to Engineering. *Advanced Materials* **2009,** 21, (19), 1897-1905.

103. Sachin, K.; Mercedes, C.-C.; David, N. R., Self-Assembling Nanoparticles at Surfaces and Interfaces. *ChemPhysChem* **2008,** 9, (1), 20-42.

104. Fendler, J. H., Chemical self-assembly for electronic applications. *Chemistry of Materials* **2001,** 13, (10), 3196-3210.

105. Kickelbick, G., Concepts for the incorporation of inorganic building blocks into organic polymers on a nanoscale. *Progress in Polymer Science* **2003,** 28, (1), 83-114.

106. Adams, D. M.; Brus, L.; Chidsey, C. E. D.; Creager, S.; Creutz, C.; Kagan, C. R.; Kamat, P. V.; Lieberman, M.; Lindsay, S.; Marcus, R. A.; Metzger, R. M.; Michel-Beyerle, M. E.; Miller, J. R.; Newton, M. D.; Rolison, D. R.; Sankey, O.; Schanze, K. S.; Yardley, J.; Zhu, X. Y., Charge transfer on the nanoscale: Current status. *Journal of Physical Chemistry B* **2003,** 107, (28), 6668-6697.

107. Saavedra, H. M.; Mullen, T. J.; Zhang, P. P.; Dewey, D. C.; Claridge, S. A.; Weiss, P. S., Hybrid strategies in nanolithography. *Rep. Prog. Phys.* 73, (3).

108. Andrew , R. H.; Beatriu, E.; Juan , F. M.; David , K. S., High-Tech Applications of Self-Assembling Supramolecular Nanostructured Gel-Phase Materials: From Regenerative Medicine to Electronic Devices. *Angewandte Chemie International Edition* **2008,** 47, (42), 8002-8018.

109. Eugenii, K.; Itamar, W., Integrated Nanoparticle-Biomolecule Hybrid Systems: Synthesis, Properties, and Applications. *Angewandte Chemie International Edition* **2004,** 43, (45), 6042-6108.

110. Ana, B. D.; Ramón, M.-M.; Félix, S.; Katrin, H.; Knut, R., The Supramolecular Chemistry of Organic-Inorganic Hybrid Materials. *Angewandte Chemie International Edition* **2006,** 45, (36), 5924-5948.

111. Nikoobakht, B.; Wang, Z. L.; El-Sayed, M. A., Self-Assembly of Gold Nanorods. *J. Phys. Chem. B* **2000,** 104, (36), 8635-8640.

112. Yang, P. D.; Kim, F., Langmuir-Blodgett assembly of one-dimensional nanostructures. *Chemphyschem* **2002,** 3, (6), 503-+.

113. Dieter Horn, J. R., Organic Nanoparticles in the Aqueous Phase - Theory, Experiment, and Use. *Angewandte Chemie International Edition* **2001,** 40, (23), 4330-4361.

114. Nguyen, T. Q.; Martel, R.; Avouris, P.; Bushey, M. L.; Brus, L.; Nuckolls, C., Molecular interactions in one-dimensional organic nanostructures. *Journal of the American Chemical Society* **2004,** 126, (16), 5234-5242.

115. Brousseau, L. C.; Zhao, Q.; Shultz, D. A.; Feldheim, D. L., pH-gated single-electron tunneling in chemically modified gold nanoclusters. *Journal of the American Chemical Society* **1998,** 120, (30), 7645-7646.

116. Chondroudis, K.; Mitzi, D. B., Electroluminescence from an organic-inorganic perovskite incorporating a quaterthiophene dye within lead halide perovskite layers. *Chemistry of Materials* **1999,** 11, (11), 3028-3030.

117. Mirkin, C. A.; Letsinger, R. L.; Mucic, R. C.; Storhoff, J. J., A DNA-based method for rationally assembling nanoparticles into macroscopic materials. *Nature* **1996,** 382, (6592), 607-609.

118. Yildiz, H. B.; Tel-Vered, R.; Willner, I., Solar Cells with Enhanced Photocurrent Efficiencies Using Oligoaniline-Crosslinked Au/CdS Nanoparticles Arrays on Electrodes. *Advanced Functional Materials* **2008,** 18, (21), 3497-3505.

119. Wang, R. M.; Li, L.; Arachchige, I.; Ganguly, S.; Brock, S. L.; Mao, G. Z., Nanoparticles Change the Ordering Pattern of n-Carboxylic Acids into Nanorods on HOPG. *Acs Nano* **2010,** 4, (11), 6687-6696.

120. Wang, S. X.; Li, L.; Mao, G. Z., Formation of Carboxylic Acid Nanorods on Oleylamide-Capped Au Nanoparticles. *Journal of Physical Chemistry C* **2012,** 116, (9), 5492-5498.

121. Rabe, J. P.; Buchholz, S., Commensurability and Mobility in 2-Dimensional Molecular-Patterns on Graphite. *Science* **1991,** 253, (5018), 424-427.

122. Kuroda, R.; Kishi, E.; Yamano, A.; Hatanaka, K.; Matsuda, H.; Eguchi, K.; Nagagiri, T., Scanning tunneling microscope images of fatty acid Langmuir-Blodgett bilayers. *J. Vac. Sci. Technol. B* **1991,** 9, (2), 1180-1183.

123. Kishi, E.; Matsuda, H.; Kuroda, R.; Takimoto, K.; Yamano, A.; Eguchi, K.; Hatanaka, K.; Nakagiri, T., Barrier-Height Imaging of Fatty-Acid Langmuir-Blodgett-Films. *Ultramicroscopy* **1992,** 42, 1067-1072.

124. Hibino, M.; Sumi, A.; Tsuchiya, H.; Hatta, I., Microscopic Origin of the Odd-Even Effect in Monolayer of Fatty Acids Formed on a Graphite Surface by Scanning Tunneling Microscopy. *J. Phys. Chem. B* **1998,** 102, (23), 4544-4547.

125. Mao, G.; Dong, W.; Kurth, D. G.; Mohwald, H., Synthesis of Copper Sulfide Nanorod Arrays on Molecular Templates. *Nano Lett.* **2004,** 4, (2), 249-252.

126. Chen, D.; Wang, R.; Arachchige, I.; Mao, G.; Brock, S. L., Particle-Rod Hybrids: Growth of Arachidic Acid Molecular Rods from Capped Cadmium Selenide Nanoparticles. *J. Am. Chem. Soc.* **2004,** 126, (50), 16290-16291.

127. Kaneko, F., Marcel Dekker: New York, 2001; p 53-97.

128. Wan, L.; Manickam, D. S.; Oupicky, D.; Mao, G. Z., DNA Release Dynamics from Reducible Polyplexes by Atomic Force Microscopy. *Langmuir* **2008,** 24, (21), 12474-12482.

129. Ulman, A., Formation and Structure of Self-Assembled Monolayers. *Chem. Rev.* **1996,** 96, (4), 1533-1554.

130. Huo, Q.; Liu, X.; Atwater, M.; Wang, J. H.; Dai, Q.; Zou, J. H.; Brennan, J. P., A study on gold nanoparticle synthesis using oleylamine as both reducing agent and protecting ligand. *Journal of Nanoscience and Nanotechnology* **2007,** 7, (9), 3126-3133.

131. Wang, R.; Li, L.; Arachchige, I.; Ganguly, S.; Brock, S. L.; Mao, G., Nanoparticles Change the Ordering Pattern of n-Carboxylic Acids into Nanorods on HOPG. *ACS Nano* **2010,** 4, (11), 6687-6696.

132. Wu, Y.; Cheng, G.; Katsov, K.; Sides, S. W.; Wang, J.; Tang, J.; Fredrickson, G. H.; Moskovits, M.; Stucky, G. D., Composite mesostructures by nano-confinement. *Nat Mater* **2004,** 3, (11), 816-822.

133. Tao, J.; Mao, G. Z.; Daehne, L., Asymmetrical molecular aggregation in spherulitic dye films. *Journal of the American Chemical Society* **1999,** 121, (14), 3475-3485.

134. Yang, T.; Berber, S.; Liu, J. F.; Miller, G. P.; Tomanek, D., Self-assembly of long chain alkanes and their derivatives on graphite. *Journal of Chemical Physics* **2008,** 128, (12), -.

135. Byung Gil, J.; Seok-Hong, M.; Chang-Woo, K.; Sang-Hyun, P.; Ki-Bum, K.; Tae-Sik, Y., Colloidal Nanoparticle-Layer Formation Through Dip-Coating: Effect

of Solvents and Substrate Withdrawing Speed. *Journal of The Electrochemical Society* **2009,** 156, (5), K86-K90.

136. Arachchige, I. U.; Brock, S. L., Sol-gel methods for the assembly of metal chalcogenide quantum dots. *Accounts of Chemical Research* **2007,** 40, (9), 801-809.

137. Chen, D.; Wang, R.; Arachchige, I.; Mao, G.; Brock, S. L., Particle-Rod Hybrids: Growth of Arachidic Acid Molecular Rods from Capped Cadmium Selenide Nanoparticles. *Journal of the American Chemical Society* **2004,** 126, (50), 16290-16291.

138. Moreno, E.; Cordobilla, R.; Calvet, T.; Cuevas-Diarte, M. A.; Gbabode, G.; Negrier, P.; Mondieig, D.; Oonk, H. A. J., Polymorphism of even saturated carboxylic acids from n-decanoic to n-eicosanoic acid. *New Journal of Chemistry* **2007,** 31, (6), 947-957.

139. Kaneko, F.; Kobayashi, M.; Kitagawa, Y.; Matsuura, Y., Collective Displacement of Acyl Chains on E-]C Phase-Transition of Stearic-Acid. *Journal of Physical Chemistry* **1992,** 96, (17), 7104-7107.

140. Bernstein, J.; Davis, R. E.; Shimoni, L.; Chang, N. L., Patterns in Hydrogen Bonding - Functionality and Graph Set Analysis in Crystals. *Angewandte Chemie-International Edition* **1995,** 34, (15), 1555-1573.

141. Malta, V.; Celotti, G.; Zannetti, R.; Martelli, A. F., Crystal structure of the C form of stearic acid. *J. Chem. Soc. B* **1971**, 548-553.

142. Meine, K.; Weidemann, G.; Vollhardt, D.; Brezesinski, G.; Kondrashkina, E. A., Atomic force microscopy and X-ray studies of three-dimensional islands on monolayers. *Langmuir* **1997,** 13, (24), 6577-6581.

143. Sato, K.; Okada, M., Growth of Large Single Crystals of Stearic Acid from Solution. *J. Crystal Growth* **1977,** 42, 259-263.

144. CCDC STARAC01contains the supplementary crystallographic data of stearic acid C-form. It can be obtained free of charge via www.ccdc.cam.ac.uk/data_request/cif, or by emailing: support@ccdc.cam.ac.uk. .

145. Meyerhofer, D., Characteristics of resist films produced by spinning. *Journal of Applied Physics* **1978,** 49, 3993-3997.

146. Bornside, D. E.; Macosko, C. W.; Scriven, L. E., Spin Coating - One-Dimensional Model. *Journal of Applied Physics* **1989,** 66, (11), 5185-5193.

147. Becker, R.; Döring, W., Kinetische Behandlung der Keimbildung in übersättigten Dämpfen. *Annalen der Physik* **1935,** 24, 719.

148. Volmer, M., *Kinetik der Phasenbildung*. Steinkopff: Leipzig, 1939.

149. Kashchiev, D., *Nucleation*. Butterworth-Heinemann: Oxford, 2000.

150. Fletcher, N. H., Size effect in heterogeneous nucleation. *J. Chem. Phys.* **1958,** 29, (3), 572-576.

151. Liu, X. Y., Generic Progressive Heterogeneous Processes in Nucleation. *Langmuir* **2000,** 16, (18), 7337-7345.

152. Cacciuto, A.; Frenkel, D., Simulation of colloidal crystallization on finite structured templates. *Physical Review E* **2005,** 72, (4).

153. Feldheim, D. L.; Keating, C. D., Self-assembly of single electron transistors and related devices. *Chemical Society Reviews* **1998,** 27, (1), 1-12.

154. Zabet-Khosousi, A.; Dhirani, A. A., Charge transport in nanoparticle assemblies. *Chemical Reviews* **2008,** 108, (10), 4072-4124.

155. Riskin, M.; Tel-Vered, R.; Bourenko, T.; Granot, E.; Willner, I., Imprinting of molecular recognition sites through electropolymerization of functionalized au nanoparticles: Development of an electrochemical TNT sensor based on pi-donor-acceptor interactions. *Journal of the American Chemical Society* **2008,** 130, (30), 9726-9733.

156. van Herrikhuyzen, J.; George, S. J.; Vos, M. R. J.; Sommerdijk, N. A. J. M.; Ajayaghosh, A.; Meskers, S. C. J.; Schenning, A. P. H. J., Self-assembled hybrid oligo(p-phenylenevinylene) - Gold nanoparticle tapes. *Angewandte Chemie-International Edition* **2007,** 46, (11), 1825-1828.

157. Nakai, H.; Yoshihara, M.; Fujihara, H., New Electroactive Tetrathiafulvalene-Derivatized Gold Nanoparticles and Their Remarkably Stable Nanoparticle Films on Electrodes. *Langmuir* **1999,** 15, (25), 8574-8576.

158. Deluzet, A.; Perruchas, S.; Bengel, H.; Batail, P.; Molas, S.; Fraxedas, J., Thin single crystals of organic insulators, metals, and superconductors by confined electrocrystallization. *Advanced Functional Materials* **2002,** 12, (2), 123-128.

159. Unwin, P. R., Concluding Remarks - Crystal growth and nucleation: tracking precursors to polymorphs. *Faraday Discussions* **2007,** 136, 409-416.

160. Crespilho, F. N.; Zucolotto, V.; Brett, C. M. A.; Oliveira, O. N.; Nart, F. C., Enhanced Charge Transport and Incorporation of Redox Mediators in Layer-by-Layer Films Containing PAMAM-Encapsulated Gold Nanoparticles. *The Journal of Physical Chemistry B* **2006,** 110, (35), 17478-17483.

161. Bradbury, C. R.; Zhao, J. J.; Fermin, D. J., Distance-independent charge-transfer resistance at gold electrodes modified by thiol monolayers and metal nanoparticles. *Journal of Physical Chemistry C* **2008,** 112, (27), 10153-10160.

162. Shein, J. B.; Lai, L. M. H.; Eggers, P. K.; Paddon-Row, M. N.; Gooding, J. J., Formation of Efficient Electron Transfer Pathways by Adsorbing Gold Nanoparticles to Self-Assembled Monolayer Modified Electrodes. *Langmuir* **2009,** 25, (18), 11121-11128.

163. Pruneanu, S.; Pogacean, F.; Biris, A. R.; Ardelean, S.; Canpean, V.; Blanita, G.; Dervishi, E.; Biris, A. S., Novel Graphene-Gold Nanoparticle Modified Electrodes for the High Sensitivity Electrochemical Spectroscopy Detection and Analysis of Carbamazepine. *Journal of Physical Chemistry C* **2011,** 115, (47), 23387-23394.

164. Zangwill, A., *Physics at Surfaces*. Cambridge University Press: Cambridge, UK, 1988.

165. Vereecken, P. M.; Strubbe, K.; Gomes, W. P., An improved procedure for the processing of chronoamperometric data: application to the electrodeposition of Cu upon (100) n-GaAs. *Journal of Electroanalytical Chemistry* **1997,** 433, (1-2), 19-31.

166. Martín, H.; Carro, P.; Hernández Creus, A.; González, S.; Salvarezza, R. C.; Arvia, A. J., Growth Mode Transition Involving a Potential-Dependent Isotropic to Anisotropic Surface Atom Diffusion Change. Gold Electrodeposition on HOPG followed by STM. *Langmuir* **1997,** 13, (1), 100-110.

167. Schmidt, U.; Donten, M.; Osteryoung, J. G., Gold Electrocrystallization on Carbon and Highly Oriented Pyrolytic Graphite from Concentrated Solutions of LiCl. *Journal of The Electrochemical Society* **1997,** 144, (6), 2013-2021.

168. Bradbury, C. R.; Kuster, L.; Fermín, D. J., Electrochemical reactivity of HOPG electrodes modified by ultrathin films and two-dimensional arrays of metal nanoparticles. *Journal of Electroanalytical Chemistry* **2010,** 646, (1-2), 114-123.

169. Coleman, L. B.; Cohen, M. J.; Sandman, D. J.; Yamagish.Fg; Garito, A. F.; Heeger, A. J., SUPERCONDUCTING FLUCTUATIONS AND PEIERLS INSTABILITY IN AN ORGANIC SOLID. *Solid State Communications* **1973,** 12, (11), 1125-1132.

170. Wudl, F., From Organic Metals to Superconductors - Managing Conduction Electrons in Organic-Solids. *Accounts of Chemical Research* **1984,** 17, (6), 227-232.

171. Williams, J. M.; Beno, M. A.; Wang, H. H.; Leung, P. C. W.; Emge, T. J.; Geiser, U.; Carlson, K. D., Organic Superconductors - Structural Aspects and Design of New Materials. *Accounts of Chemical Research* **1985,** 18, (9), 261-267.

172. Bryce, M. R., Functionalised tetrathiafulvalenes: new applications as versatile pi-electron systems in materials chemistry. *Journal of Materials Chemistry* **2000,** 10, (3), 589-598.

173. Scott, B. A.; La Place, S. J.; Torrance, T. B.; Silverman, B. D.; Welber, B.; J. Am. Chem. Soc. 1977, 6631., The Crystal Chemistry of Organic Metals. Composition, Structure, and Stability in the Tetrathiafulvalinium-Halide Systems. *J. Am. Chem. Soc.* **1977,** 99, 6631-6639.

174. Horváth, A. L., *Handbook of Aqueous Electrolyte Solutions: Physical Properties, Estimation, and Correlation Methods*. Ellis Horwood New York, **1985**; p 290.

175. Oesch, U.; Janata, J., Electrochemical study of gold electrodes with anodic oxide films-I. Formation and reduction behaviour of anodic oxides on gold. *Electrochim. Acta* **1983,** 28, (9), 1237-1246.

176. Oesch, U.; Janata, J., Electrochemical study of gold electrodes with anodic oxide films—II. Inhibition of electrochemical redox reactions by monolayers of surface oxides. *Electrochim. Acta* **1983,** 28, (9), 1247-1253.

177. El-Deab, M. S., On the preferential crystallographic orientation of Au nanoparticles: Effect of electrodeposition time. *Electrochim. Acta* **2009,** 54, (14), 3720-3725.

178. Welch, C. M.; Nekrassova, O.; Dai, X.; Hyde, M. E.; Compton, R. G., Fabrication, characterisation and voltammetric studies of gold amalgam nanoparticle modified electrodes. *Chemphyschem* **2004,** 5, (9), 1405-1410.

179. Trasatti, S.; Petrii, O. A., Real surface area measurements in electrochemistry. *Pure Appl. Chem.* **1991,** 63, (5), 711-734.

180. Finot, M. O.; Braybrook, G. D.; McDermott, M. T., Characterization of electrochemically deposited gold nanocrystals on glassy carbon electrodes. *Journal of Electroanalytical Chemistry* **1999,** 466, (2), 234-241.

181. El-Deab, M. S.; Okajima, T.; Ohsaka, T., Electrochemical reduction of oxygen on gold nanoparticle-electrodeposited glassy carbon electrodes. *Journal of The Electrochemical Society* **2003,** 150, (7), A851-A857.

182. Dai, X.; Nekrassova, O.; Hyde, M. E.; Compton, R. G., Anodic stripping voltammetry of arsenic(III) using gold nanoparticle-modified electrodes. *Analytical Chemistry* **2004,** 76, (19), 5924-5929.

183. Dai, X. A.; Compton, R. G., Direct electrodeposition of gold nanoparticles onto indium tin oxide film coated glass: Application to the detection of arsenic(III). *Analytical Sciences* **2006,** 22, (4), 567-570.

184. Praig, V. G.; Piret, G.; Manesse, M.; Castel, X.; Boukherroub, R.; Szunerits, S., Seed-mediated electrochemical growth of gold nanostructures on indium tin oxide thin films. *Electrochim. Acta* **2008,** 53, (27), 7838-7844.

185. Ino, S., Stability of Multiply-Twinned Particles. *Journal of the Physical Society of Japan* **1969,** 27, (4), 941-&.

186. Marks, L. D., Experimental studies of small particle structures. *Reports on progress in physics* **1994,** 57, (6), 603-649.

187. Keul, H. A.; Moller, M.; Bockstaller, M. R., Structural evolution of gold nanorods during controlled secondary growth. *Langmuir* **2007,** 23, (20), 10307-10315.

188. Kirkland, A. I.; Jefferson, D. A.; Duff, D. G.; Edwards, P. P.; Gameson, I.; Johnson, B. F. G.; Smith, D. J., Structural studies of trigonal lamellar particles of gold and silver. *Proc. R. Soc. London Ser. A-Math. Phys. Eng. Sci.* **1993,** 440, (1910), 589-609.

189. Yacaman, M. J.; Ascencio, J. A.; Liu, H. B.; Gardea-Torresdey, J., Structure shape and stability of nanometric sized particles. *J. Vac. Sci. Technol. B* **2001,** 19, (4), 1091-1103.

190. Wang, Z. L.; Mohamed, M. B.; Link, S.; El-Sayed, M. A., Crystallographic facets and shapes of gold nanorods of different aspect ratios. *Surf. Sci.* **1999,** 440, (1-2), L809-L814.

191. Liu, X. G.; Wu, N. Q.; Wunsch, B. H.; Barsotti, R. J.; Stellacci, F., Shape-controlled growth of micrometer-sized gold crystals by a slow reduction method. *Small* **2006,** 2, (8-9), 1046-1050.

192. Li, M. F.; Zhao, G. H.; Geng, R.; Hu, H. K., Facile electrocatalytic redox of hemoglobin by flower-like gold nanoparticles on boron-doped diamond surface. *Bioelectrochemistry* **2008,** 74, (1), 217-221.

193. Chen, Y.; Schuhmann, W.; Hassel, A. W., Electrocatalysis on gold nanostructures: Is the {110} facet more active than the {111} facet? *Electrochem. Commun.* **2009,** 11, (10), 2036-2039.

194. Kim, D. Y.; Im, S. H.; Park, O. O., Synthesis of Tetrahexahedral Gold Nanocrystals with High-Index Facets. *Cryst. Growth Des.* **2010,** 10, (8), 3321-3323.

195. Hsu, S. J.; Su, P. Y. S.; Jian, L. Y.; Chang, A. H. H.; Lin, I. J. B., Vertex and Edge Truncated Octahedron Gold Crystals. N-alkylimidazole and Silver(I) Ion Controlled Morphology Transformation. *Inorg. Chem.* **2010,** 49, (9), 4149-4155.

196. Yu, Y.; Zhang, Q. B.; Lu, X. M.; Lee, J. Y., Seed-Mediated Synthesis of Monodisperse Concave Trisoctahedral Gold Nanocrystals with Controllable Sizes. *Journal of Physical Chemistry C* **2010,** 114, (25), 11119-11126.

197. Keul, H. A.; Moller, M.; Bockstaller, M. R., Selective exposition of high and low density crystal facets of gold nanocrystals using the seeded-growth technique. *Crystengcomm* **2011,** 13, (3), 850-856.

198. Ivanova, O. S.; Zamborini, F. P., Size-Dependent Electrochemical Oxidation of Silver Nanoparticles. *Journal of the American Chemical Society* **2010,** 132, (1), 70-72.

199. Tang, L.; Han, B.; Persson, K.; Friesen, C.; He, T.; Sieradzki, K.; Ceder, G., Electrochemical Stability of Nanometer-Scale Pt Particles in Acidic Environments. *Journal of the American Chemical Society* **2010,** 132, (2), 596-600.

200. Jones, S. E. W.; Toghill, K. E.; Zheng, S. H.; Morin, S.; Compton, R. G., The Stripping Voltammetry of Hemispherical Deposits Under Electrochemically Irreversible Conditions: A Comparison of the Stripping Voltammetry of Bismuth on Boron-Doped Diamond and Au(111) Electrodes. *Journal of Physical Chemistry C* **2009,** 113, (7), 2846-2854.

201. Becker, R.; Döring, W., Kinetische Behandlung der Keimbildung in übersättigten Dämpfen. *Annalen der Physik* **1935,** 24, P 719.

202. Volmer, M., *Kinetik der Phasenbildung*. Dresden und Leipzig, T. Steinkopff: **1939**.

203. Staikov, G.; Milchev, A., The Impact of Electrocrystallization on Nanotechnology. In *Electrocrystallization in Nanotechnology*, Wiley-VCH Verlag GmbH & Co. KGaA: **2007**; pp 1-29.

204. Johnson, C. K.; Watson, J. C. R., Superstructure and modulation wave analysis for the unidimensional conductor hepta- (tetrathiafulvalene) pentaiodide. *The Journal of Chemical Physics* **1976,** 64, (6), 2271-2286.

205. Daly, J. J. a. S., F., Hepta(tetrathiafulvalene) pentaiodide: the projected structure. *Acta Crystallographica Section B* **1975,** 31, 620-621.

206. La Placa, S. J.; Corfield, P. W. R.; Thomas, R.; Scott, B. A., Non-integral charge transfer in an organic metal: the structure and stability range of (TTF)Br0.71–0.76. *Solid State Communications* **1975,** 17, (5), 635-638.

207. Warmack, R. J.; Callcott, T. A.; Watson, C. R., dc conductivity of tetrathiofulvalene bromide (TTF-Br_{n}) and TTF-I_{n} single crystals. *Physical Review B* **1975,** 12, (8), 3336-3338.

208. Reis, A. H.; Peterson, S. W.; Washecheck, D. M.; Miller, J. S., NATURE OF PT CHAIN DISTORTION IN PARTIALLY OXIDIZED ONE-DIMENSIONAL COMPLEX, K1.75PT(CN)4.1.5H2O. *Inorganic Chemistry* **1976,** 15, (10), 2455-2462.

209. Williams, J. M.; Keefer, K. D.; Washecheck, D. M.; Enright, N. P., STRUCTURAL STUDIES OF PRECURSOR AND PARTIALLY OXIDIZED CONDUCTING COMPLEXES .1. NEUTRON-DIFFRACTION AND

SPECTROSCOPIC INVESTIGATION OF QUASI-ONE-DIMENSIONAL POTASSIUM TETRACYANOPLATINATE (1.75-1) SESQUIHYDRATE, K1.75 PT(CN)4 .1.5H2O. *Inorganic Chemistry* **1976,** 15, (10), 2446-2455.

210. Epstein, A. J.; Miller, J. S., ANOMALOUS ELECTRICAL-CONDUCTIVITY OF THE POTASSIUM DEFICIENT LINEAR-CHAIN PLATINUM COMPOUND - K1.75PT(CN)4.1.5H20. *Solid State Communications* **1979,** 29, (4), 345-349.

211. Loveday, D. C.; Hillman, A. R.; Orpen, A. G.; Pringle, P. G.; Hepel, M., Electrochemical quartz crystal microbalance studies of partially oxidized tetracyanoplatinum salts. *J Mater Chem* **1996,** 6, (6), 993-998.

212. Keefer, K. D.; Washecheck, D. M.; Enright, N. P.; Williams, J. M., NOVEL QUASI-ONE-DIMENSIONAL ZIG-ZAG PLATINUM ATOM CHAIN IN K175PT(CN)4-1.5H2O - NEUTRON-DIFFRACTION STUDY. *Journal of the American Chemical Society* **1976,** 98, (1), 233-234.

213. Reis, A. H.; Peterson, S. W.; Washecheck, D. M.; Miller, J. S., PARTIALLY OXIDIZED ONE-DIMENSIONAL COMPLEX CONTAINING A DISTORTED PLATINUM CHAIN - MOLECULAR AND CRYSTAL-STRUCTURE OF K1.75 PT(CN)4-1.5H2O. *Journal of the American Chemical Society* **1976,** 98, (1), 234-236.

ABSTRACT

MOLECULAR CRYSTALLIZATION DIRECTED BY NANOPARTICLES AND NANOPATTERNS

by

LI LI

August 2013

Advisor: Dr. Guangzhao Mao

Major: Materials Science and Engineering

Degree: Doctor of Philosophy

This dissertation focuses on nanoparticle/nanopattern-induced molecular self-assembly and crystallization. We propose a universal strategy to synthesize organic/inorganic hybrid nanostructures using inorganic nanoparticles and nanoparticle arrays to induce organic crystalline compound nucleation and crystallization. The nanoconfinement effect will be addressed to study molecular crystallization by changing nanoparticle size, curvature and separation distance. Atomic force microscopy (AFM) is the main characterization tool to investigate the topography of the hybrid nanostructures and the nucleation and crystallization process. The proposed work will contribute to the understanding of seed mediated nucleation and crystallization, molecular ordering under nanoconfinement and hybrid nanomaterials.

AUTOBIOGRAPHICAL STATEMENT

LI LI

EDUCATION

- Ph.D., Materials Science and Engineering, Wayne State University, 2013
- M.S., Polymer Chemistry and Physics, Beihang University, China, 2008
- B.E., Polymer Materials and Engineering, Qingdao University, China, 2005

EXPERIENCE

- 05/2009 – 05/2013, Graduate Research Assistant, Wayne State University, MI
- 09/2008 – 05/2009, Graduate Teaching Assistant, Wayne State University
- 08/2005 – 05/2008, Graduate Research Assistant, Beihang University, China

PUBLICATIONS

1. **Li, L.**, Jahanian, P., Mao, G. "*Use Gold Nanoparticles to Confine Crystallization of Tetrathiafulvalene Bromide Charge Transfer Salt – a Seed-mediated Approach to Grow Organic Nanorods*." (To be submitted.)
2. **Li, L.**$^{+}$; Wang, S.$^{+}$; Mao, G. "*Formation of Carboxylic Acid Nanorods on Oleylamide-capped Au Nanoparticles."* J. Phys. Chem. C, 116, 5492-5498, **2012.** (Equal contribution)
3. Korala, L; **Li, L.**; Brock, S. L. *"Transparent Conducting Films of CdSe(ZnS) Core(shell) Quantum Dot Xerogels."* Chem. Commun., 48, 8523-8525, **2012**.
4. Wan, L.; **Li, L.**; Mao, G. "*Nanospiral Formation by Droplet Drying: One Molecule at a Time."* Nanoscale Res. Lett. 6(49), **2010.**
5. Wang, R.; **Li, L.**; Arachchige, I.; Ganguly, S.; Brock, S. L.; Mao, G. "*Nanoparticles Change the Ordering Pattern of n-Carboxylic Acids into Nanorods on HOPG."* ACS Nano, 4, 6687-6696, **2010.**